DEVELOPMENT OF NANOSTRUCTURED Ti AND Nb-BASED ALLOYS FOR BIOMEDICAL APPLICATIONS

BY
MOHAMED ABDRABOU HUSSEIN

A Dissertation Presented to the
FACULTY OF THE COLLEGE OF GRADUATE STUDIES
KING FAHD UNIVERSITY OF PETROLEUM & MINERALS
DHAHRAN, SAUDI ARABIA

In Partial Fulfillment of the
Requirements for the Degree of

DOCTOR OF PHILOSOPHY
In

MECHANICAL ENGINEERING

MAY 2015

KING FAHD UNIVERSITY OF PETROLEUM & MINERALS
DHAHRAN- 31261, SAUDI ARABIA
DEANSHIP OF GRADUATE STUDIES

This thesis, written by **MOHAMED ABDRABOU MOUSSAD HUSSEIN** under the direction his thesis advisor and approved by his thesis committee, has been presented and accepted by the Dean of Graduate Studies, in partial fulfillment of the requirements for the degree of **DOCTOR OF PHILOSOPHY IN MECHANICAL ENGINEERING**.

Dr. Nasser Al-Aqeel
(Advisor)

Dr. Zuhair Gasem
Department Chairman

Dr. Saheb Nouari
(Member)

Dr. Salam A. Zummo
Dean of Graduate Studies

Dr. C. Suryanarayana
(Member)

12/5/15
Date

Dr. Laoui, Tahar.
(Member)

Hassan
Dr. Hassan, Syed Fida
(Member)

DEDICATION

To my beloved parents, wife, my lovely daughter Mariem and son Omar

ACKNOWLEDGMENTS

First word and foremost thanks to Allah, the most gracious and the most merciful.

I would like to thank my advisor Dr. Nasser Al-Aqeeli for his advising, experienced, guidance and for his full support. I would like also to express special thanks and appreciations to the committee member, Dr. C Suryanarayana, University Of Central Florida, USA for his valuable help and guidance. I also express my deep thanks to other committee members, Dr. Saheb Nouari, Dr. Tahar Laoui, and Dr. Syed Fida Hassan.

Special thanks to King Fahd University of Petroleum and Minerals for sponsoring me, DSR for financial support of the projects, and for the Mechanical engineering department‘s Chairman and staff members. My deep thanks to Material Science lab family, Mr. Lateef Hashmi (Gold man) and Mr. Sadaqat for their help. I would like to thank also the Research Institute: Center of Excellence in Nanotechnology (CENT), Engineering Research Center, and Center of Excellence in Corrosion for their kind support. Kindest thanks to my colleagues in the Mechanical Engineering Department and to all my friends for their support and encouragement.

I would like to extend my thanks also to Kafrelsheikh University, Egypt for giving me this chance to join KFUPM for my Ph.D.

Also, I would like to express my love to my parents, my wife, my daughter Mariem, and my son Omar.as well as my brother and my sisters.

Finally, I wish to express my gratitude to every one gave a hand of help along the way in this work.

Table of Contents

LIST OF TABLES

LIST OF FIGURES

LIST OF ABBREVIATIONS

XRD	X-Ray Diffraction
MA	Mechanical Alloying
BPR	Ball-to-Powder Ratio
EDS	Energy Dispersive Spectroscopy
PCA	Process Control Agent
SEM	Scanning Electron Microscope
HV	Vickers Hardness
hr	Hour
PM	Powder Metallurgy
PSA	Particle Size Analyzer
SPS	Spark Plasma Sintering
TEM	Transmission Electron Microscope
SADP	Selected Area Diffraction Pattern
NZ	Nb-Zr Ninary System
TNZ	Ti-Nb-Zr Ternary System
DSC	Differential Scanning Calorimetry
β	Beta Phase
α	Alpha Phase
FE-SEM	Field Emission Scanning Electron Microscope
BCC	Body Centered Cubic
HCP	Hexagonal Close Packed
FCC	Face Centered Cubic
a	Lattice Parameter
SBF	Simulated Body Fluid
Ar	Argon
BF	Bright Field Image

IBM	Ion Beam Mixing
Sec	Second
P	Load
h	Displacement
GFE	Gibbs Free Energy

ABSTRACT (ENGLISH)

Full Name : [Mohamed Abdrabou Mousad Hussein]

Thesis Title : **[Development of Nanostructured Ti and Nb-based Alloys for Biomedical Applications]**

Major Field : **[Mechanical Engineering]**

Date of Degree : [May / 2015]

Titanium and Titanium-based alloys are generally preferred in the medical and dentistry fields compared to conventional alloys due to their enhanced mechanical properties and biocompatibility. Ti-based alloys were utilized with the addition of elements like Al, V, Cr, and Ni. However, it was reported that these elements have adverse effects on the utilization of these particular alloys, such as toxicity and genotoxicity which ultimately lead to lower biocompatibility. In addition, the osseointegration of such newly developed implant materials is one of the main goals of biomaterials research for dental and orthopedic applications to obtain enhanced interaction with cells.

This dissertation focuses on developing nanostructured Ti and Nb-based alloys with non-toxic elements and enhanced mechanical properties for biomedical applications by mechanical alloying and spark plasma sintering.

Different compositions were synthesized by ball milling and then characterized using XRD, TEM, and SEM. Afterwards, selected milled powders were sintered using spark plasma sintering. Microstructural evaluation and mechanical characterization were carried out for the sintered samples to investigate the effect of spark plasma sintering parameters on the microstructure and mechanical properties of the sintered alloys using XRD, FE-SEM, TEM, micro hardness, and nanoindentation measurements.

The results for the binary Nb-Zr system showed that a nanostructured Nb-Zr alloy with an average grain size of between 100-300 nm was successfully synthesized for the first time using the MA-SPS techniques. A maximum hardness and relative density of 584 HV and 97.9% were achieved respectively. The results also showed that the increased energy of the system due to MA led to the formation of solid-solutions at earlier time, then amorphous phase with further milling, which mechanically crystallized to an FCC phase on continued milling. In addition, an amorphous phase at Zr contents lower than 40% was achieved for the first time.

The results of ternary Ti-Nb-Zr system showed that nanostructured Ti20Nb13Zr at% near-β alloy with non-toxic elements and enhanced mechanical properties were successfully fabricated for the first time using the MA-SPS techniques. The results showed that at SPS temperature of 1200 °C, a nearly full density structure was obtained. The microstructure of the obtained alloy consist of a β-Ti (bcc) matrix which surround a α-Ti (hcp) region. The obtained alloy was chemically homogenized with a micro hardness value, HV of 657. The obtained nanostructured alloy having an average grain size of the dispersed α phase of 70 -140 nm. The nanostructured alloy increases the adhesion of osteoblast which will lead to enhanced interaction with cells compared to their coarse-grained counterparts. The developed nanostructured Ti–20Nb–13Zr at% alloy is a potential candidate for biomedical applications such as implant material for dental and orthopedic applications.

ABSTRACT (ARABIC)

الاسم الكامل:محمد عبدربه مسعد حسين

عنوان الرسالة: تطوير سبائك التيتانيوم والنيوبيوم ذات بنية نانومترية للتطبيقات الطبية الحيوية

التخصص: الهندسة الميكانيكية

تاريخ الدرجة العلمية: مايو 2015

يفضل التيتانيوم وسبائكه فى المجال الطبى وطب الاسنان مقارنة بالسبائك التقليدية وذلك بسبب خصائصه الميكانيكية الجيدة والتوافق الحيوى. تم استخدام سبائك التيتانيوم مع اضافة عناصر مثل الالمونيوم والفاناديوم والكروم والنيكل , ومع ذلك فان هذه العناصر لها تاثير سلبى يعيق الاستفادة من هذه السبائك مثل السمية والسمية الوراثية والتى تؤدى الى خفض التوافق الحيوى . بالاضافى الى ذلك فان الاندماج العظمى للمواد المطورة حديثا للانسجة هى واحدة من الاهداف الرئيسية فى ابحاث المواد الطبية لتطبيقات العظام والاسنان للحصول على تفاعل معزز مع الخلايا.

تركز هذه الرسالة على تطوير سبائك التيتانيوم والنيوبيوم ذات البنية النانومترية من عناصر غير سامة وتتميز بخصائص ميكانيكية محسنة للتطبيقات الطبية الحيوية باستخدام عملية التسابك الميكانيكى والتلبيد بشرارة البلازما .

تم تصنيع مركبات مختلفة باستخدام عملية التسابك الميكانيكى ثم تم عمل توصيف باستخدام حيود الاشعة السينية والمجهر الالكترونى الماسح والمنتقل . بعد ذلك تم عمل تلبيد للسبائك باستخدام شرارة البلازما . تم عمل فحص للبنية المجهرية والخواص الميكانيكية للعينات الملبدة لدراسة تاثير متغيرات عملية التلبيد بالشرارة الكهربائية على البنية المجهرية والخصائص الميكانيكية باستخدام حيود الاشعة السينة و المجهر الالكترونى الماسح والمنتقل ومقياس فيكر للصلادة وقياسات العلامة النانومترية.

اظهرت نتائج سبيكة النيوبيوم زركونيوم نجاح تصنيع سبيكة النيوبيوم زركونيوم ذات بينية نانومترية بمتوسط حجم حبيبات يتراوح من 100 الى 300 نانوميتر للمرة الاولى باستخدام عمليات التسابك الميكانيكى والتلبيد بشرارة البلازما الكهربائية.صلادة فيكرز للعينة 584 وكثافة نسبية تقدر بنحو 97.9 % . ا وضحت النتائج ايضا ان زيادة

الطاقة لنظام النيوبيوم زركونيوم باستخدام عملية التسابك الميكانيكى ينتج عنه تكوين محلول ذائب و طور غير متبلور والذى يتبلور ميكانيكيا الى طور متمركز الوجه مع الاستمرار فى عملية التسابك الميكانيكى. الطور الغير متبلور تم الحصول عليه بعد وقت اقل فى عملية التسابك الميكانيكى مقارنة بالطور متمركز الوجه. بالاضافة الى ذلك تم الحصول على طور غير متبلور لاول مرة عند تركيز منخفض للزركونيوم.

اظهرت النتائج لسبيكة التيتانيوم نيوبيوم زركونيوم تصنيع سبيكة ذات بنية نانومترية من عناصر غير سامة بنجاح بتكوين مجهرى بيتا مع الفا وخصائص ميكانيكية محسنة للمرة الاولى باستخدمات عمليات التسابك الميكانيكى والتلبيد بشرارة البلازما الكهربائية. اوضحت النتائج الحصول على بنية بكثافة 100% تقريبا باستخدام التلبيد بالشرارة الكهربائية عند درجة حرارة 1200 درجة مئوية . التركيب المجهرى للسبيكة يتكون من مصفوفة من بيتا تيتانيوم والتى تحيط بتيتانيوم الفا. كما ان التركيب المجهرى للسبيكة متجانس كيميائيا ذو صلادة فيكرز 657. السبيكة النانومترية ذات حجم حبيبات للطور الفا الموزع يتراوح بين 70 و140 نانوميتر والتى تعتبر واعدة لتعزيز وزيادة التصاق العظام (الخلايا التى تكون مصفوفة العظام) وتؤدى الى تعزيز التفاعل مع الخلايا. السبيكة التى تم تطويرها ذات البنية النانومترية مقترحة للتطبيقات الطبية الحيوية كنسيج فى تطبيقات العظام والاسنان.

CHAPTER 1

Introduction and Objectives

1.1 Motivation

The motivation of this thesis work is to develop nanostructured Ti and Nb-based alloys with non-toxic elements and enhanced mechanical properties for biomedical applications.

The motivation for developing new alloys in the nanostructured form is to enhance the performance of surgical implants as the nanostructured alloys shows enhanced mechanical properties and better biocompatibility in comparison with coarse-grained structure. The nanostructured materials are considered to be the future generation orthopedic biomaterials as they possess higher surface energy and larger surface area than their coarse grained counterparts which lead to enhance interaction with cells.

This effort of developing nanostructured materials by MA and SPS will introduce a new technological route for the development of these alloys for utilization in the medical and dentistry industries as biomedical implants.

1.2 Introduction

Metallic materials have a variety of applications in the medical field. Specifically, they are used for internal support and biological tissue replacements such as joint replacement, dental roots, orthopedic fixation and stents [1]. The major metals and alloys that are being utilized for biomedical applications are: stainless steels, Co-based alloys, and Ti alloys [2].

However, Ti and Ti-based alloys have dominated over other alloys' systems in the medical and dentistry fields due to their improved biocompatibility. [3]

Many Ti-base alloys were developed with the addition of multiple constituents in order to evaluate their individual contribution and arrive at an optimum composition that possesses high biocompatibility. Different metals like vanadium, nickel, chromium, and aluminum were added via different processing routes and some advanced Ti alloys were introduced, like Ti-6Al-4V. However, it was observed that vanadium and aluminum have a probable toxicity, and can cause mutagenic cytology in addition to triggering allergic reactions [4, 5]. Other constituents like nickel were found to cause a lower bio compatibility [6], and Cr has a major concern due to its genotoxicity [3]. Therefore, the selection of the right alloy composition in addition to finding the best processing method has been a concern in the biomedical/biomaterials field.

The elements considered in this thesis Ti, Zr, and Nb meet the criteria for biomaterials in terms of biocompatibility, resistance to corrosion, mechanical considerations and ionic cytotoxicity[3] . When there is a wide range of melting temperatures between the alloy constituents the utilization of conventional casting techniques in the synthesis of Ti-based alloys does not seem to be an optimal option due to plausible absence of homogeneity. Therefore, mechanical alloying (MA) a completely solid state technique, can be considered as a promising technique to combat limitations faced by casting techniques [7]. It has the advantage to produce homogenous alloys compared to other techniques, especially when the alloying elements have a higher melting temperature such as Nb[3]. In addition powder metallurgy (PM) is considered to be an effective way in reducing the higher machining cost of Ti alloys.

Nevertheless, the production of net-shape parts of MA samples needs to go through the challenge of consolidation as the product of MA is always in the powder form. The situation becomes even more challenging when the produced alloys from MA are having nanostructures since the heat associated with conventional consolidation techniques can induce undesirable grain growth. In recent years, many non-conventional sintering methods, such as spark plasma sintering, emerged and proved to be beneficial in minimizing undesirable phase transformations and grain growth [8].

It was reported that nanophase materials are considered to be the future generation orthopaedic biomaterials [9], possess unique surfaces and exceptional mechanical properties, and better biocompatibility compared to coarse grain structure [10]. Nanocrystalline alloy possess higher surface energy and larger surface area than coarse grained which ones to enable enhanced interaction with cells which lead to better proliferation and cell attachment on the nanocrystalline alloy [9].

1.3 Objectives

The main objective of this work is to develop nanostructured Ti and Nb-based alloys with non-toxic elements for biomedical applications by powder metallurgy: MA and SPS for both binary Nb-Zr and ternary TiNbZr (TNZ) systems.

The specific objectives to achieve in the overall aim of the current work, were as follows:

1 Solid-state synthesize of Nb-Zr and TNZ alloys by mechanical alloying (MA).

2 Study the phase evolution, and microstructural investigation for the MA alloys using XRD, TEM, and SEM.

3 Develop and synthesize nanostructured Nb-Zr and TNZ alloys using spark plasma sintering for biomedical applications.

4 Investigate the effect of SPS parameters on the microstructure and mechanical properties of the sintered alloys using XRD, FE-SEM, TEM, micro hardness, and nanoindentation measurements.

1.4 Thesis Overview

In this dissertation, chapter 2 briefly presents an introduction about nanomaterials, MA, and SPS, as well as literature review about the research on Nb-Zr, and TNZ alloys. Chapter 3 describes in details the raw materials and experimental techniques used to conduct the research work. Chapter 4 presents all the results and discussions for both Nb-Zr, and TNZ alloy system and comparison of the results with the related observation from literature. Finally, chapter 5, summarize the final conclusions from the research work, the contributions of the dissertation to the original knowledge, and the future directions to pursue. The publications are listed in appendix A

CHAPTER 2

Literature Review

2.1 Biomaterials

A biomaterial is a material used in a medical device or an implant intended to interact with different biological systems. Biomaterials should have some characteristics such as being hard, flexible, inert for reactions with any tissue of the human body, non-toxic, and non-biodegradable. In addition to biocompatibility of biomaterials, the mechanical properties that are of interest in the different biomaterials' applications are: stiffness, strength, toughness, hardness, fatigue, fracture strength, and wear resistance.

2.1.1 Requirements of Biomaterials (Implant)

All biomaterials are required to satisfy various criteria, such as adequate strength, high resistance to corrosion, bio adhesion, and biocompatibility, high wear resistance and low friction [11]. The main requirements of biomaterial are given below.

Mechanical properties: the material should have a low modulus of elasticity combined with high strength to prolong the service period of the implant and prevent loosening, thereby preventing the need for revision surgery. Additionally, stress shielding can be prevented by matching the modulus of elasticity of biomaterials to that of the bone [12, 13].

Biocompatibility: *"Biocompatibility refers to the ability of a material to perform with an appropriate host response in a specific situation" [14]*. The developed material should be compatible with living systems and not cause any bodily harm, which includes all of the negative effects a material can have on the components of a biological system (bone, extracellular - and intracellular tissues and ionic composition of plasma) [15,16].

High wear resistance: the material should have a high wear resistance and exhibit a low friction coefficient when sliding against body tissues. The higher the friction coefficient value or the lower the wear resistance can cause the implant to loosen [15, 16]. Moreover, the wear debris generated can cause inflammation that is destructive to the bone supporting the implant.

High corrosion resistance: an implant that is made of a biomaterial with a lower corrosion resistance can release metal ions into the body, which in turn produce toxic reactions [17].

Osseointegration: Osseointegration was first defined as “a direct structural and functional connection between ordered, living bone and the surface of a load-carrying implant” (Branemark, 1983). The roughness, chemistry, and topography of the surface play a major role in good osseointegration [18]. Implant loosening results from the non-integration of the implant surface into the adjacent bone [19].

Nontoxic The material should be neither geno toxic (which can alter the DNA of the genome) nor cytotoxic (causes damage to individual cells).

Long fatigue life the material should exhibit a high resistance to failure by fatigue to prevent implant failure and stress shielding from fatigue fracture. The failure of implants by fatigue has been reported for hip prostheses [20].

2.2 Metallic Alloys for Biomaterials

The materials that are used to build biomedical devices (orthopedic, dental, bone cements, etc.) can be classified into metallic materials, ceramics, polymers, and composites. Metallic materials within these four categories are widely used because of it possesses high strength, toughness, and good biocompatibility. For decades, metals have been used extensively in a variety of applications in the medical field. Specifically, metals are used for internal support and biological tissue replacements, such as joint replacements, dental roots, orthopedic fixation and stents [1]. The high reliability of metallic biomaterials, in terms of their mechanical performance, has resulted in their use, "mainly for the fabrication of medical devices for the replacement of hard tissue such as artificial hip joints, bone plates, and dental implants" [2]. The metals and alloys that are primarily used in biomedical applications are stainless steels, Co alloys, and Ti alloys [2, 21]. A brief description of each material is given below.

2.2.1 Stainless Steels

The austenitic stainless steel SUS 316L is reported to be used in the biomedical field. However, the Ni present in this alloy causes allergic reactions [2]. Moreover, pitting, crevice, and stress corrosion has been reported for implants fabricated from SUS 316L [6]. To prevent Ni allergic reactions, an austenitic stainless steel with high nitrogen content has been developed. Therefore, the new research trend is to develop Ni-free stainless steels.

2.2.2 Co Alloys

The resistance of Co alloys to the wear was reported to be higher than that of both Ti alloys and stainless steel alloys [6]. In artificial hip joints, the head of the joint is subjected to wear. Thus, hip joints have been fabricated from Co alloys, such as Co-Cr-Mo alloys, which exhibit high strength and ductility. According to [2], dispersing carbides in Co alloys leads to increase in the resistance to wear of these alloys [2]. However, the Ni content in wrought Co-Cr alloys causes allergic reactions [6].

2.2.3 Ti Based Alloys

The high biocompatibility of Ti and Ti alloys has resulted in their preferential use over other alloy systems in the medical and dentistry fields [4, 5, 22]. The primary characteristics of Ti alloys that have resulted in their being one of the main choices in the biomedical field include good mechanical properties, excellent corrosion resistance because of a TiO_2 solid oxide layer, good biocompatibility, a relatively low Young’s modulus, light weight, and non-magnetic behavior. The aforementioned characteristics make Ti and Ti alloys the preferred choice for implantation. Some of the important applications for Ti-based alloys are shown in Figure 1 .

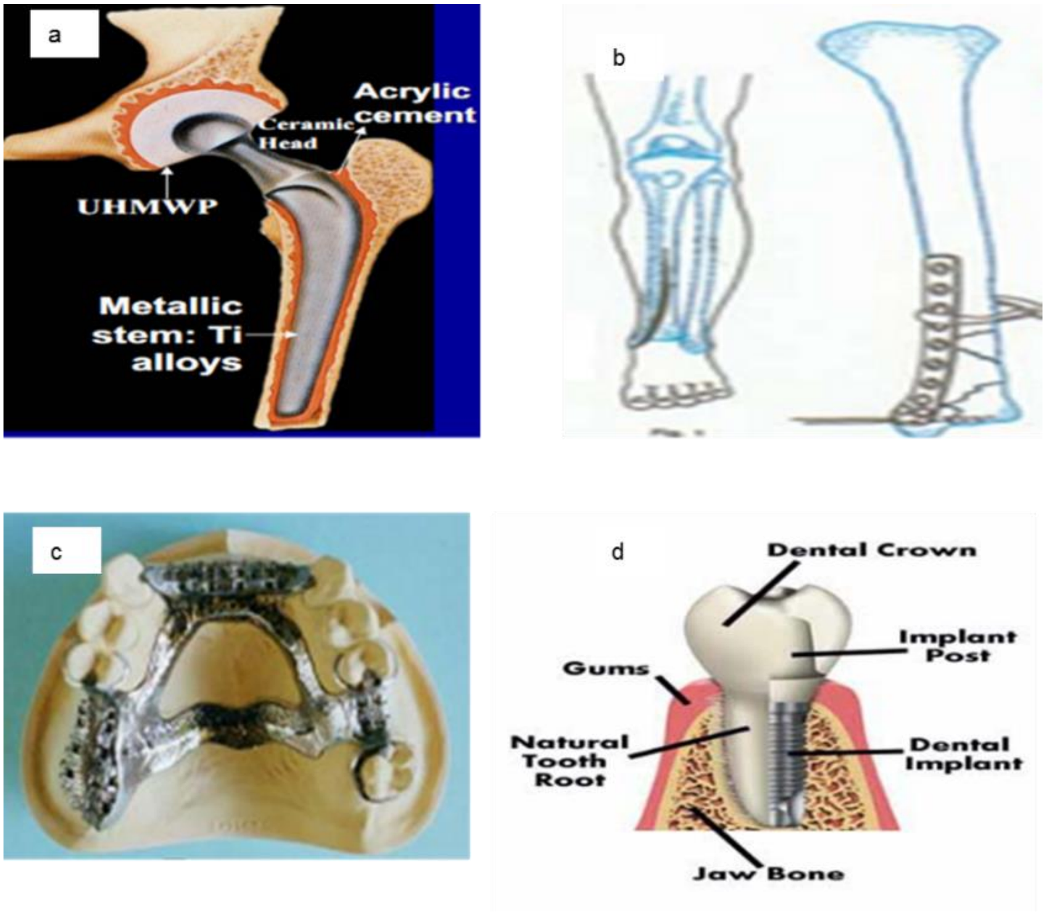

Figure 1 Selected applications for Ti-based alloys:

a) Artificial hip joint[23], b) Bone plate [23], c) Denture [23] , and d) Dental Implants [24]

2.3 Research on Ti Based Alloys

The development of Ti alloy with the addition of different constituents like vanadium, nickel, chromium, and aluminum was reported in the literature [3]. However, for the utilization of these alloys in the biomedical field, characterization usually goes beyond mechanical evaluation to include biocompatibility, toxic effect, and corrosion resistance. Table 1 Summarizes characteristics for selected elements that are used in different alloys' systems. While the V and Al (available in the widely used Ti-6Al-4V alloys) are not susceptible to corrosion they have a probable toxicity [4] and can cause mutagenic cytology and allergic reaction [5]. Moreover, from Table 1, it is clear that Ni shows a lower biocompaitability while Cr have concern to its genotoxicity [3]. Therefore, the selection of the right chemical composition of the developed alloy for biomedical applications is a major concern and subsequently has been an active area of research. This is in addition to choosing the right processing route in order to optimize different properties of the developed alloys.

According to Table 1, it appears that Ti, Zr, and Nb meet the criteria for biomaterials in terms of biocompatibility, resistance to corrosion, mechanical considerations, and ionic cytotoxicity [3]. The addition of niobium (Nb) to Ti allows these alloys to act as β-stabilizers and possess improved mechanical properties and also improved wear resistance, while the addition of Zr helps in obtaining the solid-solution required for hardness [4]. Therefore, additions of Zr and Nb seem to be a promising direction for the development of Ti-based alloys for biomedical applications.

Table 1 Characteristics of different elements [3]

Element	Biocompatability	Genotoxic	Cytotoxic	Prone to corrosion
Ti	Yes	No	Moderate	No
V	No	Yes	High	No
Cr	No	Yes	High	No
Ni	No	Yes	High	Yes
Nb	Yes	No	Low	No
Zr	Yes	No	Low	No
Al	No	Yes	Low	No
Co	No	Yes	High	Yes
Fe	No	Yes	Moderate	Yes

The computed liquidus and solidus projections of TNZ ternary system [25] are shown in Figure 2. It is clear from the phase diagram that the liquidus and solidus temperatures increase with increasing Nb content. The liquidus and solidus isotherms are between 2750 K and 2128 K.

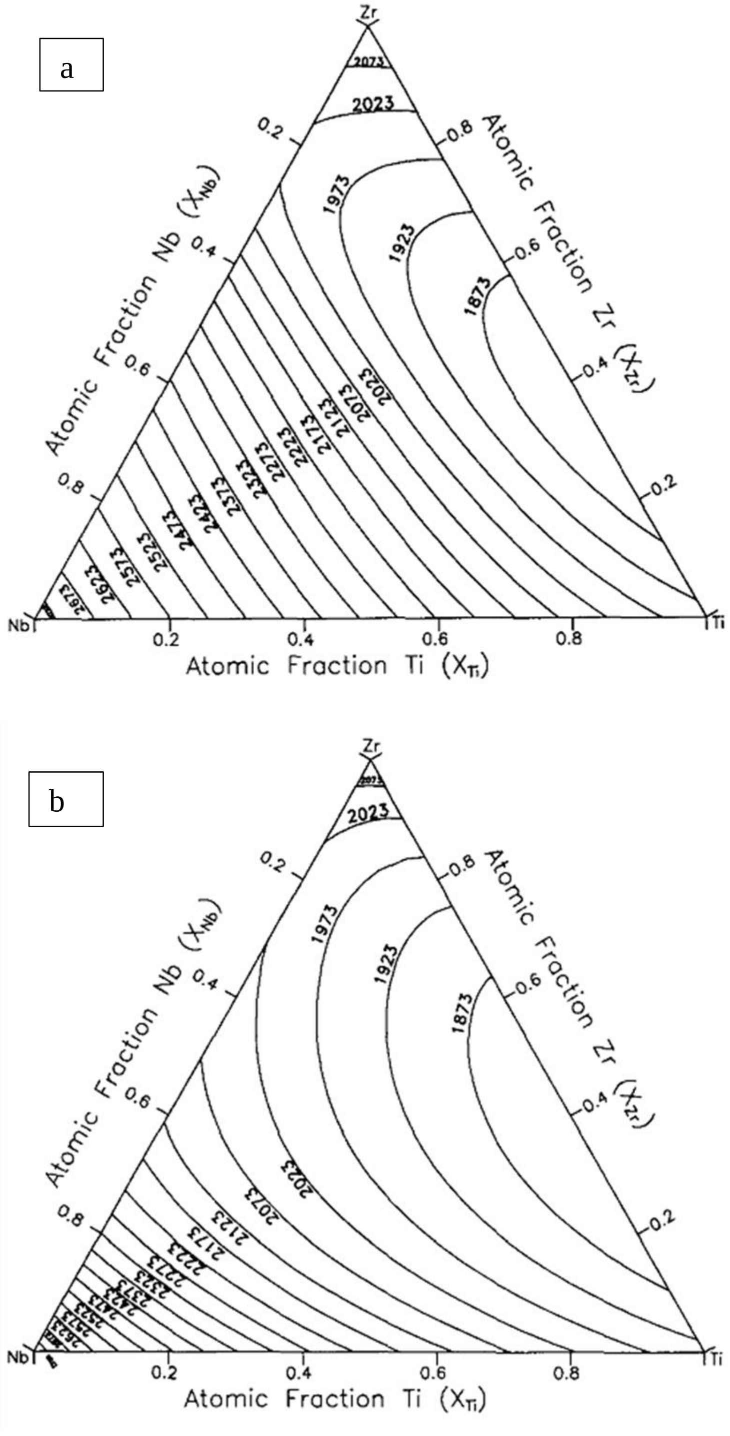

Figure 2 TNZ: a) computed liquidus projection, b) computed solidus projection [25]

(Temperatures are in kelvins)

There has been some reported work in the literature towards the development of Ti-based alloys using arc melting and casting techniques [4, 26-34]. Nevertheless, when there is a broad range of melting temperatures between alloy constituents the utilization of conventional casting techniques in the synthesis of Ti-based alloys does not seem to be a good option due to plausible absence of homogeneity. Therefore, mechanical alloying (MA) can be considered as a promising technique to combat limitations faced by casting techniques. MA has been used successfully in the development of nanostructured materials and the synthesis of immiscible systems [7]. It was also utilized heavily in the augmentation of second phases in commonly used alloys' systems and introduced an improvement in mechanical and physical properties. This technique was reported to be simple, versatile, and economically viable and can be scaled up to produce large quantities [7]. Moreover, MA proved to be a viable choice for the production of nanomaterials and nanocomposites from systems that are difficult to alloy using conventional processing routes [7]. The PM is considered to be an effective way in reducing the higher machining cost of Ti alloys.

In the present work, MA has advantages to produce a homogenous alloys compared to other techniques, especially when the alloying element has a higher melting temperature such as Nb [18]. Also, the use of MA will enhance the chances of synthesizing nanostructured Ti-based alloys with improved mechanical properties. Nevertheless, the production of net-shape parts of MA samples needs to go through the challenge of consolidation as the product of MA is always in the powder form. The situation becomes even more challenging when the produced alloys from MA are having nanostructures since the heat associated with conventional consolidation techniques can induce undesirable grain growth.

Nowadays, there are multiple consolidation techniques that can be used in the coalescence of processed powders and they vary fundamentally in the way they supply energy. The introduction of non-conventional techniques has prompted the retention of nano and other metastable phases in the final products. This has subsequently opened new venues for the utilization of MA in the production of advanced materials that are ready to be used in very challenging circumstances. SPS is considered as non-conventional and new sintering technique and classified as rapid consolidation technique [34, 35]. With careful optimization of the sintering parameters, these techniques can be used to develop new materials with finer grain sizes compared to other conventional techniques [34]. Some published work considered the utilization of SPS for consolidation of Ti-based alloys of biomedical applications like: Ti–35Nb–7Zr–5Ta [34], Ti-Mn [36], Ti-Al-V [37], Ti-Ni-Mo [38], $Ti_{40}Zr_{10}Cu_{36}Pd_{14}$ [39], TiNi [40], and Ti-Nb-Zr-CPP composites [41]. They have all concluded that the samples consolidated by SPS have higher microhardness values compared to alloys prepared by conventional consolidation techniques.

SPS has already been used by several researchers in synthesizing Ti alloys. XU Li-Juan et al [42] used MA and SPS to produce a fine grained Ti43Al9V alloy. Cristina et al [43] successfully obtained Ti alloy by SPS from hydride (TiH2) powders. Nicula et al [44] used SPS to produce a fully dense cp Ti, (Ti–Al–V) and porous structure for (Ti–Al–V–Cr, Ti–Mn–V–Cr–Al) alloys. Recently, Ming Wen, et al [45] developed Ti–Nb–Ag alloy using both conventional vacuum sintering and SPS, and found that fracture strength obtained by SPS is three times than obtained by conventional sintering. The Nb content was reported to improve corrosion resistance in binary Nb-Zr alloy [46], and to increase the wear resistance of the Ti-Nb-Ta-Zr alloy [47].

However, to my knowledge, no work was reported in the literature for the consolidation of powder processed Ti-Nb-Zr system using SPS technique. It has to be mentioned, though, that the development and characterization of nanostructured Ti-based alloys for biomedical applications are in exploratory level. More research is required to enhance their mechanical properties, their applicability and subsequently open new areas for their utilization. One of the possible strategic directions in the future of the biomaterials industry is in the development of nanostructured Ti-based alloys [18]. Moreover, it has been reported that nanophase materials do possess unique surfaces and exceptional mechanical properties similar to those of the human bones; hence they are considered to be the future generation orthopaedic biomaterials [18].

Using SPS consolidation to get a nanostructured alloy will be promising and lead to enhanced mechanical properties, biocompatibility and interaction with cells.

2.4 Research on Nb-Zr Alloys

The alloying behavior between different metals is related to the thermodynamic parameters. The heat of mixing (ΔH^{mix}) between elements predominantly determines the alloying behavior; the more negative ΔH^{mix}, the easier it is for the elements to alloy together [48]. It is possible to produce majority of the alloys of engineering importance only because of the negative heat of mixing between them. However, there are also several pairs of elements which display a positive heat of mixing and therefore it is not possible to produce alloys from them and derive benefits for industrial exploitation. It has been possible in some cases to achieve mixing, though to a limited extent, by processing these materials under non-equilibrium conditions.

Materials processing under conditions of non-equilibrium processing has become important in recent years to achieve properties in materials that have not been possible under equilibrium conditions [49]. In fact, it is well-established that materials processed under non-equilibrium conditions usually display much better and vastly improved mechanical, physical, and chemical behavior. For example, they are very hard and strong, exhibit superior magnetic properties, and in many cases, these materials also show improved corrosion resistance, with the caveat that such alloys usually contain elements such as Cr, Mo, and P [50]. Further, it has been possible to achieve increased levels of supersaturation of solute elements, formation of non-equilibrium crystalline intermetallic phases, and in extreme cases, even amorphous phases [51, 52].

Nb and Zr are desirable elements for use in biological systems and biomedical applications thanks to their biocompatibility, resistance to corrosion, mechanical integrity and ionic cytotoxicity [53, 54]. Nb–Zr alloys showed also applications in space nuclear power systems[55] . However, Nb–Zr alloys show a positive heat of mixing that has a magnitude that ranges from 16 to 17 $kJmol^{-1}$ [55–56]. As indicated in the phase diagram shown in Figure 3 [57], the Nb-Zr system is phase separating at room temperature and atmospheric pressure.

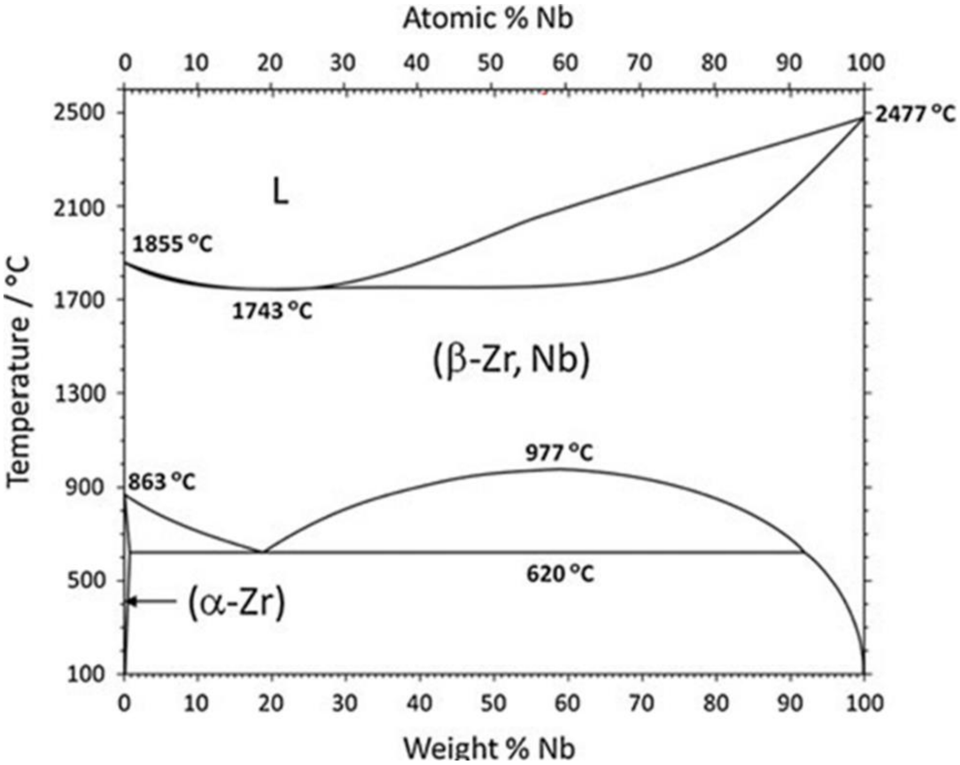

Figure 3 Phase diagram of Niobium–Zirconium system [57]

Thus, conventional processing might not be suitable for these alloys and the use of non-equilibrium processing techniques for the development of the underlying microstructures gained considerable attention in recent years [58]. MA is one of the non-equilibrium processing that is capable of synthesizing alloys with improved properties, despite its simplicity. In this technique, phase diagram restrictions do not apply, and non-equilibrium phases are achieved. To date, only little attention was given to the use of MA to produce alloys made up of immiscible Zr and Nb.

MA and rapid solidification processing as nonequilibrium processing techniques aided in synthesizing a supersaturated solid solution from immiscible system alloys [59]. Compared to rapid solidification, MA has an edge in that it is possible to produce metastable phases more easily.

Amorphous alloys have an interesting combination of physical, chemical, mechanical and magnetic properties [58, 60]. These phases have been produced in several alloy systems by non-equilibrium processing methods for example: rapid solidification processing of liquid alloys involving solidification rates of as high as 10^6 K/s, [61] vapor deposition, where the quenching rates can be even higher, typically 10^{12} K/s, [62] mechanical alloying, [63,64]ion beam mixing[65] and others. [48]. Majority of these metastable alloys have been produced by liquid quenching or vapor quenching methods in alloy systems that show a negative heat of mixing, since, only under this condition, the constituent elements mix thoroughly in the liquid or vapor phases. But, when the heat of mixing is positive, constituent elements cluster together and no alloying occurs. Consequently, there have not been any reports of amorphous phase formation in immiscible alloy systems. However, alloys produced by severe plastic deformation methods such as MA and ion beam mixing (IBM) (which involves large displacements of atomic positions due to irradiation) do not follow phase diagram restrictions and consequently the type of metastable phases produced are significantly different from those produced by liquid quenching or vapor quenching methods, and include the amorphous phases in some of these alloy systems.

MA has been reported to result in the formation of either solid solutions in Ge-Al [66], , and Fe-Cu [67] systems or supersaturated solid solutions between elemental pairs exhibiting positive heat of mixing in Cu-V [68] , Fe-Mg [69], Pb-Al [70,71], Ni-Ag [72], and Fe-Pb [69] systems. Additionally, fully amorphous phases were obtained using MA in elemental pairs such as W-Cu [73], Cu-V [74], and Cu-Ta [75, 76], which are considered as immiscible systems. In other studies, partial amorphization was achieved in some systems such as Cu-Ta [77]. Amorphization was obtained in several Nb-Zr containing alloys, such as Ni-Nb-Zr, Cu-Nb-Zr, Ti-Nb-Zr, Fe-Ti-Nb-Zr, and Nb-Zr-Al-Ni-Cu, upon subjecting their powder mixes to MA [78-82]. However, only a few reports claim to have achieved alloying between Nb and Zr elemental powders. Miyazaki et al. [57] investigated the structure developed in the Nb-Zr system using High Pressure Torsion (HPT) and reported that, after 100 rotations of HPT, a supersaturated solid solution was formed while after 2 rotations, a β-Zr phase had appeared. Aurelio et al. [83] studied the effect of an isothermal treatment on the structural properties and stability of metastable phases formed by quenching Nb-Zr alloys. They performed an analysis of both phase reactions and composition changes upon aging and found that the Nb content of the β phase in the aged condition was higher than that of β phase in the quenched (or untransformed BCC) condition. Also in the alloy subjected to the longest aging treatments, the β phase coexisted with α.

Due to its nature, MA is perhaps the most suitable processing technique to produce metastable phases in the Nb-Zr system, since this technique was reported to produce glassy and metastable crystalline phases in several alloy systems [84-86]. Loureiro et al. [87] investigated the microstructures developed in the binary Niobium–Zirconium binary system and the hydrogenation behavior after MA of Zr-5%Nb alloy. It was reported that addition of Nb induced partial allotropic transformation of the Zr structure from α-Zr to ω-Zr. Nevertheless, the aforementioned work was only focused on one composition with low Nb content and did not explore the changes due to variable Nb concentrations.

Wang et al. [56] investigated the alloying behavior in the Nb-Zr system using ion beam mixing (IBM) and suggested that an amorphous phase is possible to be produced in the range of 8-88 at. % Zr in the binary Nb-Zr system. Moreover, by including sufficient interfacial free energy, the GFE of the Zr–Nb multilayered films could be elevated to a higher level and two metastable crystalline phases of FCC structure with different lattice parameters were obtained [55,56].

Nb–Zr alloys show the presence of metastable phases such as omega [83]. Jin et al [55] showed that an amorphous phase could be produced in ion-irradiated multilayer thin films corresponding to the composition of Nb–40 at.% Zr. Most recently, Suryanarayana and Liu [88] showed that there were indications of the formation of an amorphous phase in MA Nb–10 and 20 at. % Zr powder mixtures. An observation which was not confirmed in their work.

Multiple studies have considered the use of SPS to produce Nb-based alloys in different systems, for example Nb-Al, Nb-Al-W, Nb-Al-Mo and Nb-Al-N [89]. Although fully dense alloys were achieved in the Nb-Al system, inhomogeneous microstructures have been obtained in the Nb-Al-W and Nb-Al-Mo systems due to insufficient sintering time, which highlights the need for careful tuning of the SPS process [89]. Moreover, SPS has been used to produce Nb-Si-Cr and Nb-Si-B alloys and the resultant microstructure, oxidation behavior, mechanical and physical properties have been studied [90-91]. SPS has been also used to produce Nb-Si alloys with a densification exceeding 99.5% [92]. In other work [93], Nb/Nb5Si3 composites were successfully prepared using the SPS, with the resulting alloys almost fully dense and with high compressive ductility in addition to high strength. High-density (approximately 97.7%) NbB2 was obtained in yet another study [94] by SPS from elemental powders of Nb and B sintered at 1900°C for a holding time of

15 minutes. In a recent study [95], zirconium micron-alloyed tungsten with a relative density of 97% was prepared using SPS.

Both niobium and zirconium are highly passivating metals [96, 97] and it was proven that the amount of released metallic ions from Nb-Zr alloy into physiological media is small (<0.3 mgL-1) [98]. In particular, the addition of Zr was found to result in a high biocompatibility and high resistance to corrosion because of the formation of a stable oxide surface layer. However, little work was done to unravel the possible utilization of Nb-Zr alloys as biomedical implants and to adequately assess their properties. Some of the few literature include the work of Zhou et al [52] in which they developed Zr–xNb alloys, where x= (2.5, 16 and 22) wt. % using vacuum arc-melting method. They studied the effect of Niobium addition on the corrosion properties of the developed alloys. Their results showed that the corrosion resistance of the alloy increased by increasing the Nb content. In another study, Rubitschek et al [99] examined the corrosion resistance of ultrafine-grained (UFG) Nb-2Zr wt.% alloy processed using multipass equal channel angular processing (ECAP) in (SBF) . They showed that the ultra-fine grain (UFG) alloy possessed appreciable corrosion resistance.

Therefore, it will be instructive to investigate whether complete alloying can occur in the Zr-Nb system by mechanical alloying, and also whether the processing technique has any effect on the type of phase(s) produced. In addition to study the possibility of extending the formation of amorphous phase in the Nb-Zr immiscible system at lower Zr concentrations. Additionally MA and SPS were used for the first time to synthesize a bulk nanophase Nb-Zr alloy. We envision that this new approach will pave the way for the development of Nb-Zr alloys for biomedical applications.

2.5 Mechanical Alloying

A number of non-equilibrium processing techniques have been developed during the last fifty years. These include rapid solidification processing of liquid metals at solidification rates of about a million degrees per second, and MA, a completely solid-state powder processing technique. Mechanical alloying involves repeated cold welding, fracturing, and rewelding of powder particles in a high-energy ball mill [7]. Both these techniques are capable of producing different types of metastable phases such as supersaturated solid solutions, crystalline and quasicrystalline intermediate phases and also amorphous phases. In cases where alloying cannot occur in the liquid state, rapid solidification processing technique is not useful to synthesize any alloys from immiscible metals. MA technique does not have to follow the phase diagrams and therefore, this technique will prove better-suited to synthesize novel metastable phases. Furthermore, the mechanical alloying technique is simple, versatile, and can be easily scaled-up. MA was reported to produce several advanced alloys and compounds as concluded in Figure 4 which is difficult to produce by conventionally casting or melting process [100].

To obtain a homogenous material synthesized by the MA process, the process parameters should be optimized. The properties of blended powders such as particle size distribution, amorphization, and the final stoichiometry depends on the process parameters. So that understanding these parameters will help to control the process parameters to obtain desired properties. A summary of these parameters is shown in the Figure 5.

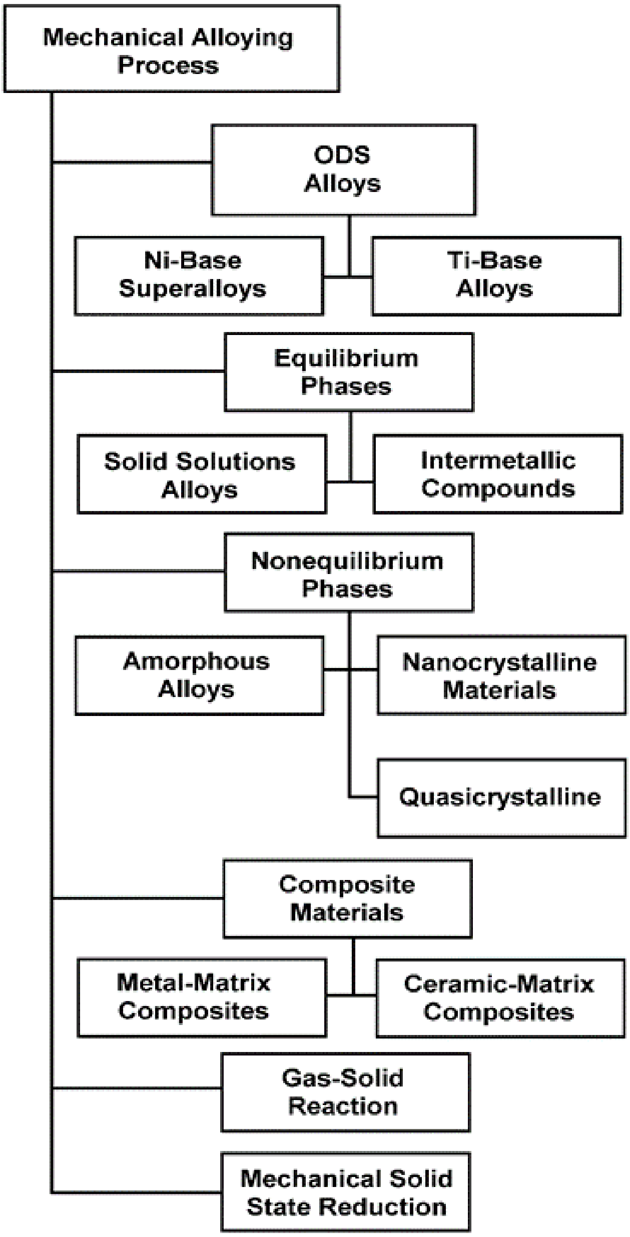

Figure 4 Applications of Mechanical alloying [100]

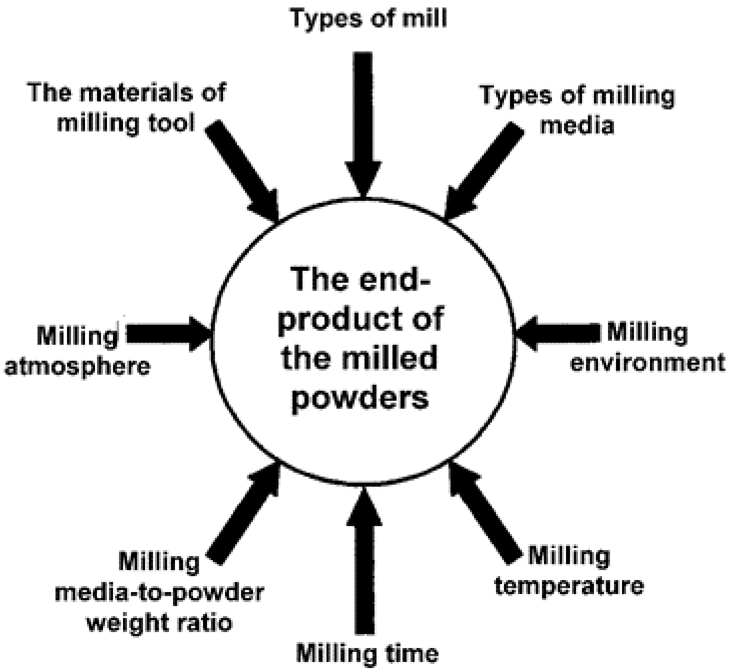

Figure 5 Main factors for mechanical alloying process [100]

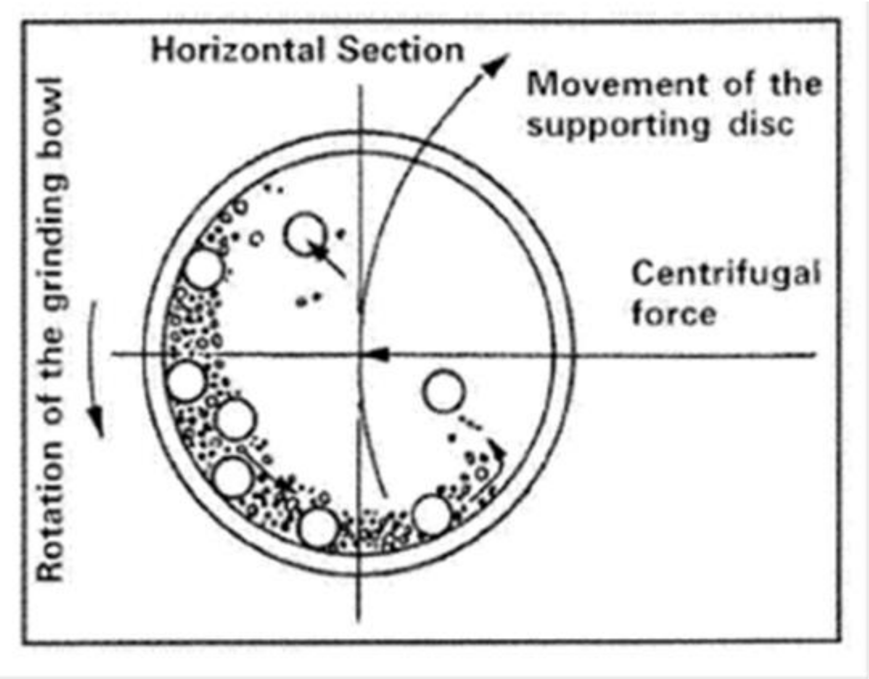

Figure 6 Ball motion inside a planetary ball mill [101]

The planetary ball mill manufactured by Fritsch GmbH in Germany was used in this work. Sample containers used in this mill are attached to a support disk and rotated around a central axis, the sample container itself also rotates about its own axis, in the opposite direction to the support disk. This combined action causes the centrifugal forces of the vials and support disk to act in alternating like and opposite directions. This causes the grinding media to run down the inside of the vial, causing a friction/grinding effect on the powders, and then when the media reach inboard location in the spinning vials, the centrifugal forces align and the media are propelled into the opposite wall, causing an impact effect on the powders [101]. This process is most easily visualized in Figure 6.

2.6 Spark Plasma Sintering

Historically, Humans have used the process of sintering for thousands of years. For example the ancient Egyptians were reported to sinter ceramics and metals by 3000 BC [102]. SPS also known as Field Assisted Sintering (FAST), Pulsed Electric Current Sintering (PECS) and Plasma Assisted Sintering (PAS), is a sintering technique where both external pressure and an electric field are applied simultaneously while avoiding grain growth during sintering at medium to high temperatures. The spark plasma process has many advantages over similar sintering techniques such as hot press (HP) sintering, hot isostatic pressing (HIP) or atmospheric furnaces [103-105].

One of the greatest challenges faced in powder metallurgy is identifying an appropriate sintering technique that can retain the developed microstructure while preventing or minimizing undesirable grain growth. Conventional sintering techniques usually lead to undesirable grain growth, reduced densification and loss of mechanical strength due to the long sintering time and high temperature required [106]. Among the sintering processes that have been developed thus far, SPS is proving to be effective in yielding fully dense metallic materials at relatively low temperatures and in very short sintering times [107,108]. Such conditions are capable of preventing/reducing grain growth and minimizing the formation of undesired secondary phases that degrade the properties. Moreover, the use of SPS is straightforward and does not require pre-compaction of the starting powder. With careful optimization of the sintering parameters, these techniques can be used to develop new materials with finer grain sizes compared to other conventional techniques [35].

Figure 7 show the Schematic of SPS process, the SPS machine consists mainly of vacuum chamber, top and bottom electrodes, DC pulse generator, units of pressure and temperature measurements.

The main four stages of SPS process are shown in Figure 8. Initially, the chamber is evacuated to create a vacuum, the second stage, is to apply the pre specified axial pressure, then apply the preprogramed thermal cycle in the third stage, and the cooling cycle in the last stage. In the SPS process, powders were loaded into a required graphite die and punch die. A thin graphite foil was used between powders and die to facilitate the sample ejection after sintering and to reduce the friction between the die walls and powders. The SPS experiments were conducted under vacuum. SPS parameters were programed: sintering pressure, sintering temperature, the heating rate, holding time, and cooling time. A thermocouple inserted in the die was used to measure the temperature.

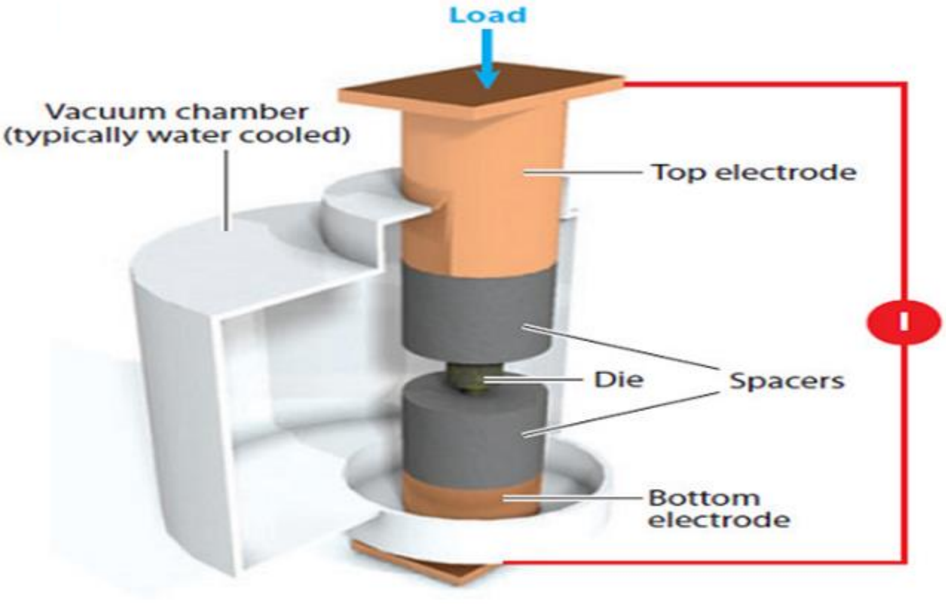

Figure 7 Schematic of the SPS apparatus [109]

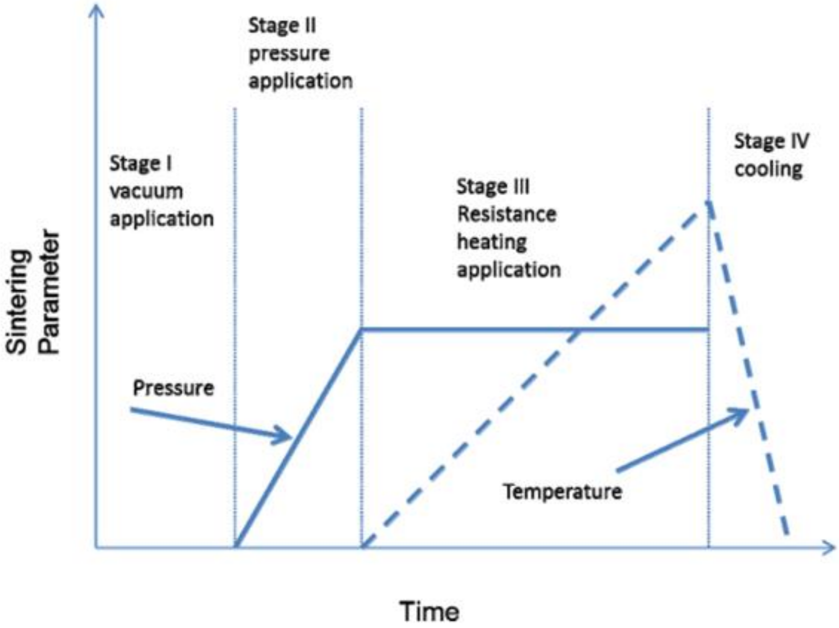

Figure 8 Stages of SPS Process [8]

Zhaohui et al. [110] proposed the mechanism of sintering in SPS: 1) activation and refining of the powder, 2) formation and growth of the sintering neck, 3) rapid densification and 4) plastic deformation densification. The activation and refining of the powder and the formation of the sintering neck stages are promoted by the spark discharge between particles as shown in Figure 9. The application of pressure and current, in addition to the high localized temperatures generated through resistance pulse heating improve heating rates and reduce sintering time and temperature leading to the consolidation of nanopowders without excessive grain growth [8].

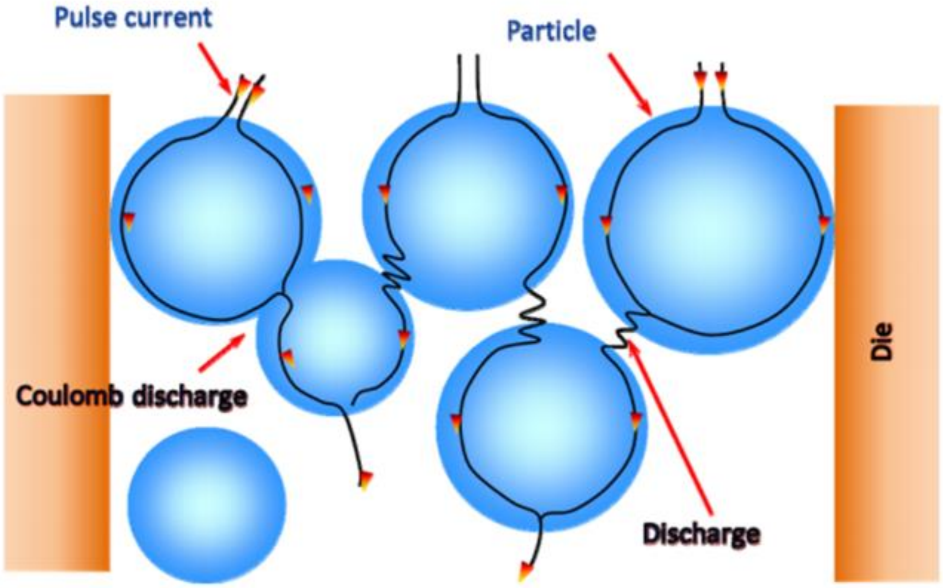

Figure 9 DC-pulse current flow through the particles [8]

CHAPTER 3

Experimental Techniques and Research Methodology

3.1 Experimental Procedure

3.1.1 Starting Materials

Elemental powders of Ti,Nb, and Zr (-325 mesh and 99.8 % metal base) provided by Alfa Aesar ,USA were used in this research. Material characterization of as received powder has been done using XRD and SEM, to assess the internal strain, the crystalline size, morphology, and particle size of these raw powders.

3.1.2 Synthesis of Alloys Using MA Process

NbZr and TNZ alloys have been synthesized using mechanical alloying technique. The powder mixtures were prepared in an atomic percentage to give the nominal compositions shown in Table 2. The mixture was weighed and loaded in tungsten carbide vials with tungsten carbide balls to give a BPR of 10:1 and 30:1 for selected compositions. The powders were MA under argon atmosphere in a planetary ball mill (Fritsch Pulverisett 5) with a rotational speed of 300 rpm. The PCA was not used to avoid contamination of the blended powders. The milling process were periodically paused half an hour every one hour to avoid excess heat in the vials. Moreover, the machine was stopped at regular intervals to remove the accumulated powders on the vial walls. At periodical interval, a small amount of the powder was taken out for characterization.

Table 2 Compositions of alloys studied

Alloy	Nominal compositions at %
Nb-xZr X= (5, 10, 15, 20, 40, 45, and 50 at %)	95Nb–5Zr
	90Nb–10Zr
	85Nb–15Zr
	80Nb–20Zr
	60Nb–40Zr
	55Nb–45Zr
	50Nb–50Zr
Ti-Nb-Zr	Ti20Nb13Zr

3.1.3 Consolidation of Alloys

The mechanically alloyed powders were compacted using the non-conventional techniques of Spark Plasma Sintering (SPS). The SPS machine (FCT system-model HP D5, Germany has been used. MA powders were loaded into 20 mm graphite die and punch die. A thin graphite foil was used between powders and die to facilitate the sample ejection after sintering and to reduce the friction between the die walls and powders. The SPS experiments were conducted under vacuum. The samples were sintered at a pressure of 50 MPa. A thermocouple inserted into the die was used to measure the temperature. After SPS, the sample was grounded and polished to remove the surface contamination from carbon. The SPS process parameters were varied as shown in Table 3.

Table 3 Parameters used in SPS

SPS parameters	**60Nb–40Zr at % alloy**	**Ti20Nb13Zr at %alloy**
Temperature (°C)	1300,1400,1500	800,900,1000,1100,1200
Holding Time (min)	10,15,25	10
Heating Rate (ºC/min)	50,100	100
Pressure (MPa)	50	50
Atmosphere	Inert Argon	Inert Argon
Sample dimensions (mm)	20*4 (diameter * height)	20*4 (diameter * height)

3.2 Characterization of the MA Powders and Consolidated Samples

3.2.1 Sample Preparation

The milled powder samples were gold coated to enhance the conductivity and the resolution of obtained images for SEM and FE-SEM. The SPS samples were coarse grounded to remove the surface contamination from carbon then grinded till Grit 600, and then the samples were polished using monocrystalline diamond suspension (provided by Buehler) from 6 μm till 250 nm , ended by fine polishing using alumina suspension with 50 nm. After polishing, the TNZ samples, were etched with 10% HF solution and NZ samples were etched using 10% HF,40% HNO3,and 50% H2O for 5 seconds .

3.2.2 X-Ray Diffraction (XRD)

At periodic intervals, samples of powders have been taken out to monitor the phase evolution by XRD. From the XRD patterns it will be possible to determine the nature of phases formed, and the lattice parameters of the phase(s).By following the variation of crystallite size and lattice parameter as a function of milling time, we will be able to correlate the phase evolution to the processing parameters.

Both of the as received , milled powder at different intervals as well as SPS samples were characterized by XRD (AXS D8 Bruker machine, Germany)using Cu Kα radiation (λ = 1.542 A°) and scanning speed of 1 degree/minute. The Scherer relation and Williamson-Hall formula was used to estimate the crystallite and internal strain:

$$\beta \cos \Theta = \eta \text{ Sin } \Theta + 0.9\lambda/D \text{ [7]} \qquad (3.1)$$

Where β is the full width at half maximum of XRD peaks, Θ is the diffraction angle, η is the internal strain, λ is the wavelength of X-ray beam and D is the mean crystallite size.

The XRD results of both as-received and milled powders were used for calculating the percentage of amorphization using the EVA software available with the X-ray diffractometer. First, remove the background that represents air scatter, incoherent scatter. Then, the remaining is from crystalline and amorphous contribution only. The Percent crystallinity was calculated from the equation (3.2), finally the percent of amorphous phase is the complement of the percentage of the crystallinity.

$$X_{cr} = \frac{I_c \times 100}{I_c + I_a} \qquad \text{[111]} \qquad (3.2)$$

3.2.3 Scanning Electron Microscopy (SEM)

The SEM (JEOL JDX 3530 LV, Japan) and FE-SEM, (Tescan Lyra-3) combined with EDX were used to observe the morphology, grain size refinement of the milled powders, microstructures, and chemical compositions of SPS samples. In addition, the chemical compositions of alloys was examined by EDS (Oxford Inc., UK) and mapping attached to the SEM.

3.2.4 Transmission Electron Microscopy (TEM)

The microstructures were also observed on TEM: Tecnai G Series operated at 200 keV) and JEOL (200 KeV) to reveal the details of the obtained phases. A bright-field (BF) image is obtained by allowing only the transmitted beam to pass the objective aperture. A diffraction pattern is formed on the back-focal plane of the objective lens when an electron beam passes through a crystalline specimen in a TEM. The diffraction pattern represents a reciprocal lattice plane with reciprocal lattice points. Electron diffraction (SAD) could be used to generate images of diffraction contrast and for crystal structure analysis.

BF images were used reveal the different phases and to measure the average grain size. In addition the indexing of the SADP have been done to identify the different phases formed: The amorphous phase, crystal structure and the lattice parameter of the crystalline phase.

3.2.5 Phase Transformations of Milled Powders

Phase transformations of milled powders have been evaluated using DSC. The thermal analyzer STA 449F3-Jupiter was used. Alumina crucible at a heating rate of 10 K/min under Ar atmosphere, and the temperature was varied in the range from ambient till 1200 ºC. DSC provides an important tool to investigate the thermal stability of synthesized alloys, structure and phase transformations.

3.2.6 Density Measurements

The density determination kit (METTLER TOLEDO) was used to measure the density of sintered samples based on Archimedes’ principle. The polished sample was weighed in the air and then in distilled water, then the formula (3.3) has been used to calculate the density of SPS sample. The reported value, was the average of three measurements.

$$\rho = \frac{A}{A-B}(\rho 0 - \rho L) + \rho L \text{ [112]} \tag{3.3}$$

Where, A is the weight of the sample in air, B is the weight of the sample in water, ρ_0 is the density of the water, and ρ_L is the density of air (0.0012 g/cm^3).

3.2.7 Mechanical Characterization

The nanoindenter tester and microhardness tester have been used to assess the mechanical properties of consolidated samples.

3.2.7.1 Microhardness

Microhardness test has been done to assess the mechanical properties of samples. A hardness tester (Buehler, USA) with 2000 g, and 500g load and 10 s dwell time was used to measure the Vickers microhardness of the consolidated samples after grinding and polishing. The reported value was the average of ten measurements along the cross section of the sample.

3.2.7.2 Nanoindentation

Nanoindentation has been conducted to measure/ assess the mechanical properties of SPS samples. The nanoindenter tester (CSM Instruments SA in Switzerland) was used at room temperature. The indenter tip used was a diamond four sided pyramid Vickers indenter. The maximum load used of 100 mN, loading and unloading rate of 100mN/min, and pause time of 5 sec was used. The tip has a Poisson ratio of 0.07 and young’s modulus of 1140 GPa. Samples were polished to a surface like mirror with 3 µm, 1µm, and 250 nm monocrystalline diamond suspension ended with 50 nm Alumina. An array of 3*3, 80 µm apart was used. The mechanical properties were obtained using the model developed by Oliver WC, Pharr [113].

$$\left(\frac{1}{\mathrm{E}}\right)r = \left(\frac{1-\vartheta^2}{E}\right)I + (\frac{1-\vartheta^2}{E})S \quad [113] \tag{3.4}$$

Where E_r is the measured value (reduced modulus). The Poisson ratio was assumed to be 0.428 for β-Ti [114], ~0.324 for α-Ti [115–117], and the average value has been used for the average mechanical properties of the tested material.

CHAPTER 4

RESULTS AND DISCUSSION

4.1 Characterization of as Received Powders

XRD pattern of raw powders Ti, Nb and Zr is presented Figure 10 All the expected peaks from pure Ti, Nb, and Zr are clearly presented in the patterns. The Williamson-Hall formula was used to estimate the crystallite size and internal strain. The crystallite size of Ti,Nb and Zr are 51.4 nm,55.512 nm, 57.825 nm while the strain of them are 0.0016,0.0019, 0.0028 respectively. Figure 11 shows the morphology of as received powders, the shape of particles shown in the SEM images of Ti, Nb, and Zr are irregular.

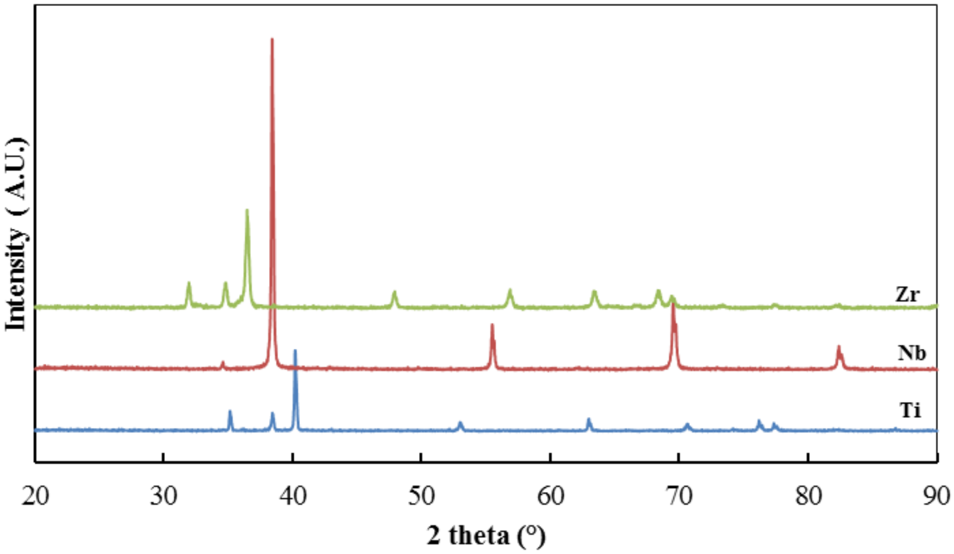

Figure 10 XRD patterns of as received powders

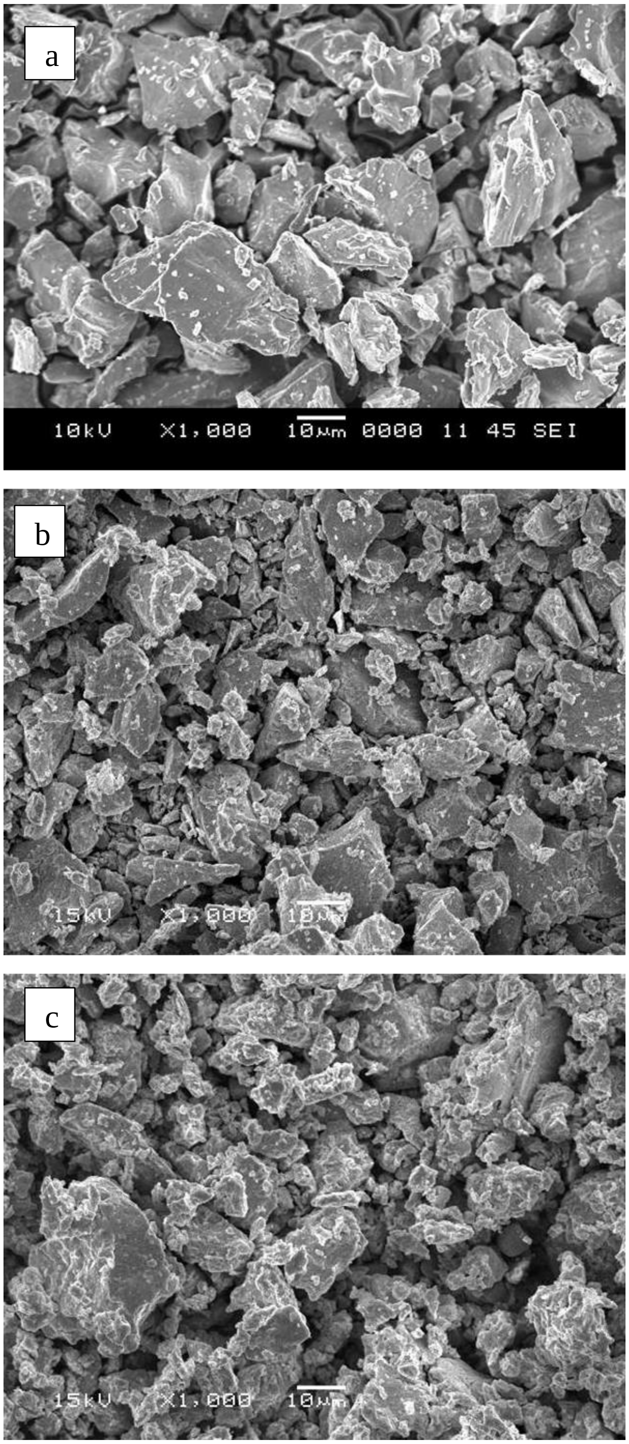

Figure 11 SEM micrograph of as received powders: (a) Ti, (b) Nb, and (c) Zr

4.2 Binary Nb-Zr System

NbZr alloy with different compositions, Nb-xZr, x= (5, 10, 15, 20, 40, 45, and 50 at %) has been MA using the ball mill machine. The ball mill processing parameters; milling time, and BPR have been varied to study their effect on the phase evolution. After conducting the detailed study of the phase evolution during the MA, Nb–40 at. % Zr milled powder was consolidated using SPS process. The SPS processing parameters; temperature, holding time, and heating rate has been varied to study its effect on the resulting structure, microstructure, densification, and mechanical properties.

4.2.1 Phase Evolution Studies (1)

For the MA NZ powders, XRD, and TEM were used to study the phase evolution, and determine the crystal structure of the phases Figure 12 shows the XRD patterns of the Nb–40 at. % Zr milled powder. The as-mixture powder shows the presence of elemental Nb and Zr only and no other phase is present. On milling the powder, the intensities of the diffraction peaks of both the metals decreased and their widths increased due to a reduction in crystallite size and introduction of lattice strain [7, 64]. However, on continued milling of the powder blend to about 10 h, the diffraction peaks were replaced by a broad diffuse halo, corresponding to the (110) peak of Nb, suggesting that an amorphous phase had partially formed. The fraction of the amorphous phase increased with milling time reaching a maximum of about 60 vol.% on milling the powder for 10 to 20h. However, on continued milling to 70 h, a crystalline phase had formed, suggesting that the amorphous phase had crystallized due to milling,

---

(1) **Published**: N. Al-Aqeeli, C. Suryanarayana, and M. A. Hussein, “Formation of an amorphous phase and its crystallization in the immiscible Nb–Zr system by mechanical alloying,” J. Appl. Phys., vol. 114, no. 15, p. 153512, 2013.

a phenomenon that has been termed mechanical crystallization [86,118]. A similar trend was noted on milling the powder blends of the compositions (55 Nb-45Zr, and 50Nb-50Zr at. %) as shown in Figure 13 and in Figure 14.

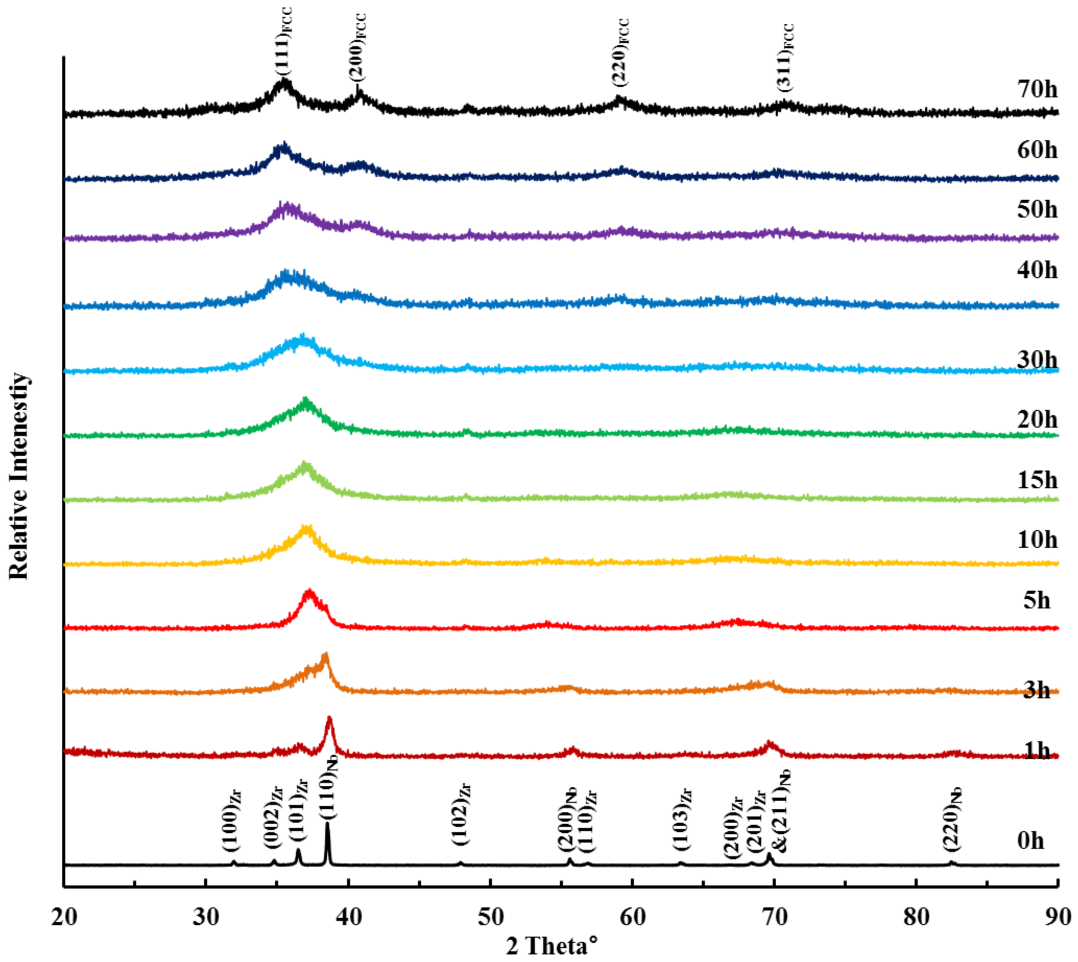

Figure 12 XRD patterns of the as received and milled Nb–40 at.% Zr powder: While the starting (unmilled powder) showed only the diffraction peaks from both Nb and Zr, the milled powder showed a decrease in peak intensity and an increase in peak width due to reduction in crystallite size and introduction of lattice strain. An amorphous phase started to form on milling the powder for about 10 h, and its volume fraction increased with increasing milling time. On milling the powder for 50–70 h, a crystalline fcc phase had formed.

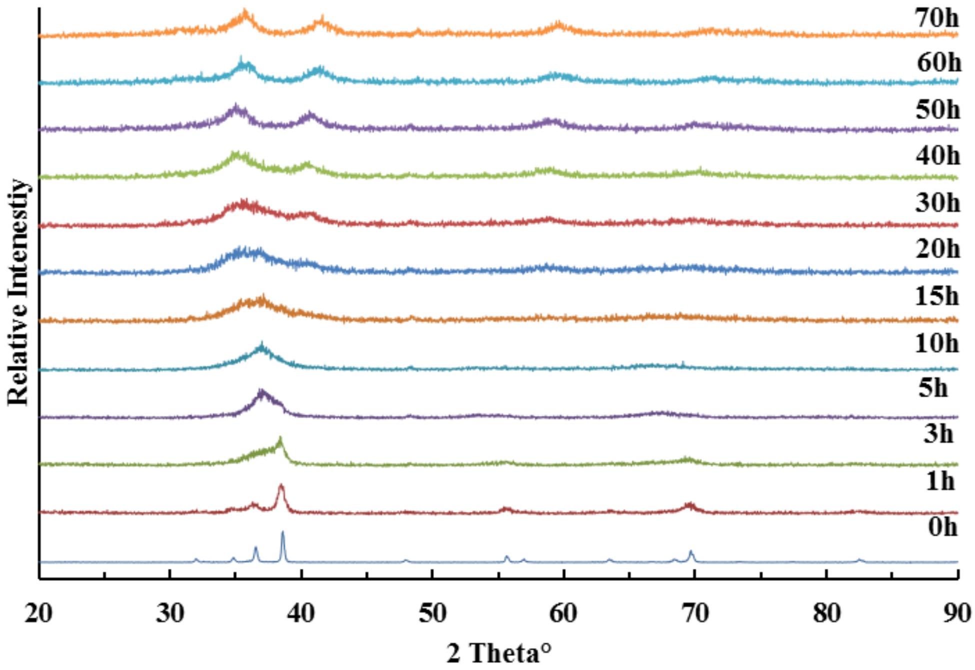

Figure 13 XRD patterns of the as received and milled Nb–45 at.% Zr powder

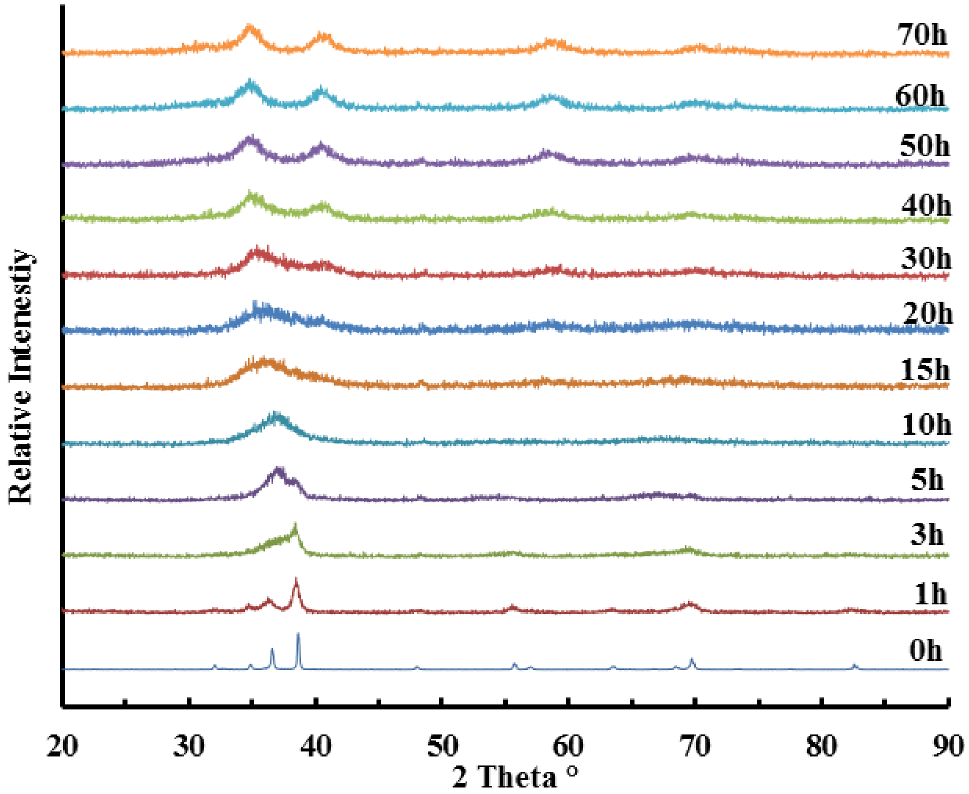

Figure 14 XRD patterns of the as received and milled Nb–50 at.% Zr powder

Figure 15 and Figure 16 show TEM micrographs and SADP of the Nb–40 at.% Zr powder blends milled for 10 and 70 h. Some regions in the powder milled for10 h clearly showed the presence of an amorphous phase. This is confirmed from the high-resolution TEM micrograph that shows the salt-and-pepper like the contrast (Figure 15 -a) and the presence of a broad diffuse halo in the diffraction pattern (Figure 15 b). This observation clearly confirms that it has been possible to produce an amorphous phase in this immiscible Nb-Zr system. But, the electron micrograph of the powder milled for 70 h clearly shows the presence of lattice fringes suggesting that a crystalline phase is present at this stage (Figure 16 a) and the diffraction pattern (Figure 16 b) clearly confirms the presence of a crystalline phase. From the position of the rings, this crystalline phase has been indexed to have an FCC structure with a = 0.44 nm. The formation of a crystalline phase on continued milling after the formation of the amorphous phase clearly suggests this could be due to mechanical crystallization [118].

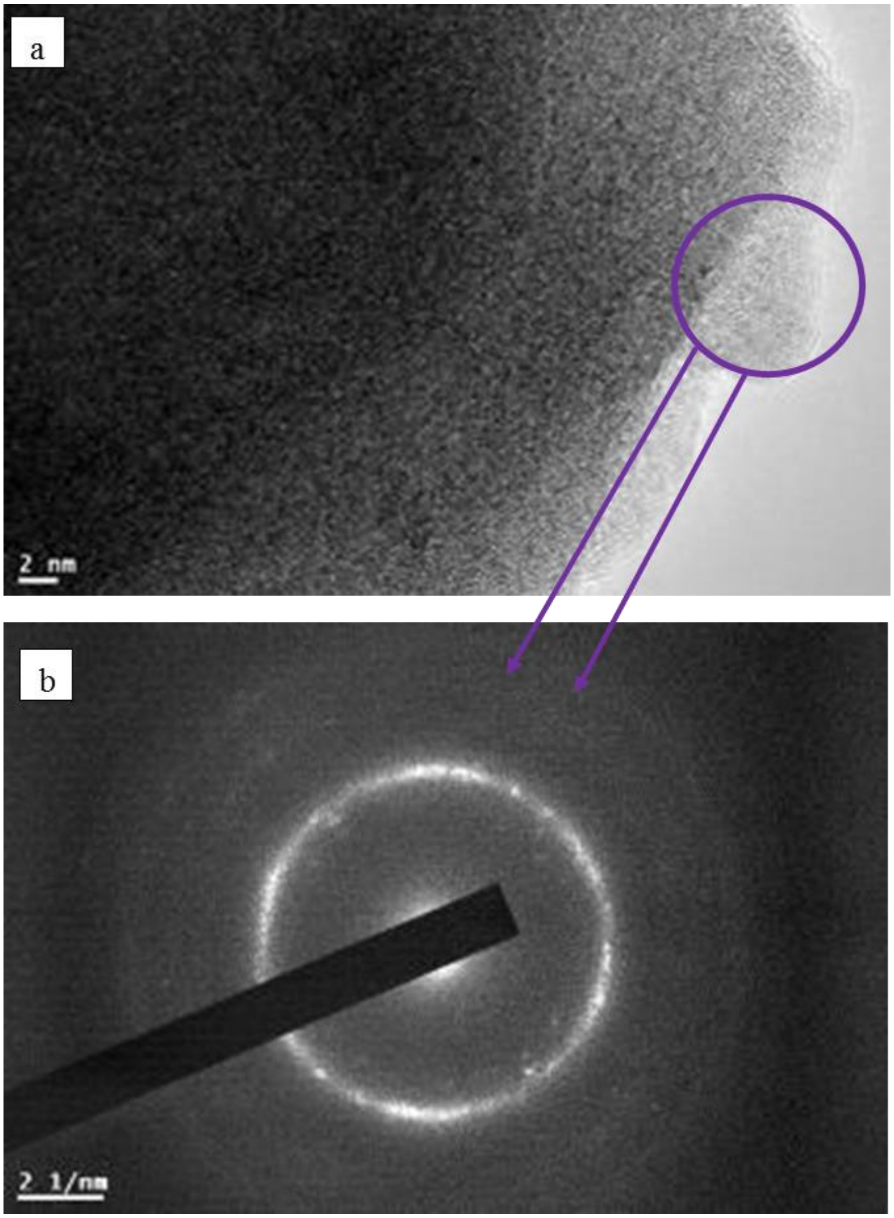

Figure 15 TEM images of the Nb-40 at. % Zr powder milled for 10 h: a) BF and b) SADP. The micrograph (a) shows the presence of the amorphous phase, confirmed by the diffraction pattern showing a halo (b)

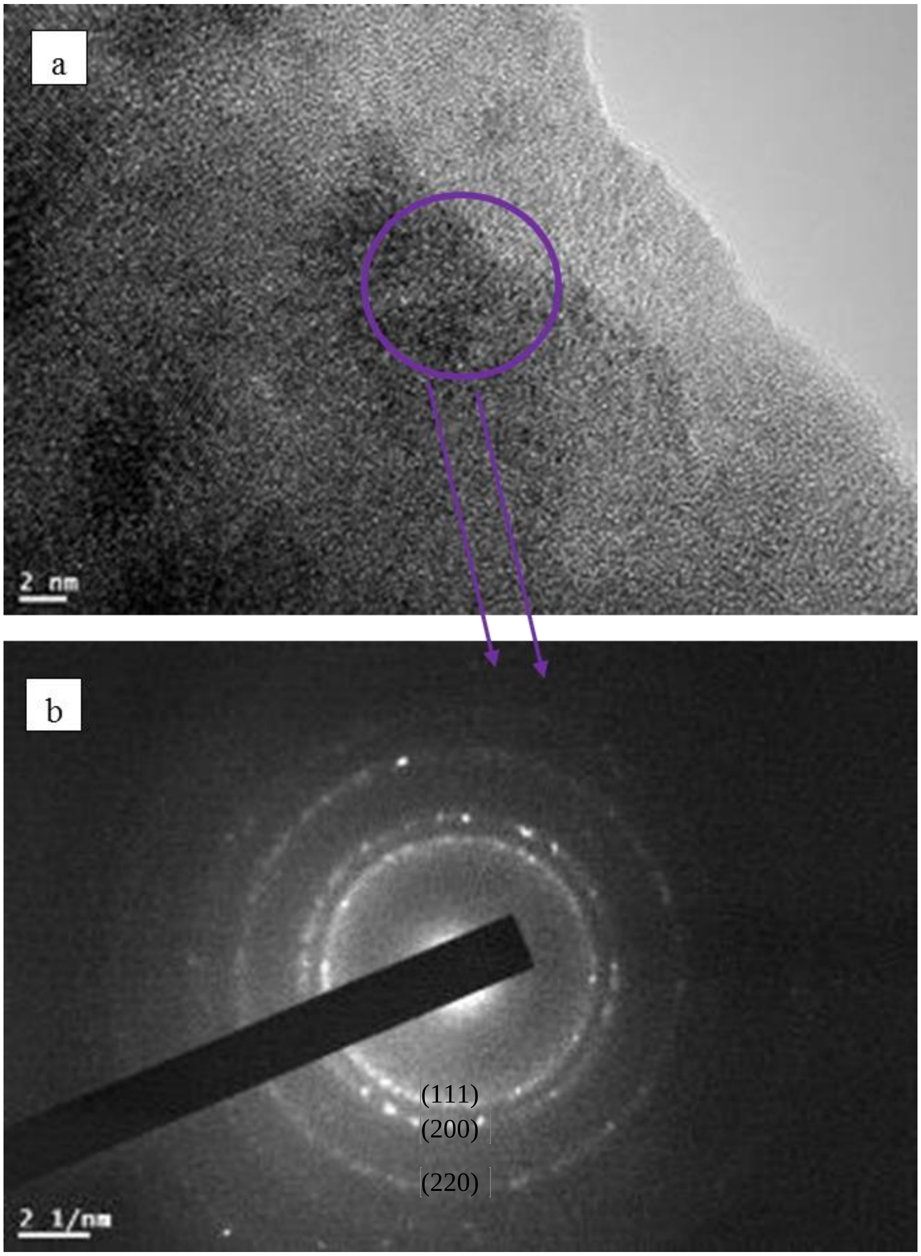

Figure 16 TEM images of the Nb-40 at. % Zr powder milled for 70 h: a) BF and b) SAD .the micrograph (a) shows the presence of the fcc crystalline phase, confirmed from the diffraction pattern (b).

4.2.2 The Quantification of Amorphous Phase

Since the samples contained a mixture of the crystalline and amorphous phases, the fraction of crystallinity in the samples was calculated according to the method suggested by Soltys et al. [119] and Majdanac et al. [120] and explained previously in 3.2.2 section.

Figure 17 presents the percentage amorphization as a function of milling time in the three samples. The percentage of amorphization in the milled powder increased with milling time. The percentage amorphization exhibited a maximum value at a milling time of 15-20 h, and it decreased with further milling when mechanical crystallization had occurred. Simultaneously, the percentage amorphization had increased with an increase in the Nb content. This can be rationalized on the basis that Nb has a higher melting temperature than Zr and therefore the time required for amorphization increased with increasing Nb content.

It may, however, be mentioned in this context that these values are likely to indicate only the trends and that too much importance should not be attached to the quantitative values.

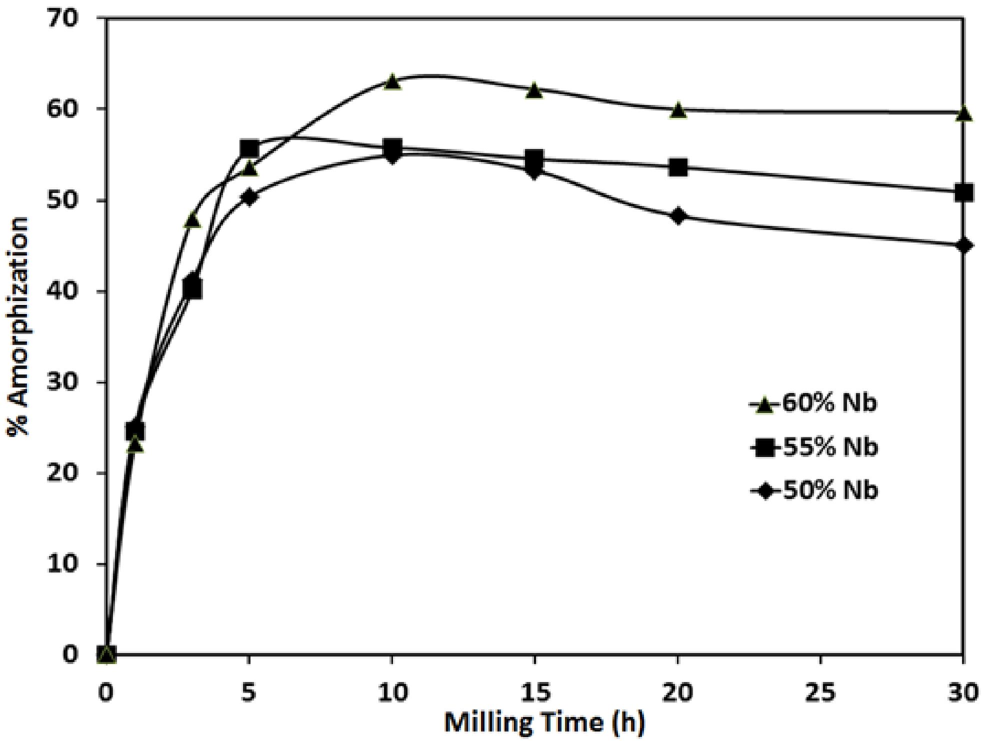

Figure 17 Variation in percentage of amorphization for the different Zr-Nb powders with the milling time

4.2.3 Crystallization of the Amorphous Phase

It was also mentioned that a crystalline phase had formed on continued milling after the amorphous phase had formed. There have been several reports of similar observations[118].The crystalline phase could be a metastable or equilibrium phase formed as a result of decomposition of the amorphous phase or it could be a contaminant phase. The technique of MA could always introduce contamination into the milled powder due to wear and tear of the grinding medium, use of a PCA, or atmospheric contamination. Chemical analysis of the milled powder showed that the carbon and nitrogen contents were zero on milling the powders for 10h, however the powder milled for 70 h showed the presence of about 1.1 wt. % W. The presence of W in the milled powder can be attributed to the use of very hard WC vial and balls, which show much less wear and tear than stainless steel balls, which are much softer than those of WC. Also, IBM of multilayer thin films will not have contamination during processing. Since these films subjected to IBM also showed the presence of two metastable crystalline phases, both having the FCC crystal structure [55], we can conclude that the amorphous phase had crystallized to form a metastable crystalline phase. Further, in the IBM case, the lattice parameter of the Nb-rich Nb-19 at. % Zr FCC phase was reported to be 0.435 nm, while that of the Zr-rich Zr-32 at. % Nb FCC phase was 0.440 nm. In our alloy with Nb-40 at. % Zr, the lattice parameter was 0.44 nm, very close to the value reported earlier in IBM alloys. Thus, it is safe to infer that this FCC phase is not a contaminant phase, but that which has formed as a result of crystallization of the amorphous phase. The reasons for the formation of the crystalline phase on continued milling of the amorphous phase have been detailed earlier [118]. The lowered free energy of the system consisting of a mixture of amorphous and crystalline phases, in comparison to an amorphous phase has been shown to be the reason for the crystallization of the amorphous phase.

4.2.4 Comparison with Related Observations

An exhaustive review of the literature on the formation of metastable phases, including amorphous phases, in immiscible systems has been presented by Ma [121]. It was noted that amorphization was possible even in alloy systems that exhibited positive heat of mixing. These systems include Ag-Cu [122], Cu-Nb, [123], Cu-Ta, [77,124] among other immiscible systems. In all these alloy systems, an amorphous phase is produced through mechanically-driven solid–state amorphization methods, e.g., cold rolling or cold drawing of multilayer thin films. An important point to be noted is that, in all these systems, amorphization has been only partial and that a homogenous amorphous phase was never obtained. Such as, the amorphous phase is observed only at the Cu/Nb interfaces in the Cu-Nb system [123] and in localized regions in the Ag-Cu system [122]. In majority of the cases, formation of the amorphous phase was confirmed only through XRD experiments. It is possible that these are only “X-ray” amorphous and additional experiments such as TEM and calorimetric measurements could help in determining whether these phases are truly amorphous. This is because the broad peaks in XRD patterns could result from (i) extremely fine crystalline grain structures or (ii) very fine crystals distributed uniformly inside an amorphous matrix. But, in the present investigation, we were able to confirm the presence of the amorphous phase through both XRD and TEM methods and therefore this lends more credibility to the reported result.

The formation of amorphous phases in immiscible alloy systems has been reported to occur through methods such as IBM, MA or cold rolling of multilayer films, but not through rapid solidification processing methods. In severe plastic deformation methods, a very large number of new surfaces and interfaces are created. This excess interfacial energy provides the driving force for amorphization, because it promotes the free energy of the system containing the crystalline phases (solid solutions or intermetallics) to above that of the hypothetical amorphous phase.

4.2.5 Extending the Composition Range for an Amorphous Phase in the Nb-Zr system (2)

According to [125], theoretically the formation of an amorphous phase in this system should be limited to Zr values exceeding 37.4%. To investigate the possibility of extending the composition range for the formation of an amorphous phase in the Nb-Zr system to lower Zr concentrations, powder blends containing 5, 10, 15 and 20 at.% Zr were milled. Figure 18 and Figure 19 show the XRD patterns at different milling intervals for $Nb_{80}Zr_{20}$ and $Nb_{95}Zr_5$. It was observed that broadening of the diffraction peaks occurred after 10 h of milling, related to the reduction in crystallite size and increase in lattice strain. As the milling time increased the intensity of the peak corresponding to $(110)_{Nb}$ is decreased and shifted to a lower angle indicating lattice expansion and formation of a solid solution. This shift appeared as early as 10 h of milling in $Nb_{95}Zr_5$, while it occurred at 20 h in $Nb_{80}Zr_{20}$. It was also noted that in all the powder blends, the FCC phase had formed with increased milling time up to 70 h. However, the lattice parameters of the new FCC phase were 0.435439 nm, 0.435169 nm, 0.433484 nm, and 0.431644 nm for the nominal compositions of $Nb_{80}Zr_{20}$, $Nb_{85}Zr_{15}$, $Nb_{90}Zr_{10}$, and $Nb_{95}Zr_5$, respectively. It appears from these results that no pronounced amorphous phase formation was achieved at these milling conditions, suggesting that the current milling conditions were not intense enough to destabilize the crystalline phase and allow the formation of an amorphous phase. This is despite the fact that severe plastic deformation, in general, facilitates the formation of an amorphous phase due to the introduction of fresh interfaces, which raise the free energy of the system.

---

(2) **Published** :N. Al-Aqeeli, M.A. Hussein, C. Suryanarayana, Phase evolution during high energy ball milling of immiscible Nb–Zr alloys, Advanced Powder Technology, 26 (2015) 385–391

In this case, however, it appears that the increase in free energy of the crystalline phase was not sufficient to exceed that of the hypothetical amorphous phase; thus only solid solutions were formed.

To investigate if higher milling intensities, through increased BPR, could facilitate the formation of the amorphous phase, two powder blends, namely $Nb_{80}Zr_{20}$, and $Nb_{95}Zr_5$ were milled at a BPR of 30:1. Figure 20 and Figure 21show the X-ray diffraction patterns of the powders milled for up to 20 h. The results show that in addition to reduced intensity and broadening of the peaks, Nb(Zr) solid solution appeared, at times shorter than when milled at a BPR of 10:1. This can be attributed to the higher energy imparted to the milled powders. Moreover, the shift in $(110)_{Nb}$ peak towards a lower angle in $Nb_{80}Zr_{20}$ appeared as early as 1 h of milling, which is relatively short. Other studies [72, 126] have reported similar early shifts in different systems which support such possibilities. The more interesting observation, however, is related to the partial formation of an amorphous phase in both the compositions at a milling time of 5-10 h. Similar to the powders milled at a lower BPR, the metastable FCC phase was formed in both compositions at longer milling times, with the caveat that the FCC phase had formed at an earlier time due to higher energy imparted to the powders. Upon reaching the metastable FCC phase, the milling experiments were stopped for higher BPR at 20 h. Such results indicate that adjusting the milling conditions is vital in pushing the system towards higher instability and subsequent amorphization. As for the indications of amorphization in the work of Suryanarayana and Liu [88], it was possibly due to the fact that their experiments were carried out using a SPEX 8000 mill, which is considered as the highest intensity commercial mill available. However, the occurrence of an amorphous phase was still minimal at these lower Zr concentrations and further milling enabled the formation of the FCC phase. Confirmation of the amorphous phase formation in these compositions was obtained through TEM investigations.

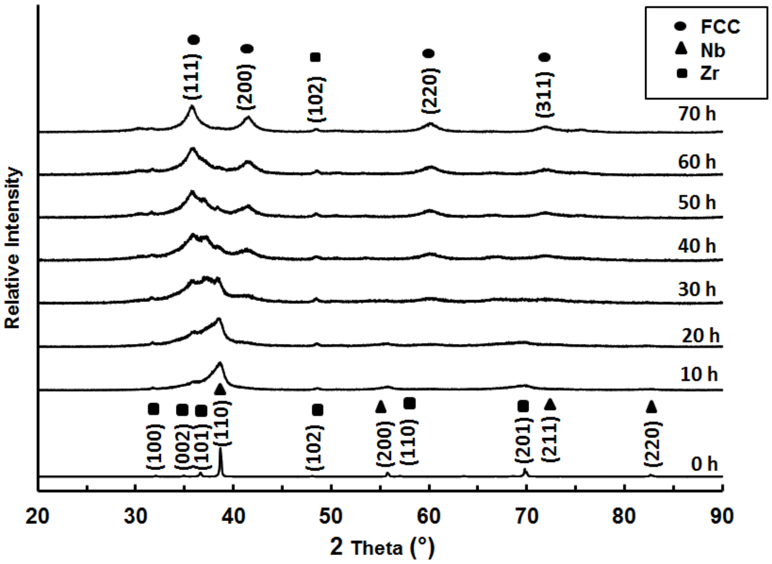

Figure 18 XRD patterns of Nb80Zr20 powders MA at a BPR of 10:1

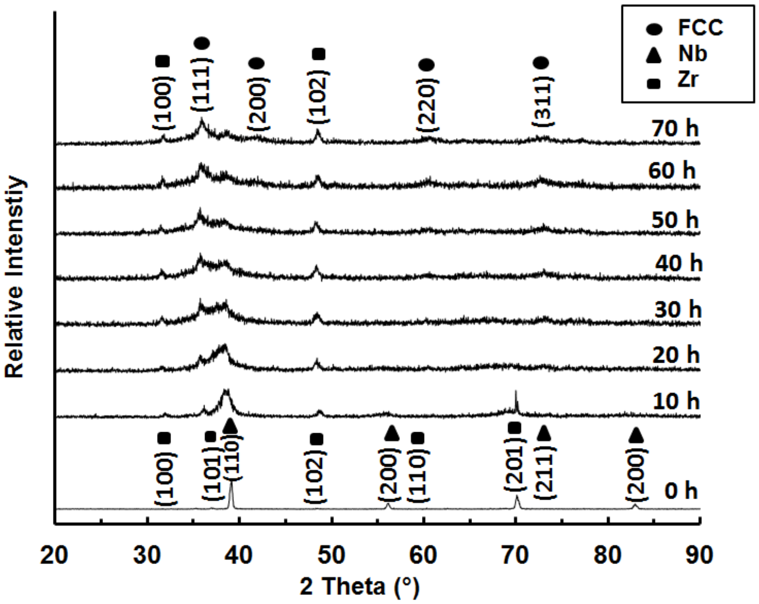

Figure 19 XRD patterns of Nb95Zr5 powders MA at a BPR of 10:1

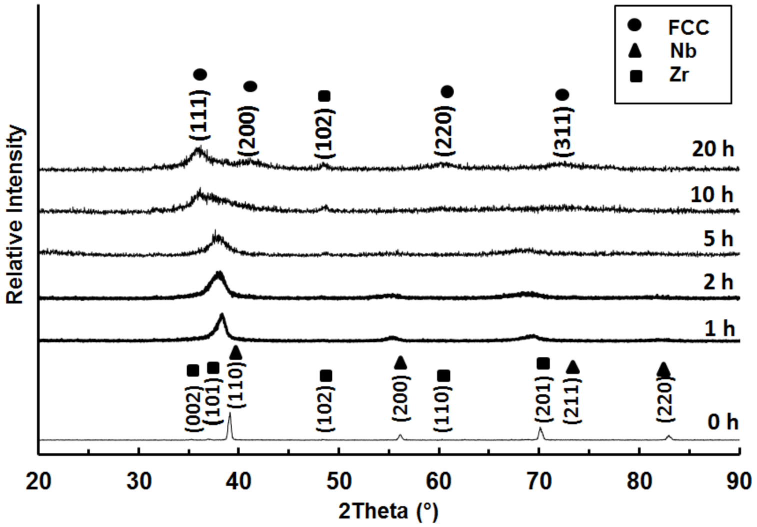

Figure 20 XRD patterns of Nb80Zr20 powders MA at a BPR of 30:1

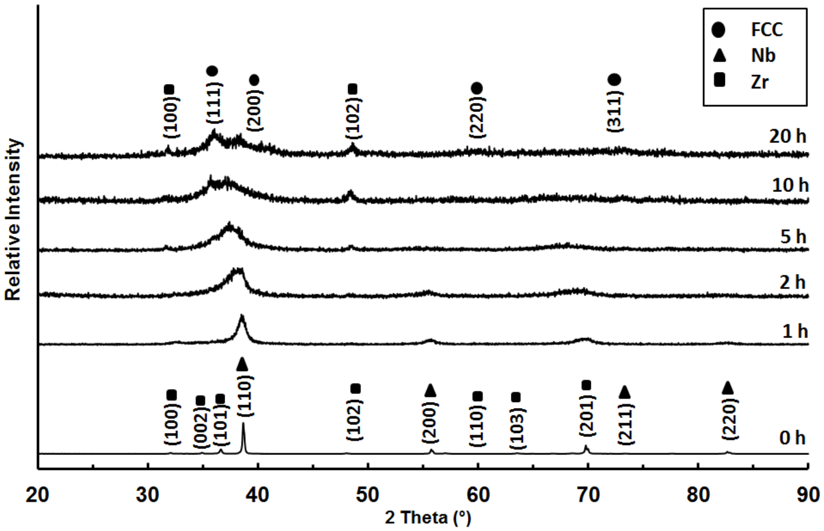

Figure 21 XRD patterns of Nb95Zr5 powders milled at a BPR of 30:1

To confirm the XRD results regarding the formation of an amorphous phase, we have also conducted direct TEM studies. Figure 22 shows the TEM images and SADP of the $Nb_{80}Zr_{20}$ and $Nb_{95}Zr_5$ powder milled for 10 h BPR 30:1, respectively. Figure 22(a) shows that there exist sharp diffraction rings indicative of the presence of a crystalline phase in the $Nb_{80}Zr_{20}$, nevertheless, the sharpness of these rings seemed somewhat less compared to that from the $Nb_{95}Zr_5$ powder milled for 10 h (Figure 22(b)). This can also be confirmed by TEM images in which the salt-and-pepper like contrast was observed in some areas of the TEM micrographs of the $Nb_{80}Zr_{20}$ powders milled for 10 h. However, the strong crystallinity of the sample $Nb_{95}Zr_5$ milled for 10 h was evident by the observed lattice fringes in the image and the absence of any indications of an amorphous phase. This suggests the coexistence of amorphous and crystalline phases in the $Nb_{80}Zr_{20}$ powders milled for 10 h. These results support the XRD observations. The stability of this amorphous phase appears to be minimal since further milling caused crystallization of the amorphous phase. However, it appears that obtaining a higher proportion and more stable amorphous phase is not easily attained at lower Zr concentrations, even with far-from equilibrium processing methods in the Nb-Zr system; except for Ion beam mixing (IBM).

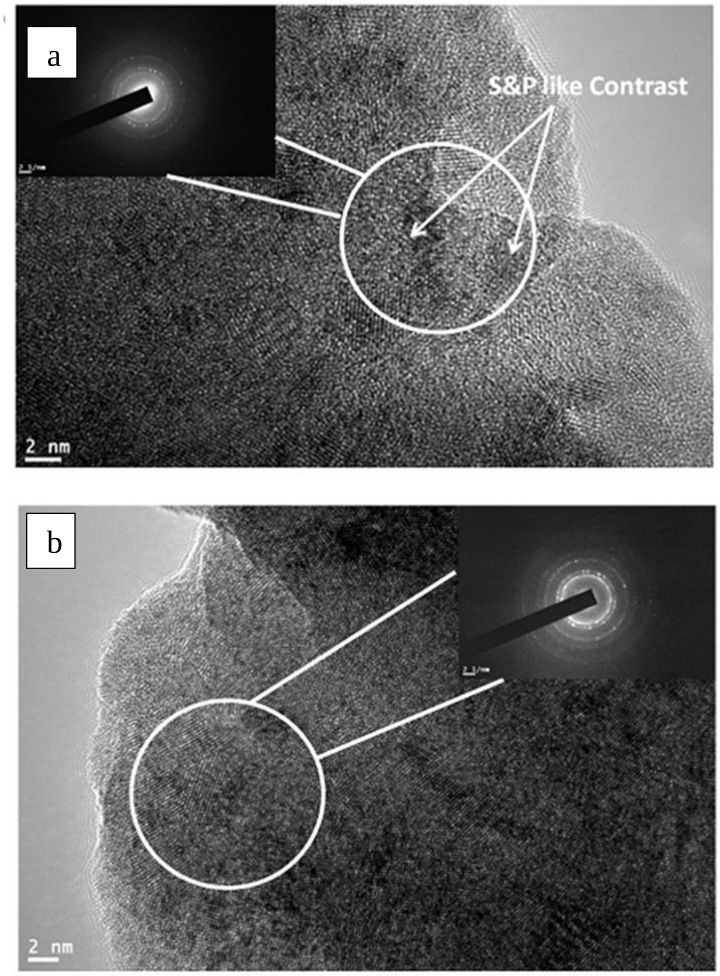

Figure 22 TEM BF micrographs and SADP of Powders MA for 10 h at a BPR of 30:1 (a) Nb80Zr20 (b) Nb95Zr5powders milled for 10 h,

4.2.6 Lattice Parameters

Figure 23 presents the variation of lattice parameter with the milling time and BPR for the Nb(Zr) solid solution. An interesting observation is the shortened milling time for achieving the same lattice parameter value at a higher BPR. For example, the lattice parameter that was achieved at 70 h milling at a BPR of 10:1 was realized at 20 h when the BPR was increased to 30:1. As the solute atoms of Zr dissolve in the lattice of Nb forming Nb(Zr) solid solution, they are expected to increase the lattice parameter of Nb since Zr has a larger atomic radius of 0.158 nm compared to the atomic radius of 0.146 nm for Nb. Since the lattice parameter is the same in both cases, this suggests that the maximum solid solubility of Zr in Nb would be similar in both compositions. These results show the difficulty in forming a higher fraction of amorphous phase at lower Zr concentrations and the stability of Nb(Zr) solid solution, which is different than what was suggested by Wang et al. [56].

The Vegard's law was used to estimate the Zr solute content in the resulting solid solutions assuming the model of an ideal solid solution. Figure 24 shows the variation of lattice parameter versus composition of the powders MA for different time periods. For the purpose of comparison, the linear interpolation between the lattice parameters of Nb and Zr are included. The lattice constant of the Nb pure metal is 0.33717 nm and that of a hypothetical BCC–Zr phase is 0.3648 nm (calculated by using the atomic diameter of the HCP Zr crystal). As is clear from the figure, the alloys obey the Vegard's law with a visible deviation that could be related to the heat of mixing between the two elements.

Generally, amorphous phases were reported to form easily in the middle of the phase diagram [56, 59], i.e., when the composition of the alloy is near equiatomic. Therefore, it is not very surprising that amorphous phases have formed in this alloy system also at high Zr contents, even when milled at a BPR of 10:1.

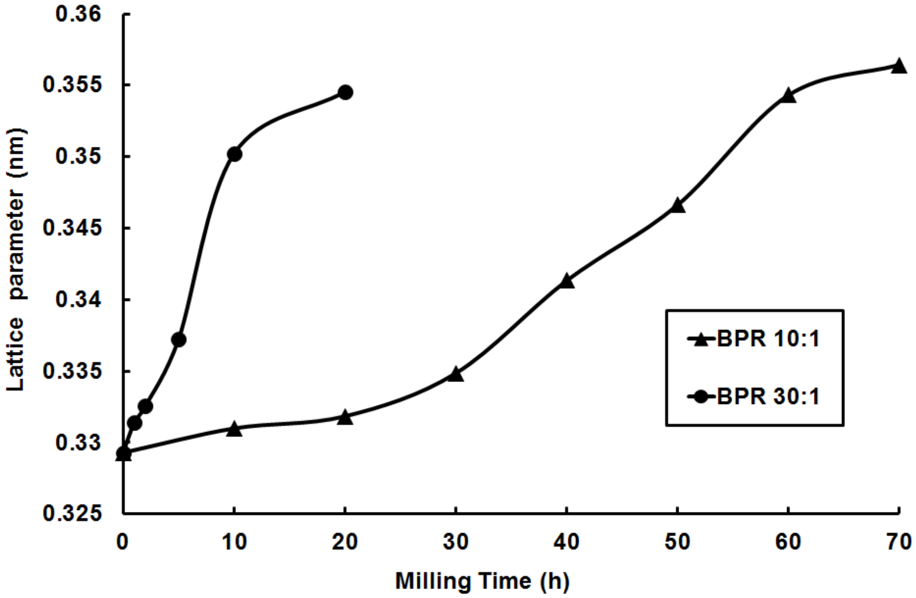

Figure 23 Lattice parameter of Nb(Zr) solid solution as a function of milling time for the MA Nb80Zr20

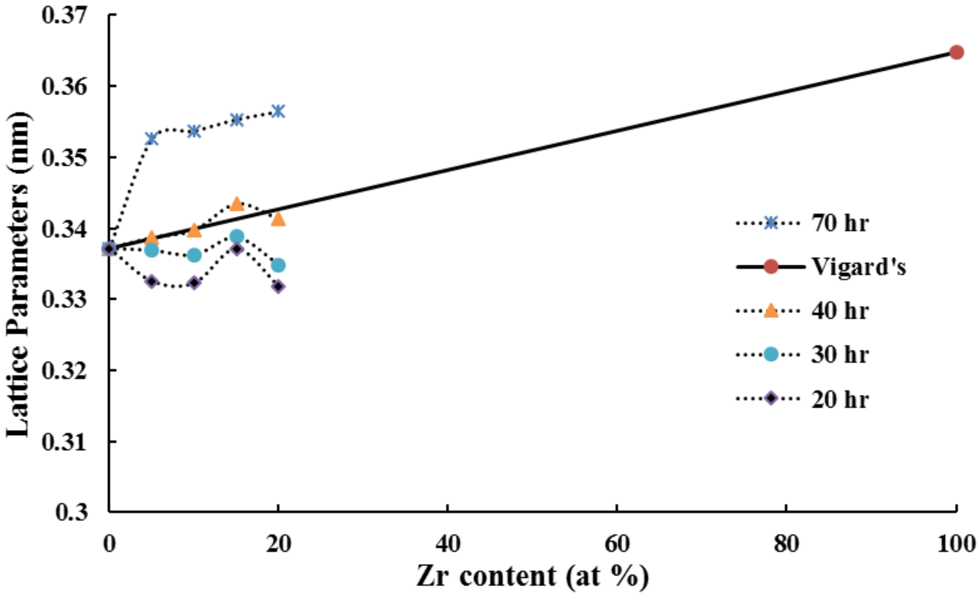

Figure 24 Variation of lattice parameter of Nb solid solution phase as a function of the milled powder blends MA for different times at BPR 10:1.

A number of different criteria have been proposed to explain the occurrence of amorphous phases in alloy systems. Of all these, the most important criterion appears to be that the constituent elements should have a reasonable size difference, i.e. atomic radius and lattice parameters. Egami and Waseda [125] had shown that when alloying occurs, introduction of solute atoms into the lattice of the solvent cause accumulation of strain and that this strain increases with the increasing solute content. When this strain reaches a critical value, the crystalline lattice becomes unstable and formation of an amorphous phase takes place. The minimum solute content required for the amorphous phase formation could be calculated from the relation:

$$\left[\left(\frac{r_B}{r_A}\right)^3 - 1\right] \times C_B^{min} = 0.1 \quad [125] \qquad (4.1)$$

Where r_B and r_A represent the radius of the B (solute) and A (solvent) atoms and C_B^{min} is the minimum solute content required to form the amorphous phase. Substituting the appropriate values for r_A and r_B, the minimum solute content (Zr) required for the formation of the amorphous phase works out to be 37.4 at.%. Thus, it is not surprising that we have obtained the amorphous phase in the Nb-Zr system in the composition range of 40 to 50 at.% Zr. But, it is interesting to show in this work the possibility of adjusting the severity of milling conditions to be able to realize the formation of the amorphous phase at lower Zr contents. Even though several other criteria have been proposed to explain the amorphous phase formation in rapidly solidified and mechanically alloyed conditions [127], these do not appear to be applicable to the Nb-Zr system because they exhibit the positive heat of mixing.

4.2.7 Morphology and Microstructures of the Milled Powders

Figure 25 and Figure 26 show SEM micrographs of $Nb_{95}Zr_5$ powders after selected times of milling at a BPR of 10:1 and 30:1, respectively. For the powders milled at a BPR of 10:1, coarse powders were gradually refined with milling time until 50 h, while at 70 h agglomeration started to occur which may be due to the domination of repeated cold welding over fracturing of the powder particles. This is possible because extremely fine particles, even though they are hard, behave in a ductile manner [126]. On the other hand, when powders with the same composition were milled at a BPR of 30:1 more irregular shape and agglomerations appeared as early as 5 h. However, as milling progressed to 10 and 20 h, a finer microstructure was obtained. This further highlights the fact that BPR has a significant effect on the morphology of the powder particles and also possibly on the structure of the phases formed.

As for the effect of milling on homogenizing the resulting alloys, Figure 27shows the compositional mapping of $Nb_{95}Zr_5$ at 5 h of milling. A homogenous solid solution Nb(Zr) was observed, which is confirmed by the uniform distribution of the two constituent elements throughout the powders.

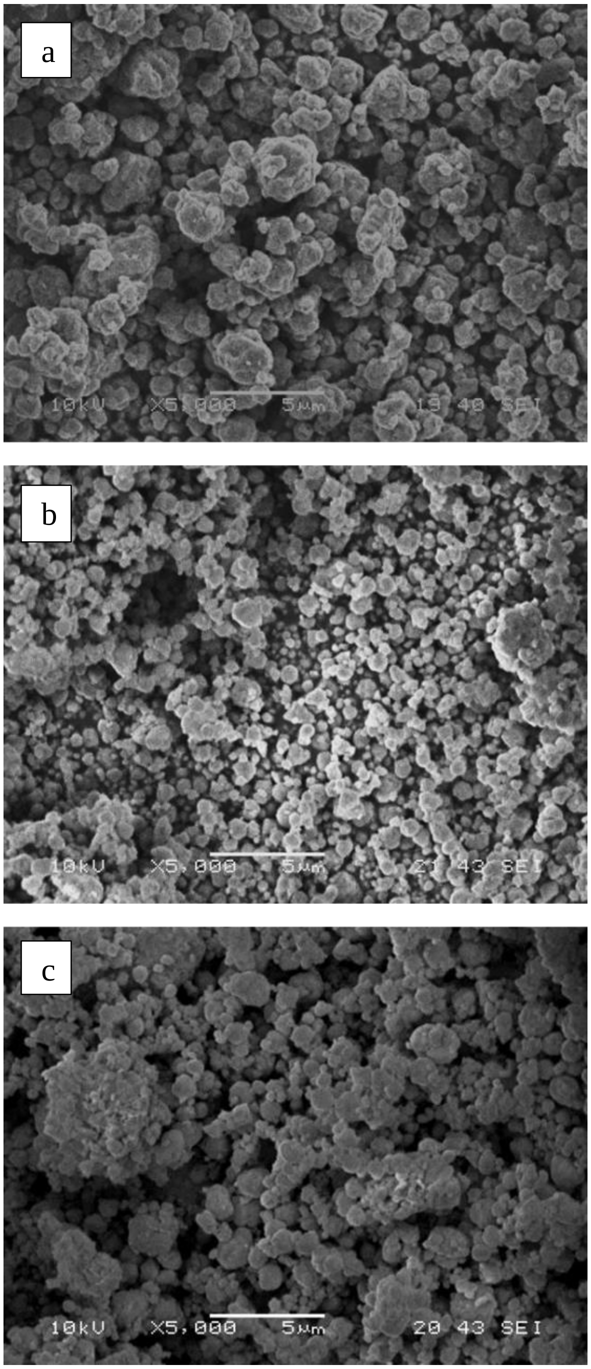

Figure 25 SEM images of Nb95Zr5, BPR 10:1 MA for (a) 10 h, (b) 50 h, and (c) 70 h.

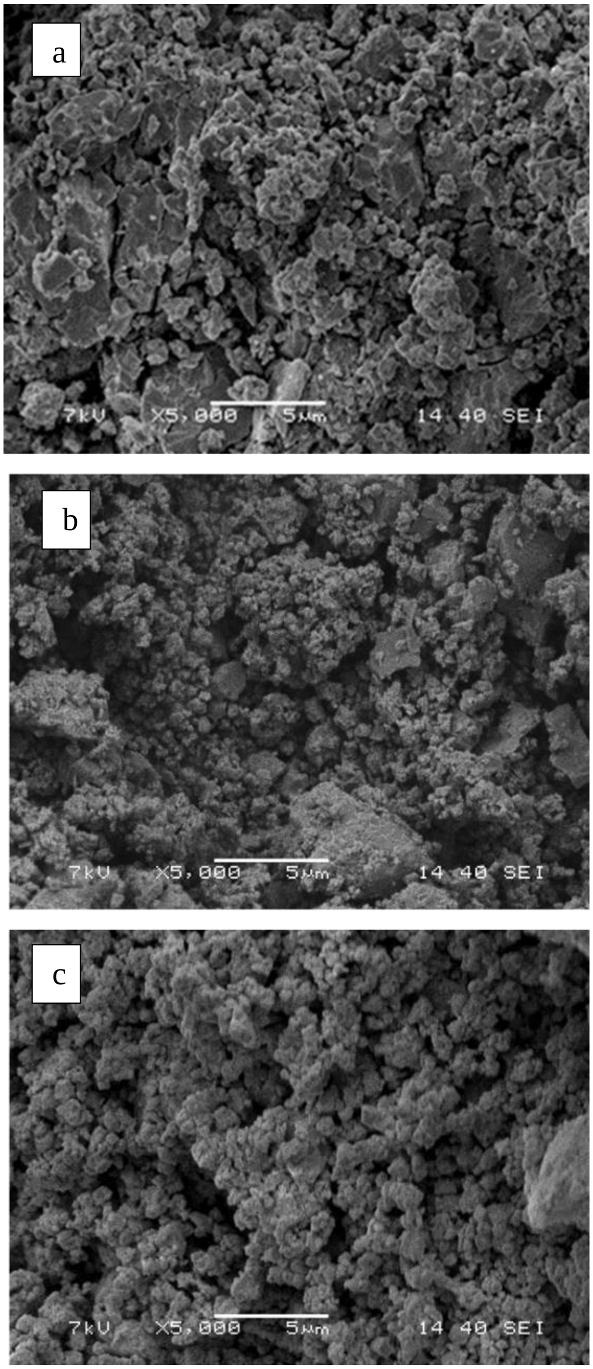

Figure 26 SEM images of Nb95Zr5, BPR 30:1 MA for (a) 5 h, (b) 10 h, and (c) 20 h.

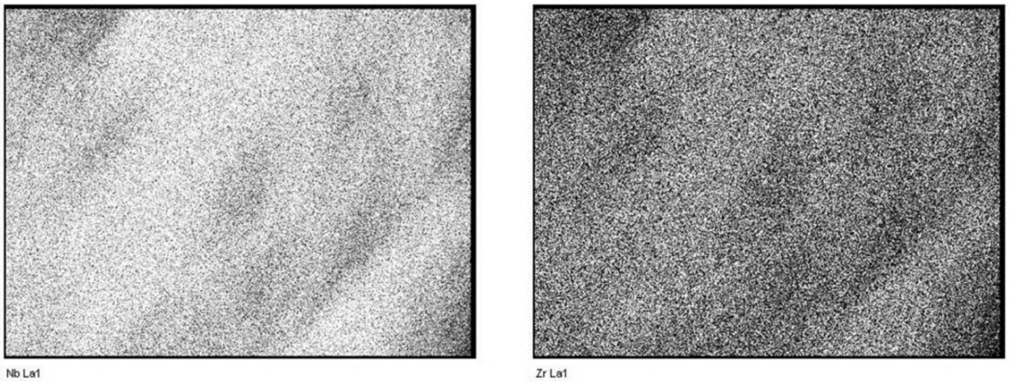

Figure 27 the compositional mapping of $Nb_{95}Zr_5$ at 5 h of milling, and BPR 30:1

4.2.8 Synthesis of $Nb_{60}Zr_{40}$Alloy (3)

4.2.8.1 Preparation of $Nb_{60}Zr_{40}$Alloy by MA

MA has been used to synthesize $Nb_{60}Zr_{40}$ alloy from as received elemental Nb, and Zr powders. The details of XRD and TEM explained in the previous section and depicted in Figure 12, and Figure 15. And will be summarized in the following section.

Figure 28 presents the XRD patterns of the MA Nb–40 at. % Zr powder. The as-mixed powder shows the presence of Nb and Zr only and no other phase is present. On milling the powder, the intensities of the diffraction peaks of both the metals decreased and their widths increased due to a reduction in crystallite size and the introduction of lattice strain [7, 64]. However, on continued milling of the powder blend to about 10 h, the diffraction peaks were replaced by a broad diffuse halo, corresponding to the (110) peak of Nb, suggesting that an amorphous phase had partially formed. Typical SEM micrographs of milled $Nb_{60}Zr_{40}$ powders are shown in Figure 29 .

---

(3) **Submitted**: M.A. Hussein, C. Suryanarayana, A. Madhan Kumar, N. Al-Aqeeli, Effect of Sintering Parameters on Microstructure, Mechanical properties and Electrochemical Behavior of Nb-Zr Alloy for Biomedical Applications, submitted to journal of Materials & Design.

Compared to the as-received morphology, after milling, the average particle size was reduced and the shape of the powder particles looks spherical and more uniform. However, due to the excessive cold welding and agglomeration of smaller particles, some large agglomerates were observed.

DSC measurements have been done for Nb40Zr milled powder for 10 hr under Ar fluxing atmosphere (20 ml/min). The thermal cycles consist of heating at 10 K/min up to 1200°C and free cooling in order to determine structural changes in the materials. Figure 30 shows exothermic peaks between (400°C-700°C). The possible reason for an exothermic peak on DSC curves to be a considerable number of random boundaries were observed to transform to order boundaries by atomic relaxation and/or diffusion under the influence of heat, accompanied by the release of the excess energies [128]. An exothermic peak related to recrystallization and subsequent grain growth, can be seen from DSC curves, this process decreases the free energy of the system by decreasing the volume fraction of total grain boundaries and causes enthalpy release. The metastable phases often show exothermic peaks in the DSC due to it's possess higher energy than the equilibrium phases. May be there are another transformations occur at higher temperatures which over the limitation of the available DSC machine.

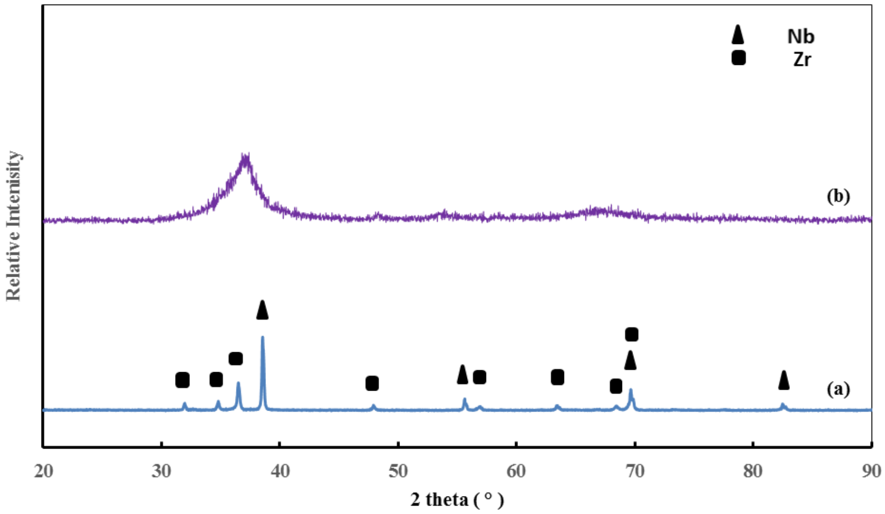

Figure 28 XRD patterns of Nb40Zr: a) as received mixture) milled powder for 10 hr

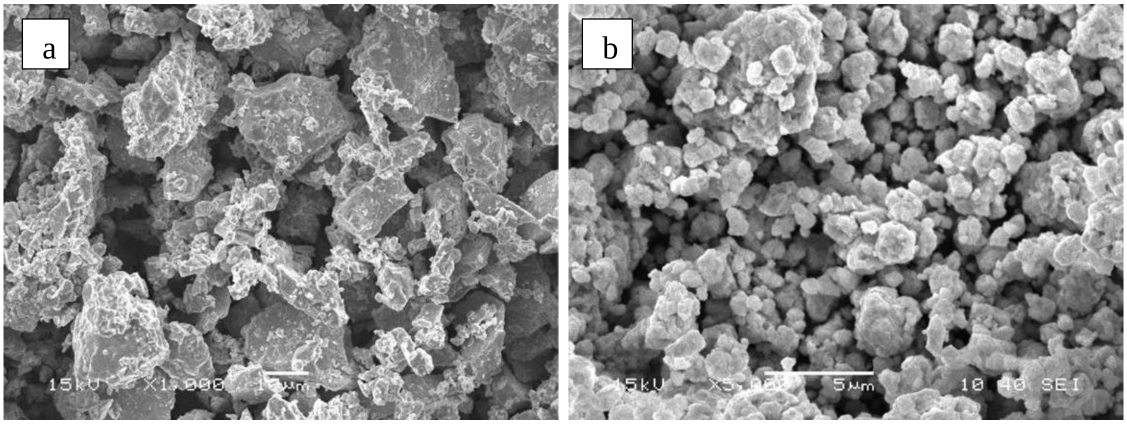

Figure 29 SEM micrographs of Nb40Zr:a) as received mixture) and b)milled powder for 10 hr

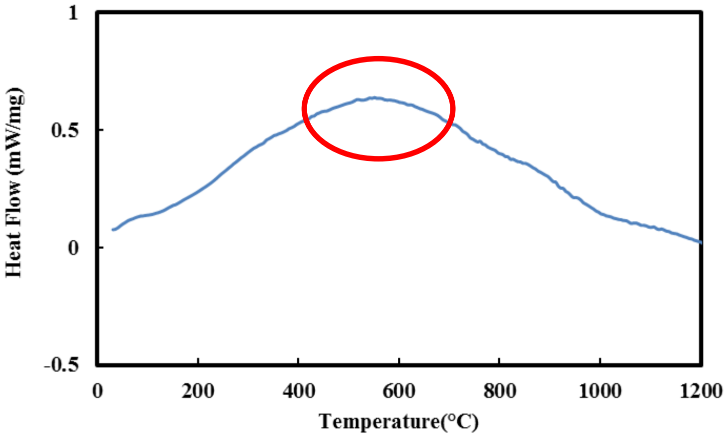

Figure 30 DSC results of Nb40Zr milled powder for 10 hr shows exothermic peak

4.2.9 Characterization of the SPS Samples

After conducting a detailed study of the phase evolution during the MA, the Nb–40 at. % Zr milled powder were consolidated using SPS process at different parameters. Table 4 summarizes the SPS conditions and its coding to be easy to refer to it.

After SPS, the samples have been characterized to study the effect of SPS parameters on the obtained phases, microstructure, densification, and mechanical properties. The phases of SPS samples were studied using XRD, and TEM. SEM was used to characterize the microstructures. The microstructures were also observed on TEM. Nanoindentation, and hardness tester (Buehler, USA) were used to measure the mechanical properties of the consolidated samples after polishing. The density determination kit was used to measure the density of sintered samples.

Table 4 parameters of SPS

Code	Temperature (°C)	Holding time (minutes)	Heating rate (°C /min)	Pressure (MPa)
S1	1300	10	100	50
S2	1300	15	100	50
S3	1300	25	100	50
S4	1400	10	100	50
S5	1500	10	100	50
S6	1300	10	50	50

4.2.9.1 Structure and Phase Analysis

XRD patterns for the sintered samples under a variety of sintering conditions are shown in Figure 31. Under all the as-sintered conditions, typical diffraction peaks of Nb, Nb(Zr)BCC solid solution ,and the Nb(Zr) FCC phase were observed. The formation of the FCC phase was achieved after prolonged milling (for approximately 70 h) of $Nb_{60}Zr_{40}$ powder and was attributed to the mechanical energy imparted by the milling process as there was no consolidation involved. However, after SPS, the observed formation of the FCC phase is attributed to the substantial heating applied during SPS within a very short period of time. This effect can be explained by the equivalence between the mechanical energy and heating of the alloy to high temperature, as reported previously [7]. This result of FCC metastable phase formation is in agreement with T L Wang et al and O.Jin,et.al [55,56] they obtained two metastable FCC phases in NbZr immiscible system by IBM.

Olivier et al [129] reported that SPS could be used in the sintering of non-equilibrium materials in their metastable state due to the exposure to high temperature and pressure in a short period of time. The resulting non-equilibrium phase combinations are primarily due to the high cooling rates associated with SPS [130]. For instance, non-equilibrium composites of cubic boron nitride-based composites were successfully obtained by SPS [131]. The similar observation was reported by [132], after SPS of CoCrFeNiMnAl MA alloy, the XRD showed the presence of both BCC and FCC phase together in the consolidated samples. The unexpected phenomenon may be associated with the critical conditions of the non-equilibrium process of rapid sintering in SPS, and the large pulsed electric current of SPS [132].

The XRD patterns clearly show that the increase in SPS temperature from 1300°C in Figure 31 f, does not yield a major transformation in the resultant phases. The only change observed is in the relative intensity of the peaks, which is triggered by the increase in temperature. The same argument also holds for the effect of increasing the holding time from 10 to 25 minutes, which led to a minute change in the relative intensities of the peaks.

Additionally, as shown in Figure 32, the Nb(110) peak is shifted towards a lower angle due to the dissolution of Zr atoms in the Nb matrix and the formation of a Nb(Zr)BCC solid solution. By increasing the sintering time and temperature and decreasing the heating rate, the peak shift becomes more pronounced, indicating the further dissolution of Zr in the Nb matrix and the formation of a Nb(Zr)BCC solid solution.

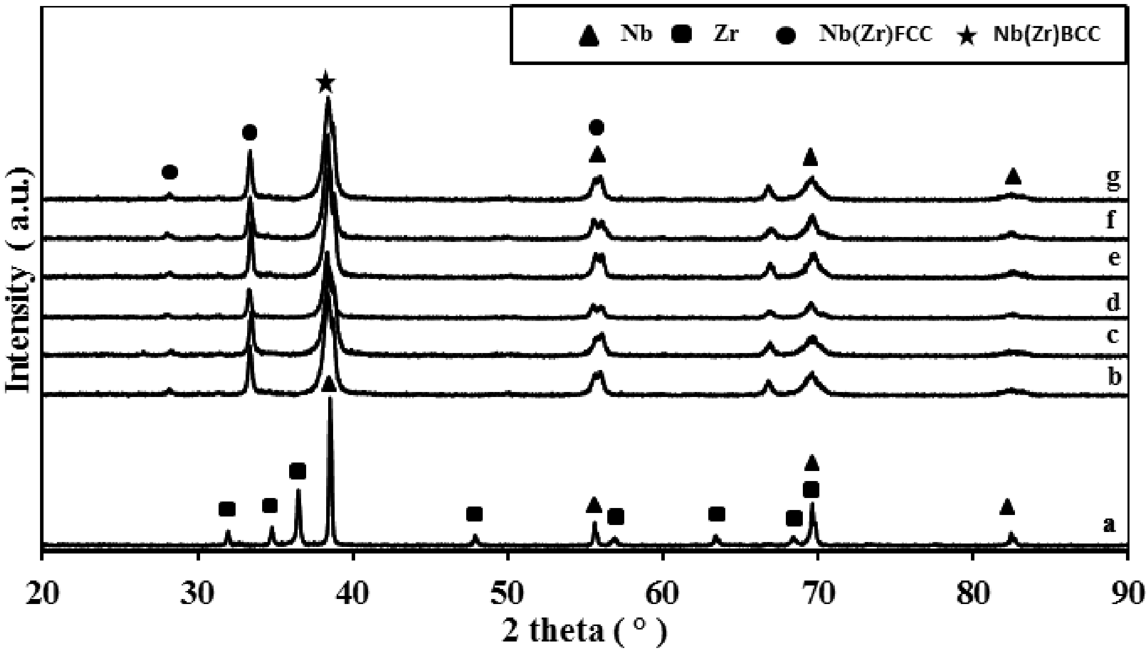

Figure 31 XRD patterns of Nb-Zr alloy under different conditions. a) As-received, (b-f) Milled for 10 hours, subjected to SPS post-milling under different conditions: (b) S1,(c) S2, (d) S3, (e) S4,(f) S5, and (h) S6.

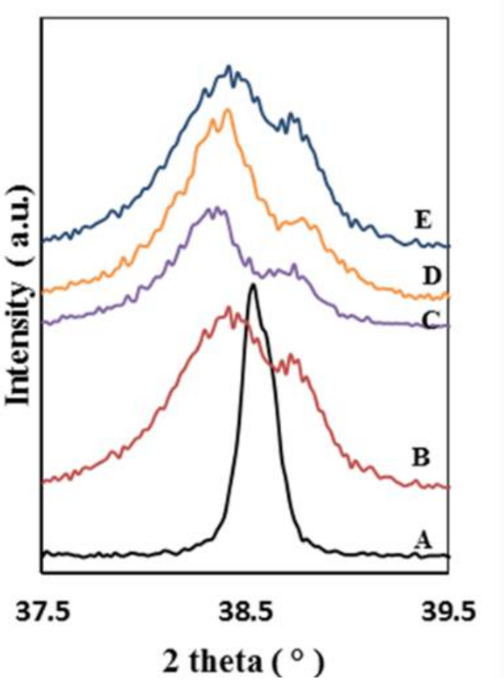

Figure 32 Shifting of the (110) Nb peak under different SPS conditions.

(A)As-received, (B) S1, (C) S3, (D) S5, and (E) S6.

4.2.9.2 Microstructure Analysis of Sintered Specimens

The phase morphology of the resultant alloys presented in Figure 33, and Figure 34. They show the SEM micrographs under both SE and BSEmodes for an SPS sample sintered at different conditions without etching. Two main phases with clear contrast (white and gray phases) were observed in all the sintered alloys. Based on the XRD and BSE results, it appears that the brighter region are pure Nb, Nb(Zr)BCC solid solution an d gray phase may be Nb(Zr), FCC phase . There exist a fair distribution between the alloy's constituents and there seem to be some micro-pores that are distributed into the structure. The presence of pores within the resultant microstructure could be of great value when these materials are used to produce implants because tissue is able to grow to fit these pores [133]. It's clear from the BSE image at different temperatures that the dissolution of Nb increases by increasing the SPS temperature from 1300 °C to 1500 °C.

High resolution FESEM (SE and BS) was performed without etching for selected samples shown in Figure 35 and Figure 36 at higher magnification to reveal the details of microstructure features: the BS-FESEM show the uniform distribution of the different phases: brighter regions are pure Nb, and Nb(Zr), BCC solid solution., the gray phase may be the FCC phase.

For more details about the feature of the microstructure, TEM studies were conducted and covered in the following section. It helps to study the nanostructure feature of the developed alloy which couldn't clearly be obtained by SEM.

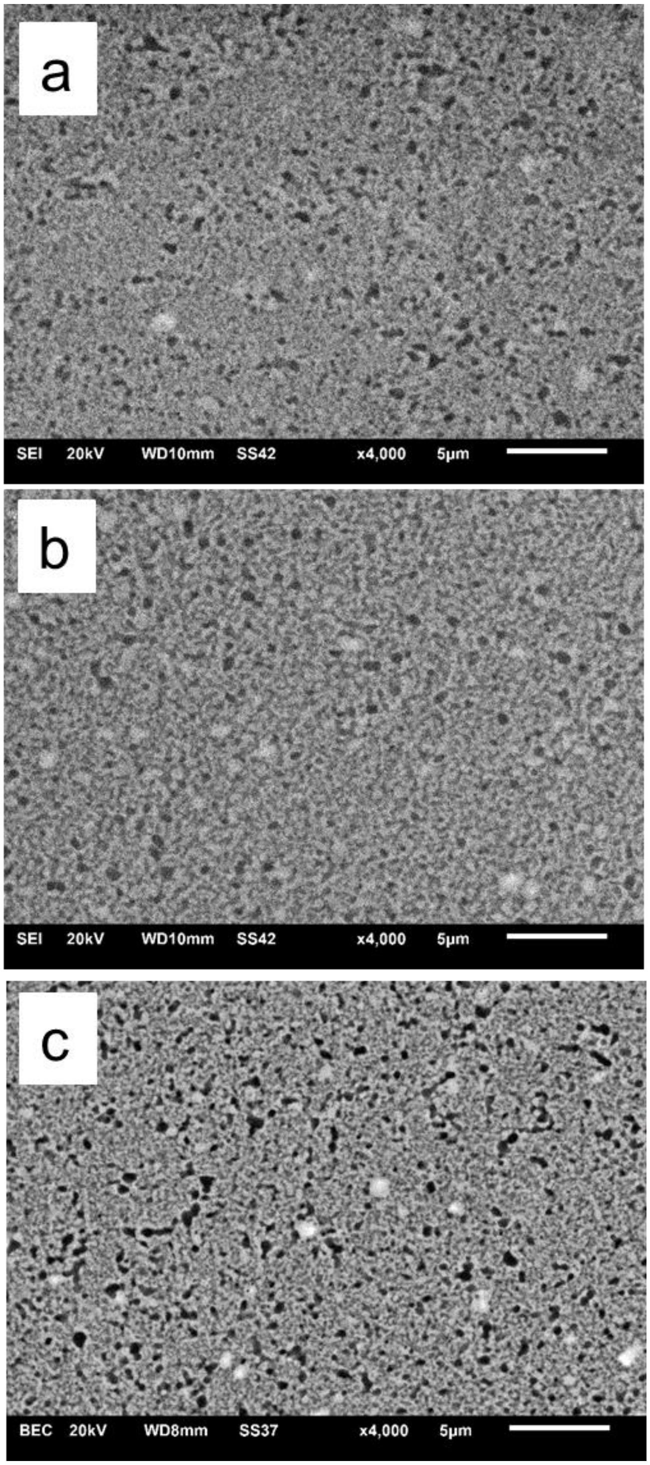

Figure 33 SE and BSE images of Nb-Zr alloy SPS at a) S1, (b) S4, and C) S5

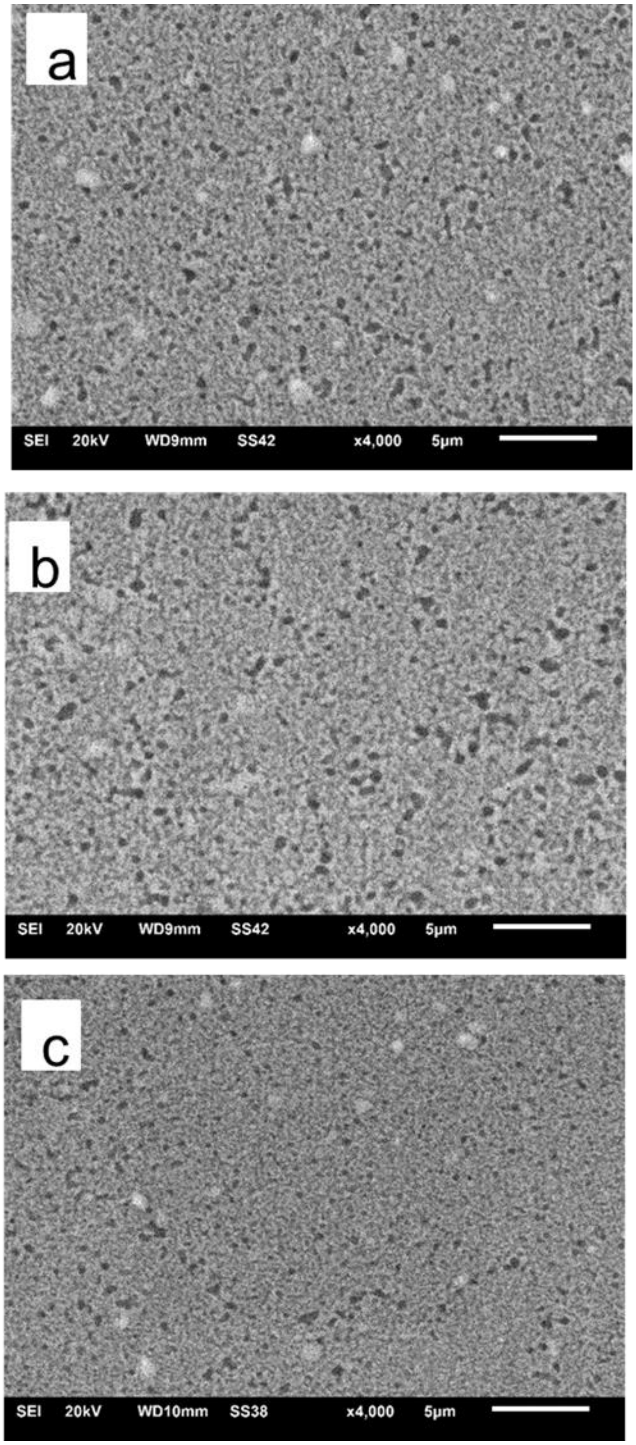

Figure 34 SE images of Nb-Zr alloy SPS at a) S2, (b) S3, and C) S6

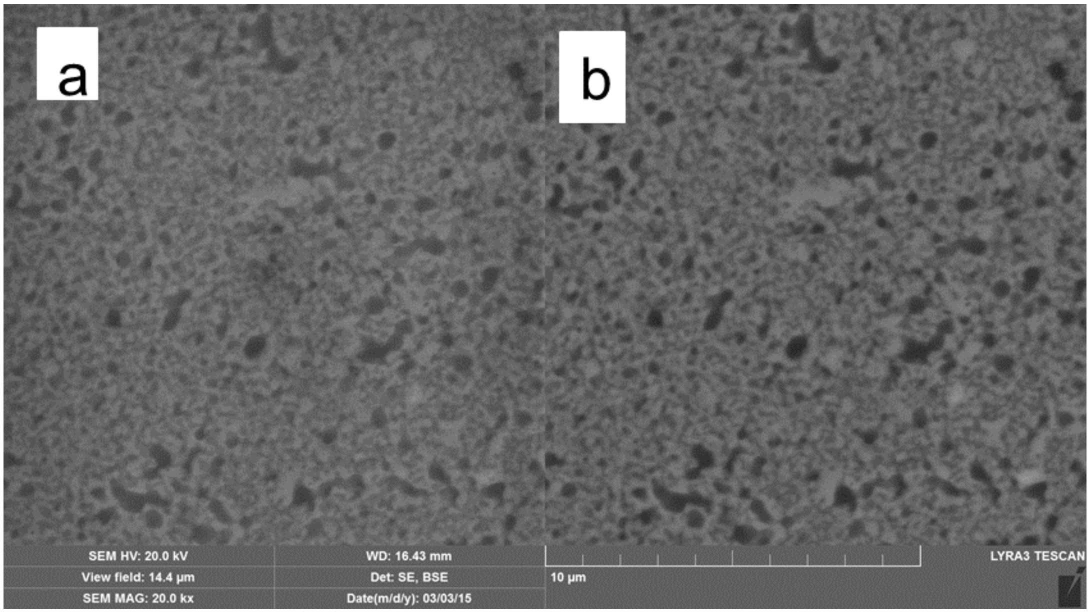

Figure 35 FESEM images: a) SE,b) BSE of Nb-Zr alloy SPS at h7

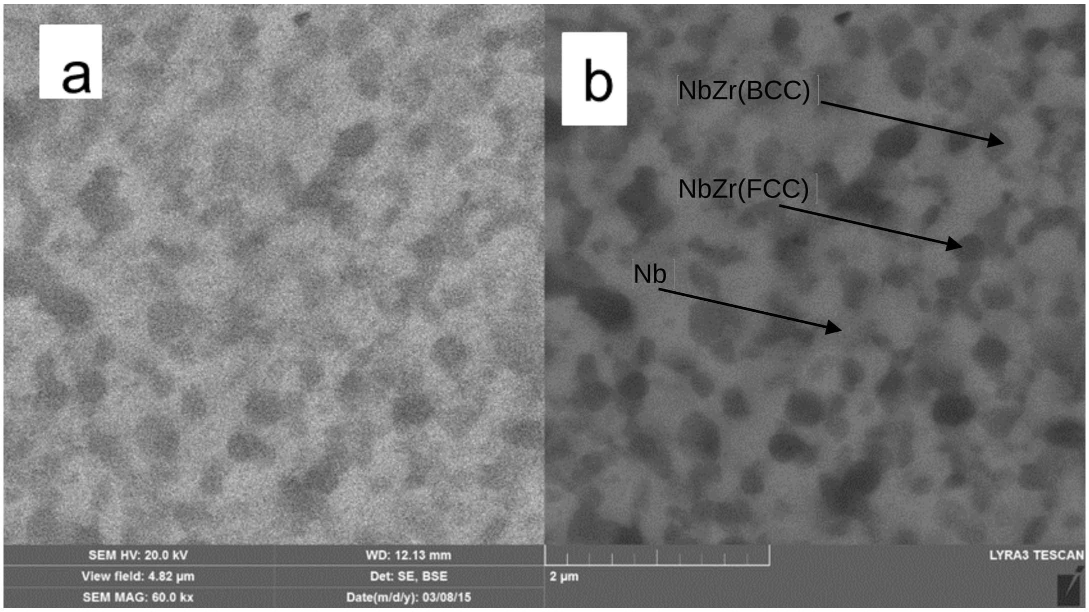

Figure 36 FESEM images: a) SE,b) BSE of Nb-Zr alloy SPS at h2

4.2.9.3 TEM Studies

Figure 37 shows the TEM results of the SPS sample at a temperature of 1300°C, holding time 10 minutes, and heating rate of 50°C min^{-1}. It is clear from these figures that the microstructure is not uniform and shows heterogeneous characteristics. According to the EDS analyses, the bright regions are pure Nb, and Nb-rich solid solution Nb(Zr), BCC (white contrast), and other regions, which contain alloyed Nb Zr, (FCC) (grey contrast). The figure also shows the presence of equiaxed grains having an average size of 100-300 nm, which highlights the benefits of using SPS in sintering these powders and the ability to retain the developed nanostructure. In fact the presence of the nanophase alloys was reported to be promising for the use as orthopedic implants due to enhancement of osteoblast adhesion on nano-grained metals compared to coarse-grained metals [10]. Nanograins have been reported also to improve cell-material interaction, which leads to enhanced cell attachment on the nanocrystalline alloy [9], in addition to better compatibility compared to the coarse-grained structure [134].

Additionally, Figure 37 b, shows the presence of stacking fault like defects in the crystal structure, which is attributed to the difference in crystal structures between the alloy's constituents, i.e. Zr is HCP while Nb is BCC. The high-resolution image in Figure 37 c shows Moiré fringes in which the superimposed grains are showing a slight difference in orientation. SAED in Figure 37 d shows ring patterns recorded from relatively small-sized grains (commonly referred to as powder patterns). These spotty rings are observed, as there are not enough grains to give a continuous ring pattern. This clearly suggests that grain sizes are small enough to get a single crystal spot diffraction pattern. The indexing of this pattern confirm the coexistence of BCC and FCC phase.

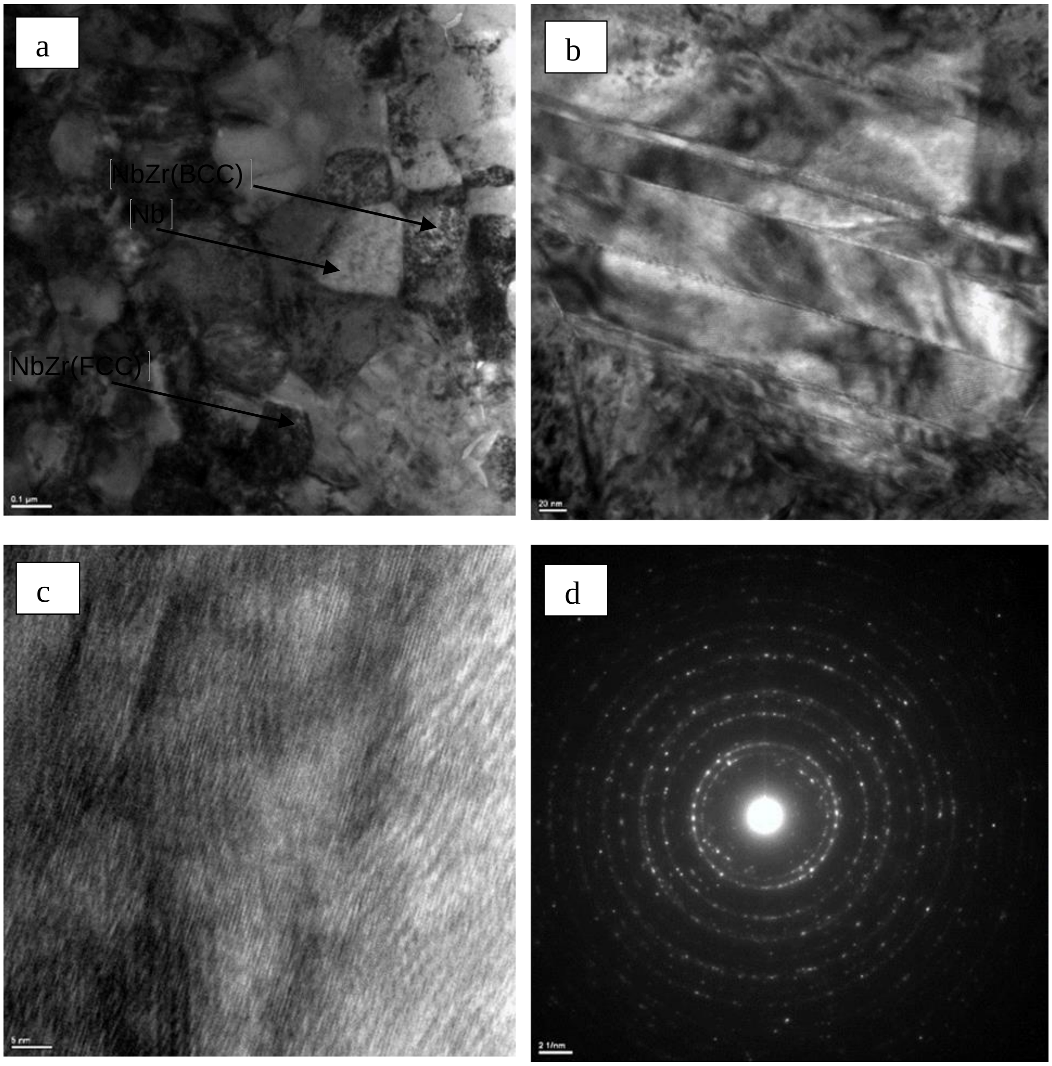

Figure 37 TEM results of the SPS sample at 1300°C, holding time 10minutes, and heating rate of 50 °C min-1: a) TEM image showing equiaxed grains, b) TEM micrograph showing stacking fault defects, c) the presence of Moiré fringes, and d) SAED Patterns

The consolidated samples were evaluated through density, and Vickers hardness measurements. Figure 38 shows the Vickers hardness and density measurements of the SPS Nb-Zr alloy as a function of the sintering holding time; for samples sintered at 1300°C at a heating rate of 100°C min^{-1}. It seems that hardness decreases with the increase in holding time, with a maximum hardness value of 564 H_V achieved at a 10-minutes holding time. This behavior is expected as the increase in holding time will lead to higher growth of the grains and ultimately lower hardness values. However, densification has increased upon increasing the holding time from 10 to 15 minutes, which can be related to the increased flux of heat that is associated with the increase in holding time. Nevertheless, as the holding time is increasing from 15 to 25 minutes the densification is slightly dropping. As the readings are given with error bars it can be concluded that the densification didn't change as the holding time was increased from 15 to 25 minutes. Both readings seem to be within the errors limitations and, thus, no change in densification can be concluded. It appears that increasing the holding time beyond 15 minutes is not needed as not much densification is achieved and the hardness seem to be decreasing as a result of having higher holding times.

To explore the effect of SPS temperature on the density and hardness of the SPS prepared alloys, we measured the hardness and density of three samples sintered at a heating rate of 100 °C min^{-1} for a holding time of 10 minutes Figure 39. The trend exhibited by the measurements indicates that the densification is marginally increased when the SPS temperature is raised to 1500°C. However, if we consider the marginal errors in the densification measurements, it appears that temperature has no pronounced effect upon densification. In contrast, the increase in sintering temperature considerably increases hardness. This may be due to a decrease in the number of pores in the resultant sample during heating and the improved contact between the powder particles. The same trend of increasing the hardness with the SPS temperature was reported in literature for different materials; Al6061 and Al2124 alloys [135]

The increase in holding time from 10 to 15 min increases densification; which leads to an increase in grain size and results in a decrease in hardness [136]. According to Hall-Petch relationship, the yield strength is dependent on the grain size and for Vickers indentation, the yield strength (σys) related to hardness (Hv) as $Hv / \sigma ys \approx 3$. Therefore, any increase in grain size of SPS samples can result in a decrease in hardness [135]. In general, the increase in sintering temperature leads to reduction of pores and an increase in grain size, which has a positive effect to increase hardness. These two effects could explain the negligible effect of temperature on the hardness as shown in Figure 39.

To study the influence of the heating rate in densification and hardness, a sample sintered at 1300°C for a holding time of 10 minutes was subjected to two altered heating rates of 50 and 100°C/min Figure 40. Sintering at the lower heating rate (50°C min^{-1}) yields an alloy with a larger densification (97.9%) and hardness (568 H_v). It appears that changing the sintering heating rate has a more pronounced effect on hardness than on density.

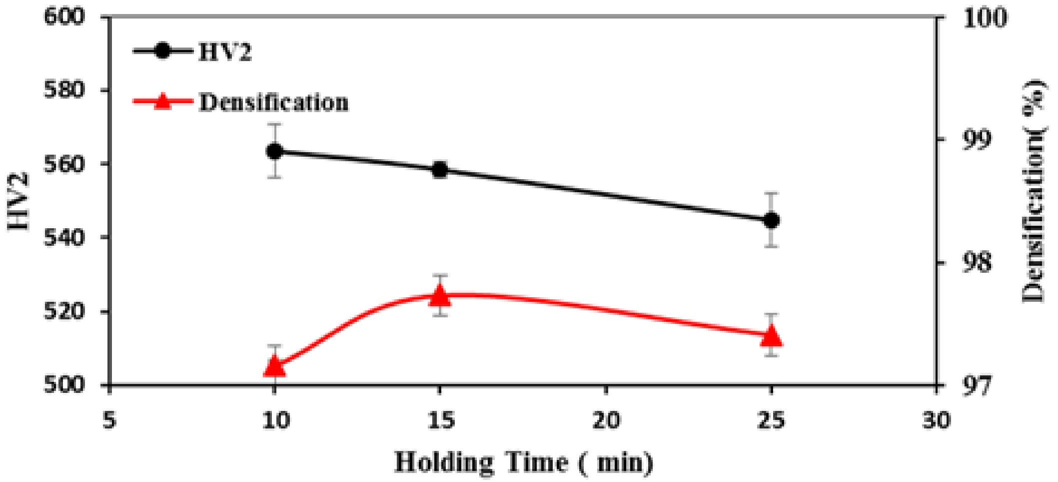

Figure 38 Hardness and densification versus holding time of the specimens SPS at 1300°C for 100°C min-

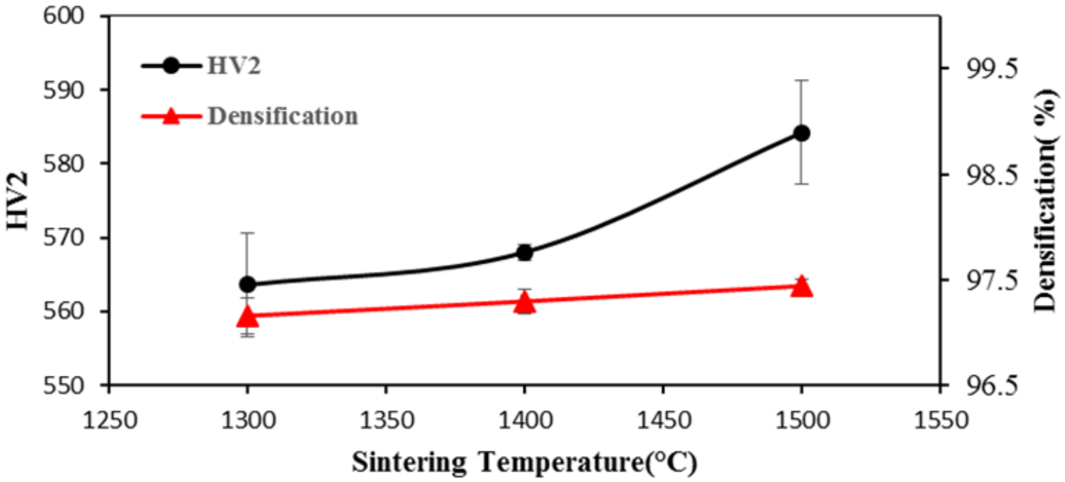

Figure 39 Hardness and densification as a function of SPS temperature; Sintering performed at 100°C min^{-1} for 10 minutes.

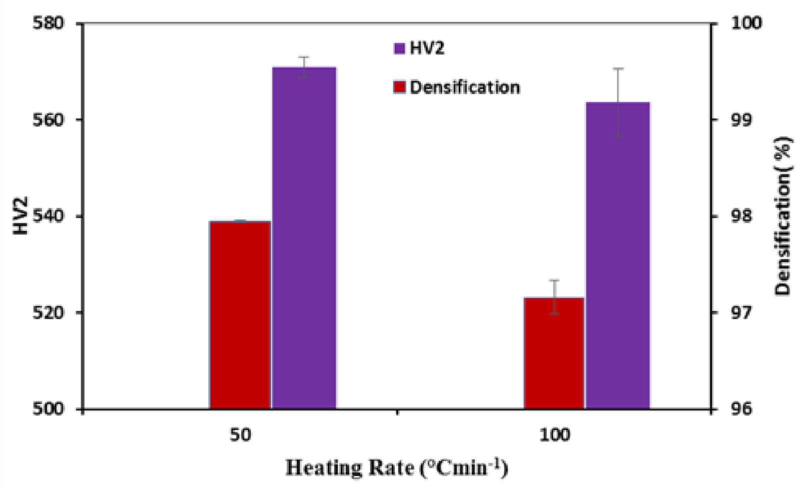

Figure 40 **Hardness and densification at different sintering heating rates for specimens sintered at 1300°C for 10 minutes**

4.2.9.4 Nanoindentation

Figure 41 shows the load displacement curve (P–h) nanoindentation curves for Nb40Zr alloy SPS at S5 conditions. The nanoindentation has been done at maximum load of 100 mN and loading and unloading rates of 100 mN/min and holding time of 5 sec. The values of hardness, Young's modulus and the extracted parameters related the resistance of the material to wear and implant lifetime are summarized in Table 5. The Nb40Zr alloy is harder than The Ti–6Al–4V alloy due to the nanostructured phases which possess higher mechanical properties compared to coarse structure. Moreover, Table 5 compares the ratios of H/E_r and H^3/E_r^2, these parameters were reported to be related to the implant lifetime and wear resistance [137]. The developed Nb40Zr alloy possess higher value for H/E_r, H^3/E_r^2 parameters compared to Ti–6Al–4VAlloy which indicate that the developed nanostructured Nb40Zr alloy possess higher wear resistance and longer lifetime.

The microhardness value for Nb40Zr alloy SPS at S5 (HV2=5.72 GPa) and S6 (HV2=5.6 GPa) at different from (H=13.09 GPa) and (H=10.51GPa) respectively, measured at 100 mN from NI, this due to ISE (indentation size effect) [138].which was reported to be due to several factors such as: surface effect [139], the friction between sample and indenter [140], or the gradient in the strain hardening [141,142]. In addition to, the developed Nb40Zr alloy possess lower Young modulus compared to CoCr (Cast) (240 GPa) and AISI 316L alloys (210 GPa) [18,143].

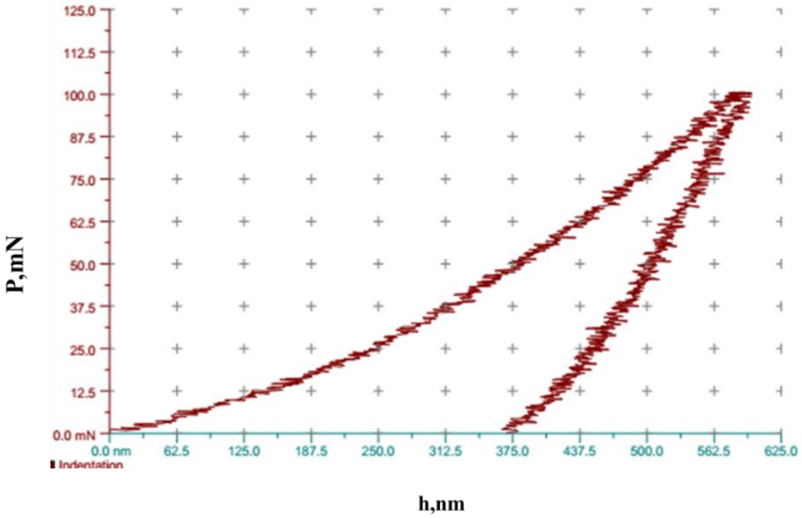

Figure 41 (P–h) nanoindentation curves for Nb40Zr alloy SPS at S5

Table 5 Summary of developed Nb40Zr properties (in italics) extracted from the nanoindentation curves in comparison with Ti–6Al–4V

Sample	H(GPa)	E_r(GPa)	H/E_r	H^3/E_r^2(GPa)	Test load, mN
Nb40Zr alloy SPS at S5 condition	13.09	212.1	0.0647	0.0549	100
Nb40Zr alloy SPS at S6 condition	10.51	207.8	0.05	0.0274	100
Ti–6Al–4V [137]	5.0	121	0.041	0.009	250

4.3 Ternary TiNbZr System

MA has been used to synthesize a Ti–20Nb–13Zr alloy from as received elemental Ti,Nb, and Zr powders, and then SPS has been used to consolidate the MA alloy powders at different temperatures. XRD, FE-SEM/EDX, TEM, and DSC has been used to characterize the synthesized alloy. After SPS, XRD, FE-SEM/EDX, TEM, densimeter, HV, and nanoindentation to study the influence of SPS temperature on the obtained phases, microstructure, densification, and mechanical properties.

4.3.1 Synthesis of Ti–20Nb–13Zr Alloy by MA

Figure 42 shows XRD patterns of as received powders and Ti–20Nb–13Zr after MA for 10 hours. All the expected peaks for as received powders are present. However, after 10 hours milling, the diffraction intensity of the peaks decreased and peak width increased due to accumulation of mechanical strain and reduction in the crystallite size [144]. The XRD pattern after10 hours milling shows a mixture of β-Ti phase, and a partial amorphous phase as evidenced by the diffraction peaks replaced by a broad diffuse halo at (110) peak of Nb and another peak at (211) peak of Nb. The dissolution of Nb and Zr into Ti and formation of partial amorphous phase may be due to evolving of crystal defects during mechanical alloying. The formation of partially amorphous phase was also reported in the same MA conditions in Nb-Zr binary system.

To confirm the results obtained from XRD, a TEM study has been conducted. Figure 43 shows TEM micrographs: BF image and SADP of the Ti20Nb13Zr powders milled for 10 hr. Some regions in the powder milled for10 h clearly showed the presence of an amorphous phase. This is confirmed from the high-resolution TEM micrograph that shows the salt-and-pepper like contrast (Figure 43a) and the presence of a broad diffuse halo in the diffraction pattern (Figure 43b). The existence of sharp diffraction rings is indicative of the presence of a crystalline phase (Figure 43c).This suggests the co-existence of amorphous and crystalline phases in the Ti20Nb13Zr powders milled for 10 h and confirms the XRD observations.

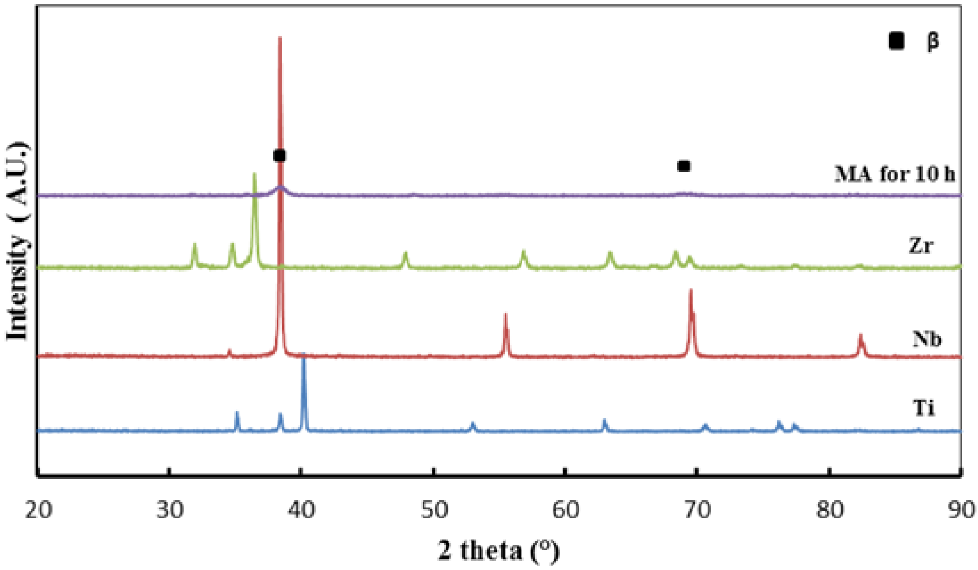

Figure 42 XRD patterns of as received powders and MA Ti20Nb13Zr for 10 hr

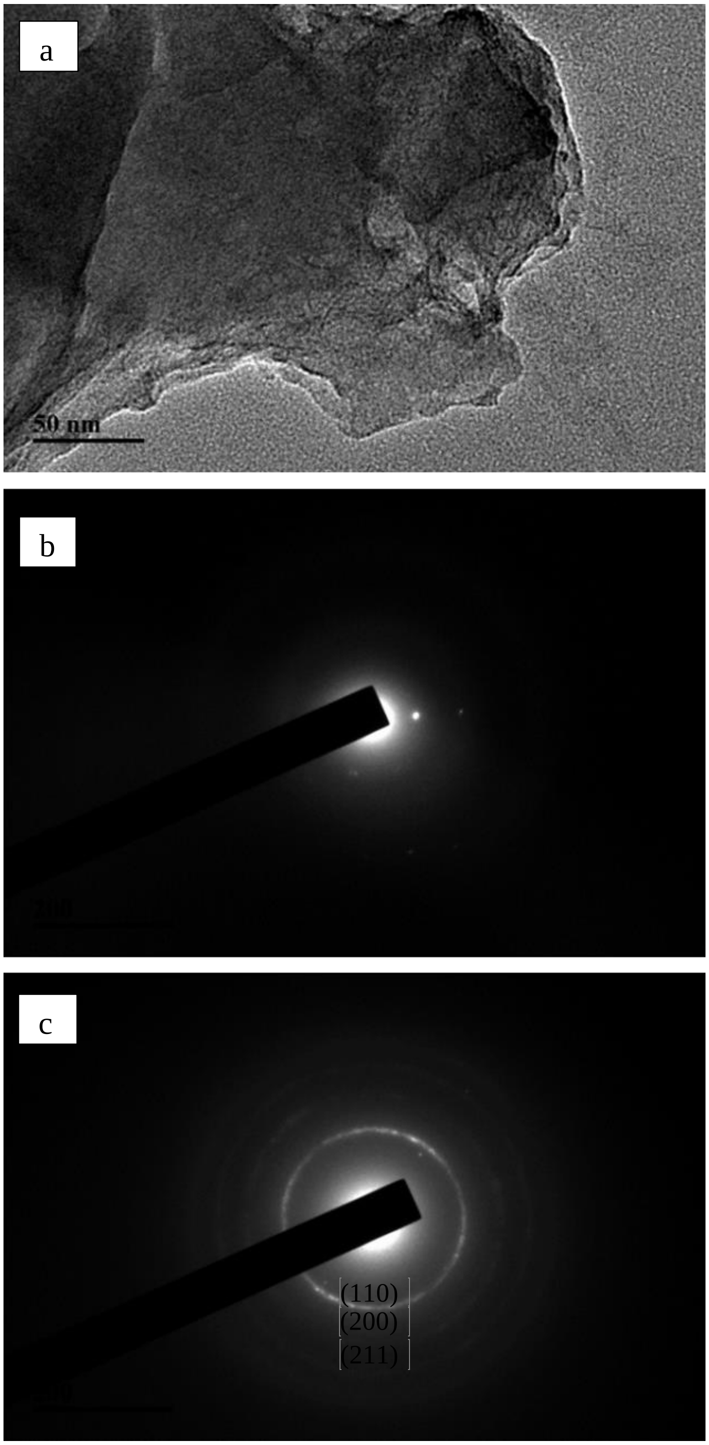

Figure 43 TEM: BF and SADP of Ti20Nb13Zr powders milled for 10 hr. The micrograph (a) shows the presence of the amorphous phase, confirmed by the diffraction pattern showing a halo (b) the micrograph (a) shows the presence of the BCC crystalline phase, confirmed from the diffraction pattern (c)

Figure 44 shows the morphology of Ti20Nb13Zr mixture before and after MA. It can be seen that the raw powder mixture before MA has different shapes of irregular and elongated with the average particle size of 23 µm for Ti and Nb and 31 µm for Zr. The morphology of Ti20Nb13Zr powders after MA is shown Figure 44b. Compared to as received morphology, the average particle size reduced and the shape of powders particles was spherical and more uniform compared to the irregular shape existed in as received powders. Some large particles were appeared due to the agglomeration of small particles and excessive cold welding.

In addition an elemental mapping were done to reveal the distribution of element of the MA powders. Figure 45 shows the homogenous distribution of Ti,Nb, and Zr in the whole area, confirming an effective MA of elemental powders at 10 hr of milling. The MA has been stopped at this time as the target phase and homogenous distribution of the alloying elements has been obtained to avoid the contamination from balls and vials.

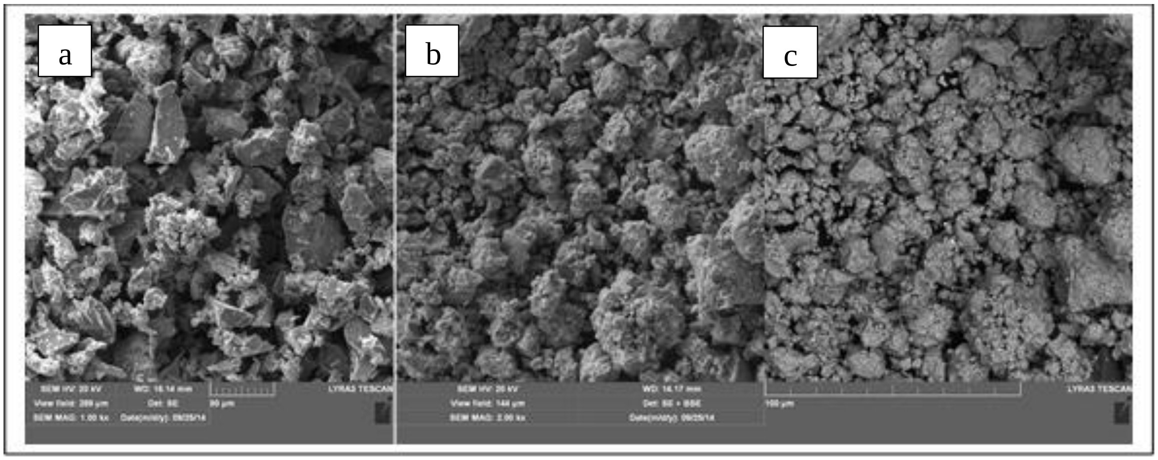

Figure 44 SEM micrographs of (a) as received powders (b) SE of MA Ti20Nb13Zr for 10 hr

(c) BS of MA Ti20Nb13Zr for 10 hr

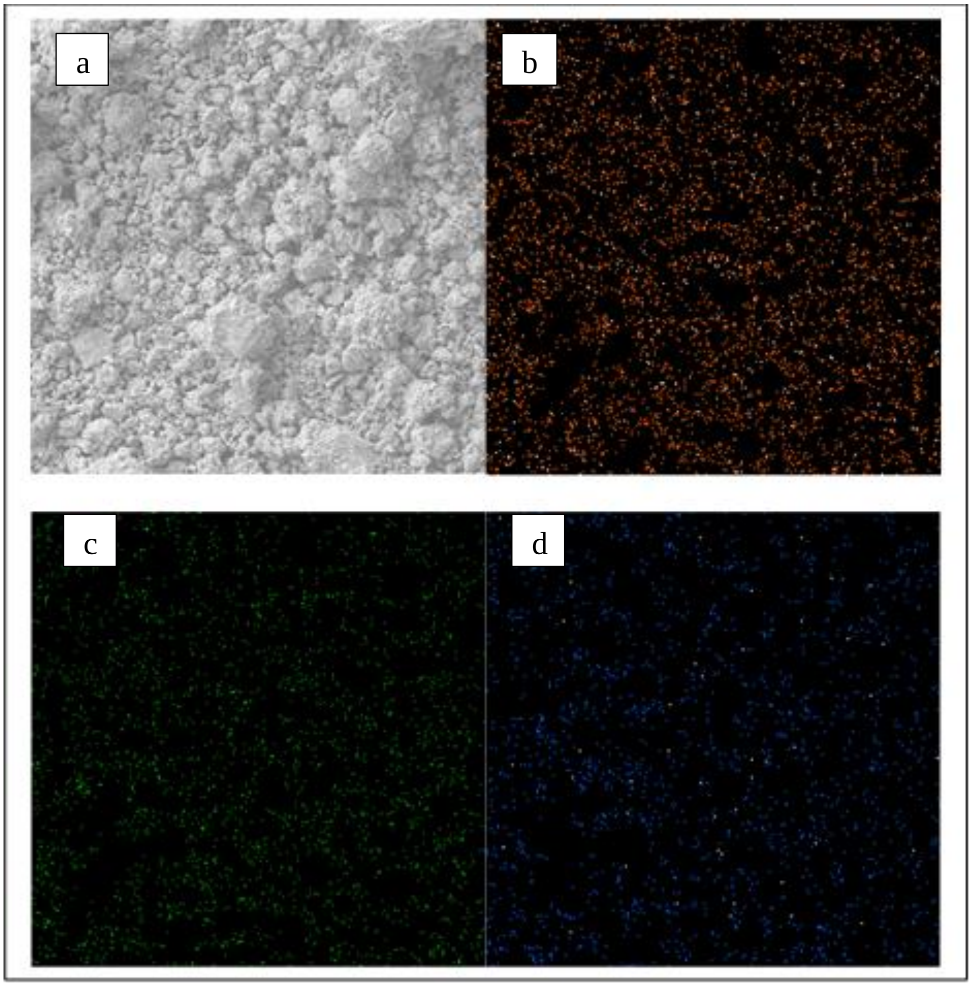

Figure 45 EDX mapping of the element distribution of MA Ti20Nb13Zr for 10 hr : (a) scanned area , (b) Ti, (c)Nb, (d)Zr

DSC measurements have been done for Ti20Nb13Zr milled powder for 10 hr under Ar fluxing atmosphere (20 ml/min). The thermal cycles consist of heating at 10 K/min up to 1200°C and free cooling, in order to determine structure changes in the materials during the process. As a comparison, pure Ti sample was also analyzed at the same condition. Figure 46 shows exothermic peaks between (450°C-1000°C). the possible reason for an exothermic peak on DSC curves, It is considered to be the release of energy of lattice defects and grain boundaries of high density, Also, a considerable number of random boundaries were observed to transform to order boundaries by atomic relaxation and/or diffusion under the influence of heat, accompanied by release of the excess energies [128]. This process decreases the free energy of the system by decreasing the volume fraction of total grain boundaries and causes enthalpy release. The metastable phases often show exothermic peaks in the DSC due to it's possess higher energy than the equilibrium phases. Figure 46 show the DSC curves. The analysis shows that that α to ß transformation starts with TNZ alloy at (636 °C) lower than that of pure Ti (964°C) this indicate that amount of α-phase in TNZ alloy is lower than of Ti._Moreover, another transformation could be seen at 1100C, which may be due to transformation of ἃ into β phase.

]

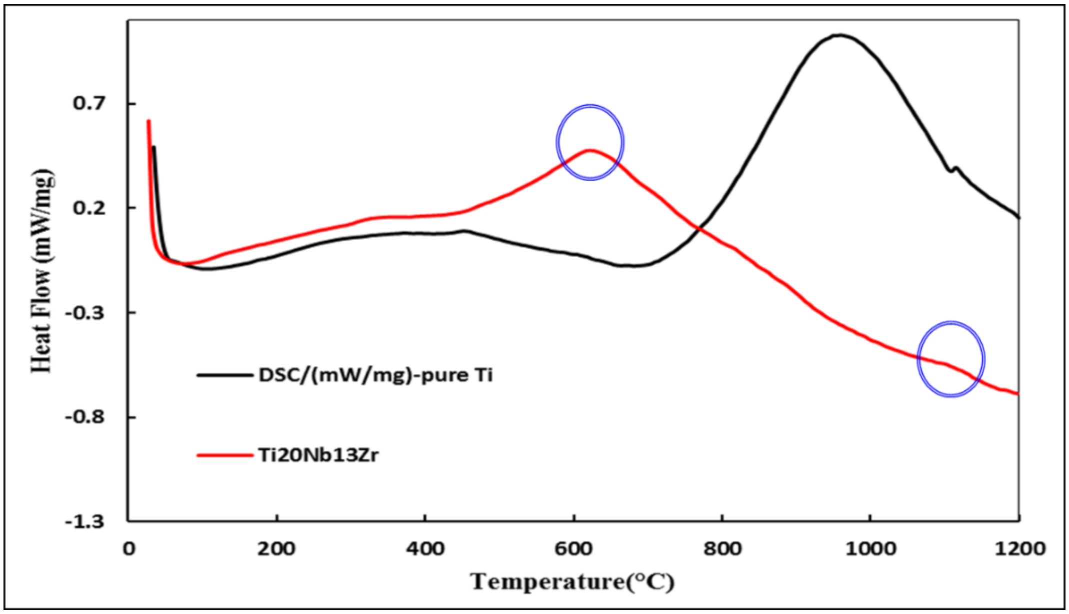

Figure 46 DSC results of Pure Ti, and Ti20Nb13Zr milled powder

4.3.2 Characterization of the SPS Samples

4.3.2.1 Structure and Phase Analysis

The phases of SPS samples were studied using XRD. Figure 47 shows XRD patterns of SPS Ti–20Nb–13Zr alloy at different sintering temperatures. The samples sintered at 800 °C, 900 °C, and 1000 °C revealed peaks form β, α, and ὰ. The peak intensity of β phase is higher than that of α phase indicating that the percentage of β phase is higher than that of the α phase. The intensity of the ὰ (martensitic metastable phase) peak is very low suggesting that it is present only in minor amounts, by increasing SPS temperature its amount decrease and more amount of equilibrium phases (β and α) are formed. These results matched with the results obtained from FE-SEM. The results from both BS-FESEM and XRD suggested that dissolution of Nb continued till 1000 °C. The increasing intensity of the β - phase peaks with increasing SPS temperature clearly confirmed that the amount of the β phase increased due to dissolution of Nb. Above a sintering temperature of 1000 °C, all the Nb has probably completely dissolved as inferred from the microstructural analysis.

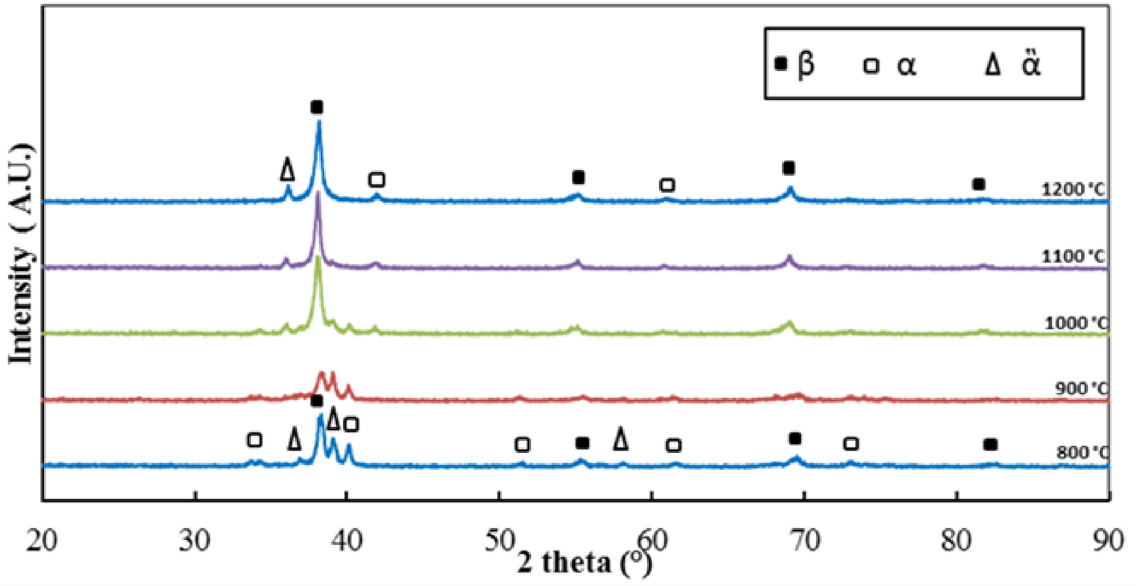

Figure 47 XRD patterns of SPS Ti–20Nb–13Zr alloy at different sintering temperatures. Note that the amount of the β-phase increased with increasing SPS temperature.

4.3.2.2 Microstructure Analysis of Sintered Specimens

Figure 49 and Figure 49 show FE-SEM and BS-FE-SEM images of Ti–20Nb–13Zr alloy after SPS at different temperatures. As obvious from the microstructure, the samples sintered at 800°C and 900 °C, Figure 49 (a, and b), the densification is incomplete. From the BS- FE-SEM, the brighter particles existed in the samples sintered at 800 °C to 1000 °C, are for Nb. These Nb particles are dissolute in both β and α regions with increasing sintering temperature, it seems that Nb particles completely dissolved in the samples sintered above 1000 °C which matched with the results obtained from [145]. The dissolution of Nb continues with increasing sintering temperature, which increases with increasing the volume fraction of both β and α phases [145]. At 1000 °C, the Nb still continued undissolved and the equiaxed microstructural of α uniformly distributed in β-matrix is clearly appearing. The microstructural features for the samples sintered in the range 1100-1200 °C is β-Ti (BCC) matrix which surround the α-Ti (hcp) region, the Nb completely dissolved and the alloy is chemically homogenized. It can be inferred from the BS- FE-SEM that the dark phase was α, and the bright phase was β.

The feature of the microstructure obtained by SPS is different from obtained by conventional sintering method. The microstructure of Ti13Nb13Zr sintered by conventional sintering shows a fine plate- like α phase plus β structure with α on grain boundary [140]. The equiaxed structure in Ti-based alloys was reported to possess a better combination of low modulus and higher strength compared to lamellar or acicular structure [146].

The EDX results from 6 different locations in the Ti-20Nb-13Zr (at.%) sample sintered at 1200 °C reveal that the average composition of the β phase was Ti-25.26%Nb-13.37%Zr (at.%). whereas the α phase contained Ti-18.53%Nb-13.84%Zr (a.%) . The EDX results clearly confirm that the higher Nb content in the β-phase (25.26 at.%) preferentially stabilizes this phase. Zr is reported to stabilize both the α and β phases in titanium alloys, and accordingly, the Zr content was almost the same (13.4 – 13.8 at.%) in both the α and β-phases. Figure 51 show an EDX elemental mapping of Ti–20Nb–13Zr after SPS, it reveal the homogenous distribution of Ti,Nb, and Zr in the whole alloy in the.

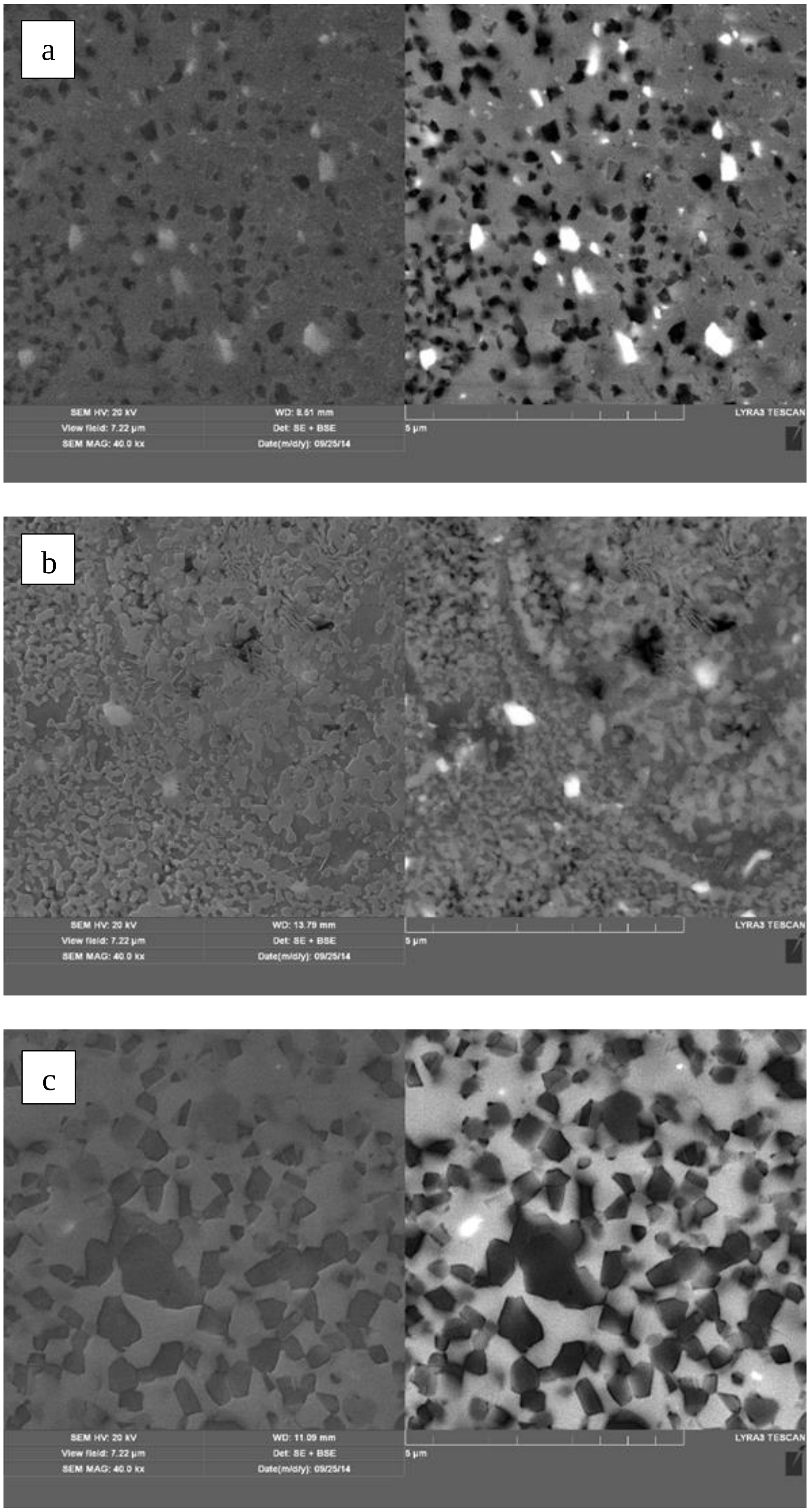

Figure 48 FE-SEM images of Ti–20Nb–13Zr alloy after SPS at: (a) 800°C; (b) 900°C; (c) 1000°C. The figure on the left hand side shows the back scattered image while the one on the right hand side shows the secondary electron image.

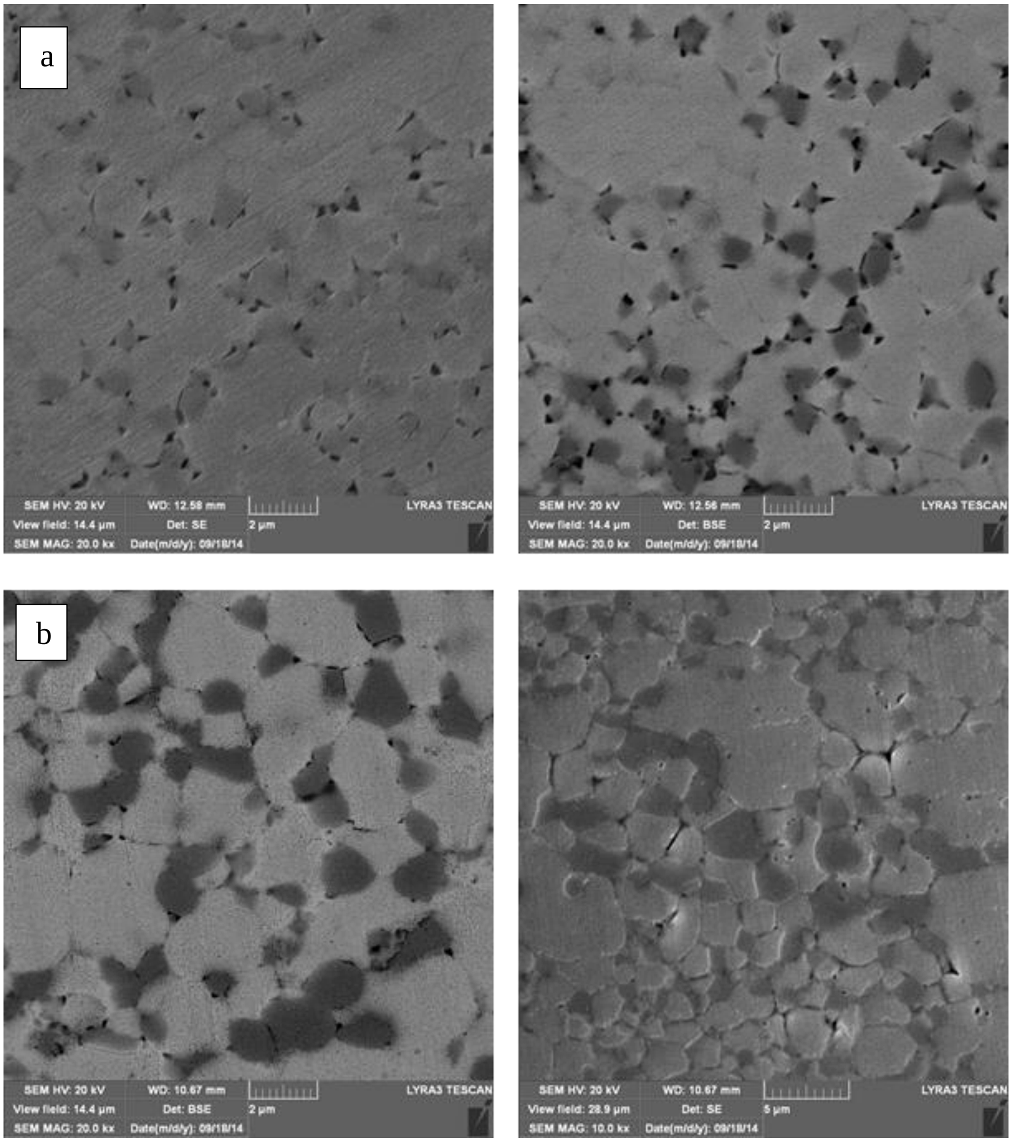

Figure 49 FE-SEM images of Ti–20Nb–13Zr alloy after SPS at: (a) 1100°C; (b) 1200°C. The figure on the left hand side shows the back scattered image while the one on the right hand side shows the secondary electron image.

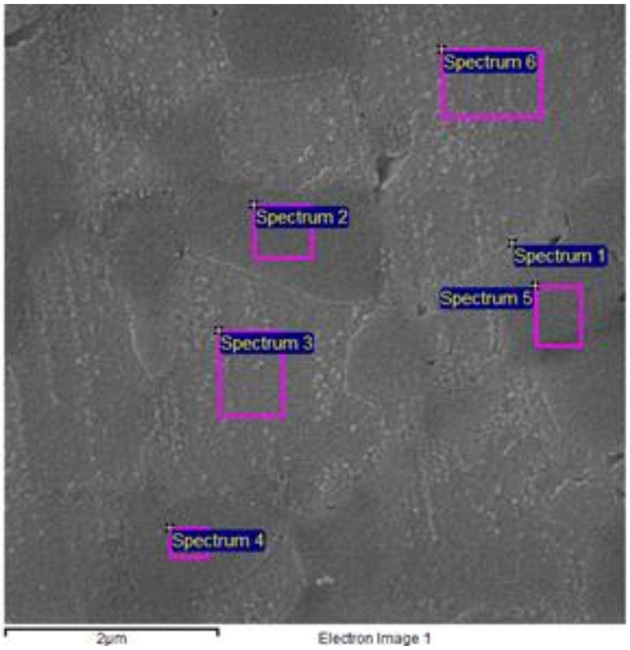

Figure 50 EDS of Ti–20Nb–13Zr alloy sintered at 1200 °C

Table 6 EDS of Ti–20Nb–13Zr alloy sintered at 1200 °C (in atomic %)

Spectrum	Ti	Zr	Nb
Spectrum 1	59.87	13.63	26.50
Spectrum 2	66.58	13.72	19.70
Spectrum 3	60.84	13.70	25.45
Spectrum 4	68.66	13.97	17.37
Spectrum 5	60.89	13.06	26.05
Spectrum 6	63.84	13.10	23.07
Mean	63.45	13.53	23.02
Std. deviation	3.56	0.37	3.75
Max.	68.66	13.97	26.50
Min.	59.87	13.06	17.37

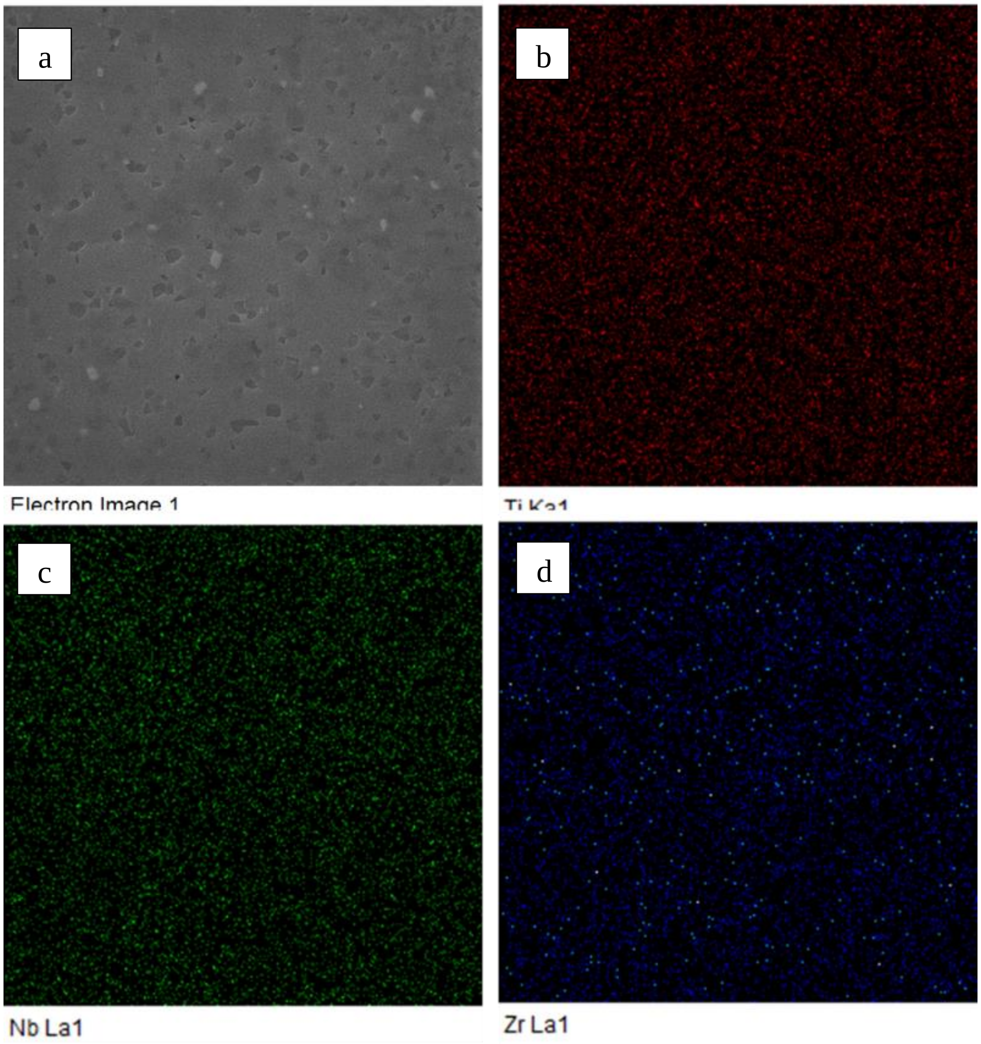

Figure 51 Mapping of of sample sintered at 1000 °C (a) scanned area, (b) Ti, (c) Nb, (d) Zr

To reveal the possibility of any effect of etchant on the obtained structure, SEM, and FE-SEM has been done for Ti–20Nb–13Zr alloy after SPS at 1200°C without etching shown in Figure 52 a, and b. The results show the same features of β-Ti (BCC) matrix which surround a α-Ti (hcp) region.

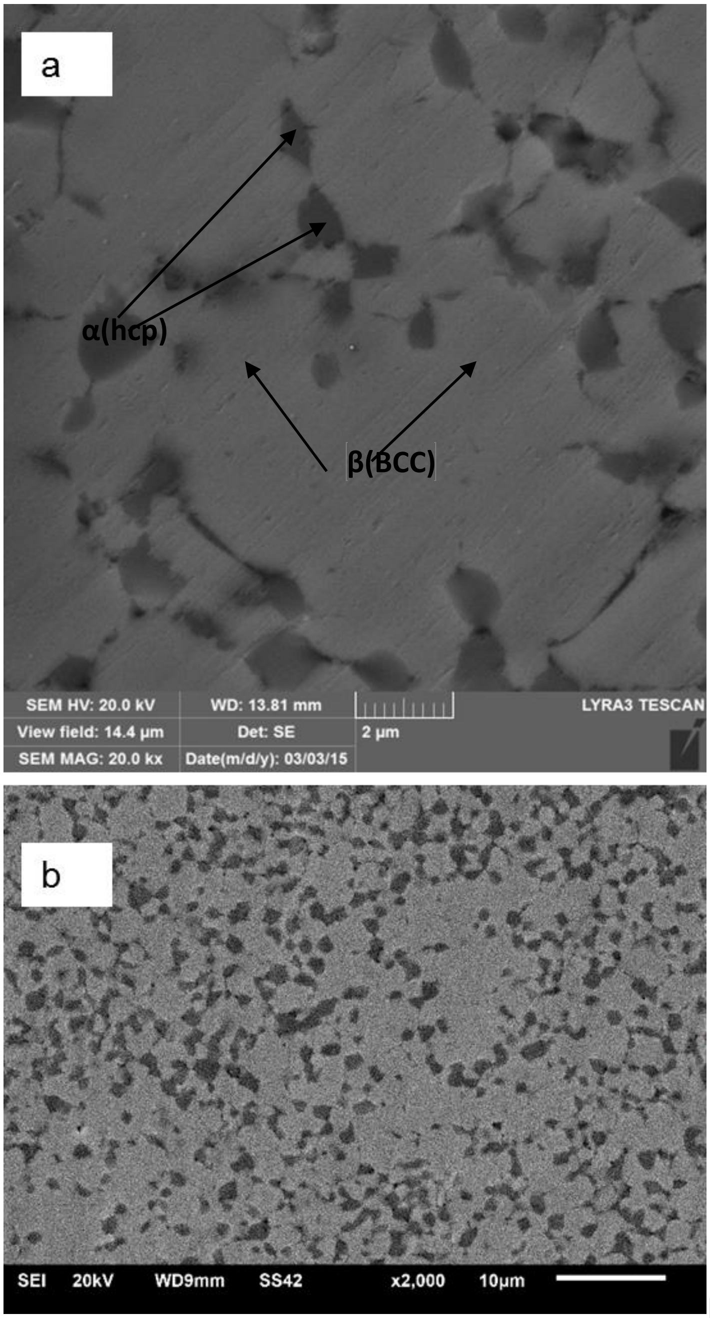

β

Figure 52 Micrograph of Ti–20Nb–13Zr alloy after SPS at 1200°C:a)FESEM, b)SEM the results show the β-Ti (BCC) matrix which surround a α-Ti (hcp) region

4.3.2.3 TEM Studies

Figure 53 shows the TEM BF image of Ti–20Nb–13Zr alloy sintered at 1200 °C. The structure is β Ti (BCC) matrix surrounding the (hcp) region. The average grain size of the dispersed α phase is between 70 and140 nm. It has been reported that nanophase materials do possess unique surfaces and exceptional mechanical properties similar to those of the human bones; hence they are considered to be the future generation orthopaedic biomaterials [9]. Nanocrystalline alloys possess higher surface energy and larger surface area than coarse grains to lead to enhancement interaction with cells which lead to enhance proliferation and cell attachment on the nanocrystalline alloy [9,18] Also, it was reported that the surface of metallic materials which possess low micron to nanophase topography enhanced and increased the adhesion of osteoblast [147]. Moreover the nanostructure alloy has better compatibility compared to coarse grain structure [134].

In the nano grained materials the number of atoms on the surface is very high and hence possess large surface energy. The Bioactive surface of nano grained materials promote greater amount of protein adsorptions stimulate new bone formation than conventional structure as shown in Figure 54. Moreover, the dimensional similarity to bone/cartilage tissue, nanomaterials also exhibit unique surface properties (such as surface topography, surface chemistry, surface wettability and surface energy)[148].These advantages of nanocrystalline alloy suggested the developed nanostructure Ti–20Nb–13Zr alloy for biomedical applications as in implant material in dental and orthopedic applications.

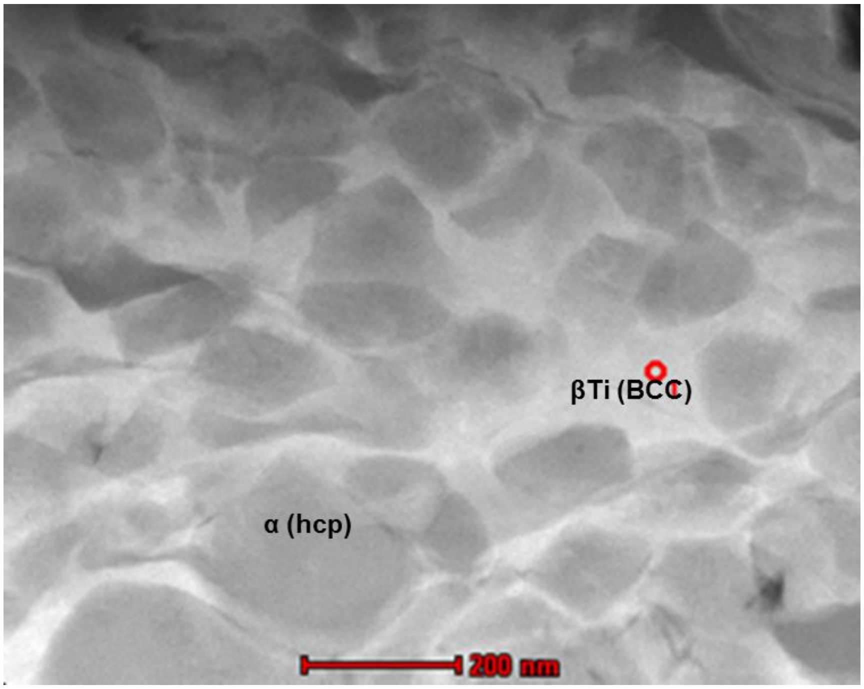

Figure 53 TEM bright field image of Ti–20Nb–13Zr alloy sintered at 1200 °C.

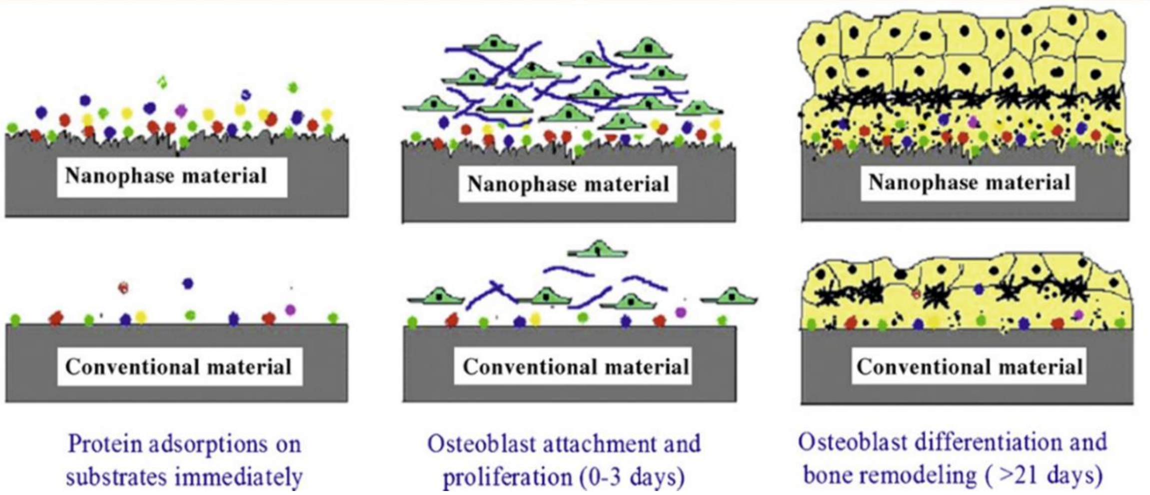

Figure 54 The biomimetic advantages of nanomaterials. [148]

4.3.2.4 Densification Studies

To study the influence of SPS temperature on the densification behavior of nanocrystalline Ti20Nb13Zr alloy, the samples were sintered at a heating rate of 100 °C /min and 10 minutes holding time while the SPS temperature was varied. It is clear from Figure 55 that the densification percentage increases with increasing of SPS temperature due to the decrement of the original pores existed in the specimen. The rate of pore elimination increased by increasing SPS temperature, which lead to increase in the densification. The samples show densification about 96.7 % of theoretical density at 800 °C which increased with sintering temperature till 99.5% at 1200 °C SPS temperature.

In comparison with literature, a Ti–35Nb– 7Zr–5Ta alloy was consolidated by conventional sintering and the full densification was obtained at the sintering temperature of 1700 °C [149]. Also, Ti–13Nb–13Zr alloy was developed by conventional sintering and the densification between 93 and 97%, was obtained after sintering at 1,400°C [145]. Compared to the results obtained by SPS, by using the spark plasma sintering, a near fully densification could be obtained at a lower temperature of titanium alloy. The reason of obtaining a good density in SPS at relatively lower temperatures due to ionisation of particle by local spark during spark plasma sintering, which causes melting of the titanium oxide films and formation of neck junctions between particles of powders at lower temperature [150]. In addition the plasma generated during the SPS process, enhance the properties of sintered powders due to acceleration of interdiffusion of atoms [35,151].

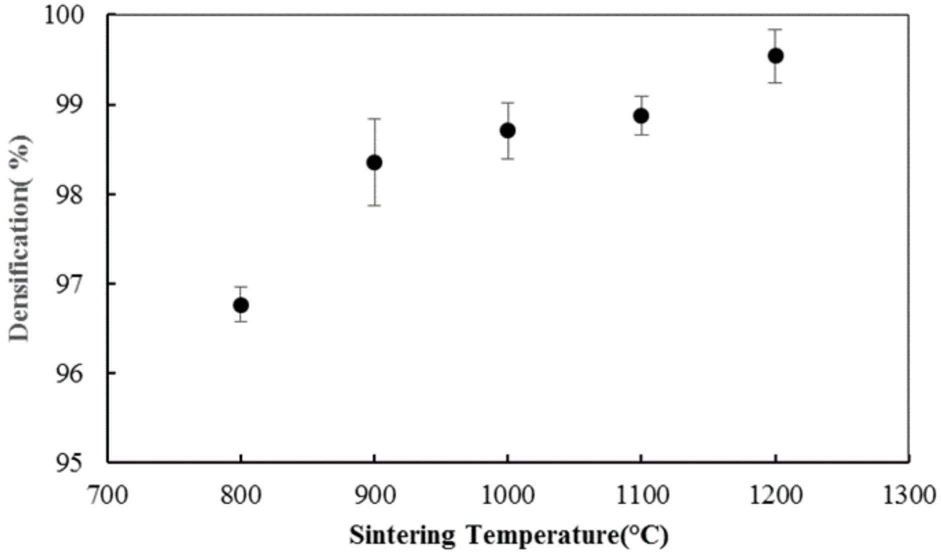

Figure 55 the densification of Ti–20Nb–13Zr alloy at different temperatures

4.3.2.5 Mechanical Properties

4.3.2.5.1 Vickers'Microhardness

Figure 56 shows the effect of SPS temperature on Vickers' microhardness. HV increased with SPS temperature and the trend follow the same trend as densification due to the elimination of pores in the resultant sample during heating and the improved contact between the powder particles.[152, 153]. The HV increased from 619 at 800 °C to 658 at 1200 °C. The HV value slightly increased from 1100 °C to 1200 °C due to homogeneity in the microstructure. However, the HV for 900 °C sample was so high, (This deviation may be related to the different features of the microstructure obtained at 900 °C)This variation appeared also in the error bar as this specimen show the highest standard error of 24.4 among all the samples.

HV and phase composition of nanocrystalline Ti20Nb13Zr alloy investigated in this study and for developed alloys for biomedical application from literature are summarized in Table 7. The mention compositions are in weight percentage except what else mentions. The hardness values for samples sintered by SPS are higher than those obtained by conventional sintering methods. The increase in the hardness of nanocrystalline materials is related to the effect of its higher dislocation density and smaller grain size [154]. In addition as shown Table 7, SPS promotes the formation of β phase compared to α' phase obtained by conventional sintering technique of TiNb13Zr13, TiNb13, and TiAl6V4 [5]. The Ti20Nb13Zr alloy is harder than The Ti13Nb13Zr alloy as well as Ti–6Al–4VAlloy, due to the increased Nb content, which was reported to enhance the wear resistance of Ti based alloy [47].

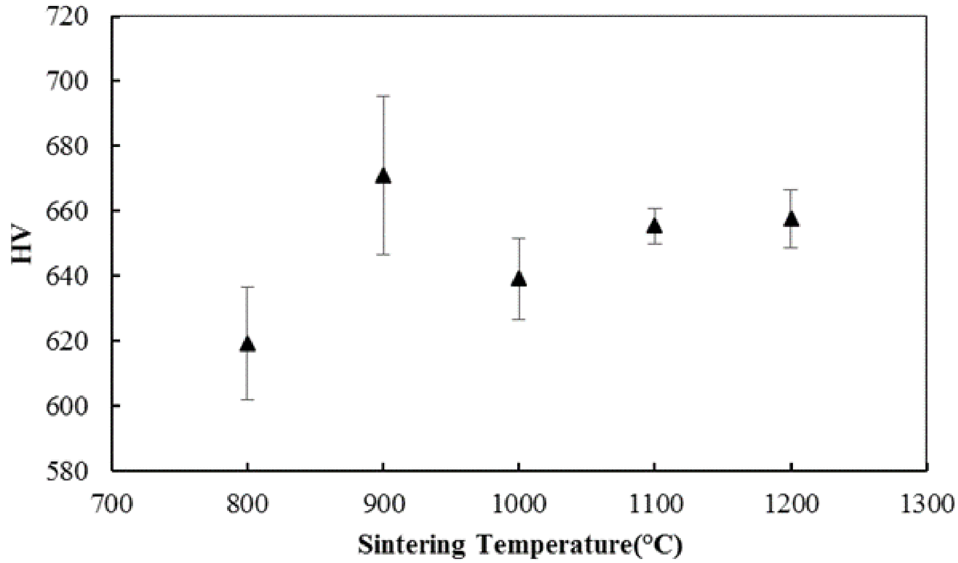

Figure 56 Vickers hardness of Ti–20Nb–13Zr alloy after SPS at different temperatures

Table 7 Comparisons of HV and phases of alloy studied (in italics) and other reported Ti based materials

Alloy Composition ,ref	Consolidation Technique	Phases	HV	Test load (gram)
TiNb13Zr13[5] TiNb13[5] TiAl6V4 [5]	Conventional Sintering	α' α'	290 340 500	200
TiNb13Zr13 [145]	Conventional Sintering	α+ β	300	200
Ti43Al9V (molar ratio) [42]	SPS	γ-TiAl + α2 Ti3Al+B2	592	500
Ti–35Nb–7Zr–5Ta [155]	SPS	α+ β	531-668	500
nanocrystalline Ti20Nb13Zr at% alloy developed in this study *SPS at 1200 °C*	*SPS*	*α+ β*	*658*	*500*

4.3.2.5.2 Nanoindentation

Figure 57 shows the load displacement curve (P–h) for Ti20Nb13Zr at% alloy SPS at 1200 °C. The values of hardness, Young's modulus and the extracted parameters related the resistance of the material to wear and implant lifetime are summarized in Table 8. For comparison purpose SPS has been done for Ti13Nb13Zr at.% alloy at 1200*°C.*As shown in the table The Ti20Nb13Zr at.% alloy is harder than The Ti13Nb13Zr at.% alloy as well as Ti–6Al–4VAlloy, due to the increased Nb content, which was reported to enhance the wear resistance of Ti based alloy [47] in addition to the nanostructured phases which possess higher mechanical properties compared to coarse structure. The Ti20Nb13Zr at.% alloy SPS at 1200 *°C* showed slightly less hardness compared to SPS at 1100 *°C* due to decreased in amount of α phase at 1200*°C.*

The implant wear resistance and lifetime were reported to evaluated by the ratios of H/E_r and H^3/E_r^2[137]. As shown from Table 8, the developed alloy, Ti20Nb13Zr at.% alloy showed higher values compared to Ti13Nb13Zr at.% as well as Ti–6Al–4VAlloy. Which indicate that the developed nanostructured Ti20Nb13Zr alloy possesses higher wear resistance and longer lifetime compared to Ti13Nb13Zr and Ti–6Al–4VAlloys. In addition the developed Ti13Nb13Zr and Ti20Nb13Zr alloys possess lower Young modulus compared to CoCr (Cast) and AISI 316L alloys. The hardness value from nanoindentation for Ti20Nb13Zr alloy SPS at 1100 °C measured at 100 mN (HV=11.8 GPa) is different from measured at 250 mN (H=12.1GPa), this due to ISE (indentation size effect) [138].which was reported to be due to several factors: surface effect [139], the friction between sample and indenter [140], or the gradient in the strain hardening [141,142].

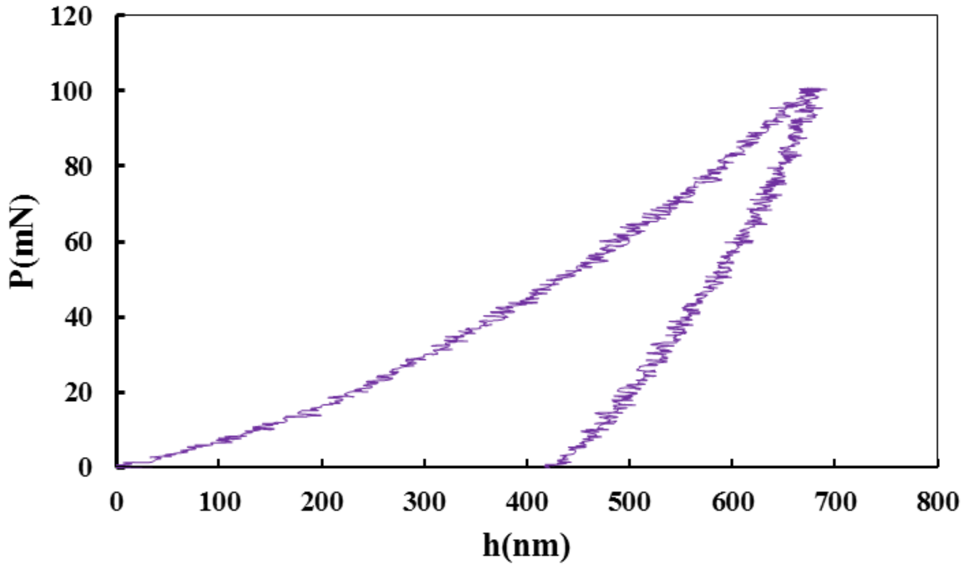

Figure 57 (P–h) nanoindentation curves for Ti20Nb13Zr alloy SPS at 1200 °C

Table 8 Summary of TNZ studied alloy (in italics) properties extracted from the nanoindentation in comparison with other reported metallic biomaterials

Sample	H (GPa)	E_r (GPa)	E_S (GPa)	H/E_r	H^3/E_r^2 (GPa)	Load, (mN)
Ti20Nb13Zr *SPS at 1100 °C*	11.846	138	134.7	0.0858	0.0873	100
Ti20Nb13Zr *SPS at 1100 °C*	12.191	165.5	166	0.0736	0.066	250
Ti20Nb13Zr *SPS at 1200 °C*	10.93 ±0.913	150.23 ±2.57	148.45 ±2.2	0.072 ±0.0048	0.0585 ±0.0127	100
Ti13Nb13Zr *SPS at 1200 °C*	8.148 ±2.019	113.59 ±20.73	108.26 ±18.12	0.070 ±0.0059	0.0425 ±0.015	100
Ti–6Al–4V [137]	5.0 ± 0.1	121 ± 3	116.16 ±2.58	0.041 ±0.001	0.009 ± 0.001	250
CoCr (Cast) [136]			240			Not reported
AISI 316L [136]			210			Not reported

CHAPTER 5

Conclusions and Recommendations

5.1 Conclusions

This work was carried out mainly to develop nanostructured Ti and Nb-based alloys with non-toxic elements for biomedical applications by MA and SPS.

The major findings obtained in this work can be summarized as follows:

1- An amorphous phase was synthesized in mechanically alloyed Nb-Zr alloys that has a positive heat of mixing between the constituent elements, in addition MA resulted in increased solid solubility limits of Nb-Zr system.

2- The formation of an amorphous phase at Zr contents lower than 40% was achieved for the first time in this work.

3- The increased energy of the system due to MA led to the formation of solid-solutions, amorphous phase, which mechanically crystallized to an FCC phase on continued milling

4- A nanostructured Nb-Zr alloy was successfully synthesized for the first time using the MA-SPS technique with an average grain size of between 100-300 nm, maximum hardness and relative density of 584 HV and 97.9%, respectively.

5- Nanostructured Ti20Nb13Zr at% near-β alloy with non-toxic elements and enhanced mechanical properties was successfully fabricated for the first time by spark plasma sintering (SPS).

6- A nearly full density structure was obtained at the SPS temperature of 1200 °C. The microstructure of the obtained alloy consist of a β-Ti (BCC) matrix which surround a α-Ti (hcp) region, and the obtained alloy was chemically homogenized with micro hardness value, HV of 657.

7- The obtained nanostructured Ti20Nb13Zr at% near-β alloy having an average grain size of the dispersed α phase between 70 -140 nm. The nanostructured alloy increases the adhesion of osteoblast which will lead to enhanced interaction with cells.

8- The developed nanostructured Ti20Nb13Zr at% alloy possesses higher wear resistance and longer lifetime compared to Ti13Nb13Zr at% and Ti–6Al–4VAlloys

9- The developed nanostructure Ti–20Nb–13Zr at% alloy is a potential candidate for biomedical applications such as implant material in dental and orthopedic applications.

5.2 Contributions to Original Knowledge

The important contributions of this work to original knowledge can be summarized below:

1. It was the first attempt the nanostructured Ti–20Nb–13Zr at% alloy was fabricated using spark plasma sintering.
2. The spark plasma sintering process has been used for the first time to consolidate the Nb-Zr alloy.
3. The formation of an amorphous phase at Zr contents lower than 40% has been achieved for the first time by using MA.

4. The formation of an amorphous phase and increased solid solubility limits of Nb-Zr were achieved for wide range of compositions.

5.3 Future Directions

The developed nanostructure Ti–20Nb–13Zr alloy in this research is a potential candidate for biomedical applications such as implant material for dental and orthopedic applications.

In light of this research, some future research directions can be recommended and are listed as follows:

1. Study the biocompatibility of the developed alloys.
2. Carry on surface modification and Coating to enhance the characteristic of the developed alloy.
3. Clinical assessment of the developed alloy to be ready for the market use.
4. Carry further mechanical characterization before considering modulus of elasticity values.
5. Use a gloves box to avoid the contamination from the environment.

References

[1] Joon Park and R.S. Lakes,”Biomaterials an Introduction” Springer, Third edition, 2007.

[2] M. Niinomi and D. D. Sc, Metallic biomaterials, J Artif Organs , pp. 105–110, 2008.

[3] Arne Biesiekierski, James Wang, Mohamed Abdel-Hady Gepreel, Cuie Wen, A new look at biomedical Ti-based shape memory alloys, Acta Biomaterialia 8 (2012) 1661–1669.

[4] Ana Lu´cia Roselino Ribeiro , Rubens Caram Junior Fla ´via Farias Cardoso , Romeu Belon Fernandes Filho Luı ´s Geraldo Vaz, Mechanical, physical, and chemical characterization of Ti–35Nb–5Zr and Ti–35Nb–10Zr casting alloys, J Mater Sci: Mater Med (2009) 20:1629–1636.

[5] K.Niespodziana,K. Jurczk and M. Jurczk, The Synthesis Of Titanium Alloys For Biomedical Applications, Rev.Adv.Mater.Sci. 18(2008) 236-240.

[6] M. Niinomi, “Recent Metallic Materials for Biomedical Applications,” Metallurgical and Materials Transactions A, vol. 33, March, 2002.

[7] Suryanarayana, C. Mechanical Alloying and Milling, Progress in Materials Science 46 (2001) 1–184

[8] N. Saheb, Z. Iqbal, A. Khalil, A. S. Hakeem, N. Al Aqeeli, T. Laoui, A. Al-Qutub, and R. Kirchner, “Spark Plasma Sintering of Metals and Metal Matrix Nanocomposites: A Review,” J. Nanomater., vol. 2012, pp. 1–13, 2012.

[9] D. Khang, J. Lu, C. Yao, K.M. Haberstroh, T.J. Webster. The role of nanometer and sub-micron surface features on vascular and bone cell adhesion on titanium. Biomaterials.2008; 29: 970–983.

[10] S. Faghihi, A.P. Zhilyaev, J.A. Szpunar, F. Azari, H. Vali, M. Tabrizian. Nanostructuring of a Titanium Material by High-Pressure Torsion Improves Pre-Osteoblast Attachment. Adv. Mater. 2007; 19: 1069–1073.

[11] Nitesh R. Patel and P. P. Gohil, “A Review on Biomaterials : Scope, Applications & Human Anatomy Significance,” vol. 2, no. 4, 2012.

[12] Lawrence Katz J., Anisotropy of Young's modulus of bone, Nature 1980; 283:106

[13] Black J, Hastings GW. Handbook of biomaterials properties. London UK: Chapman and Hall; 1998.

[14] D.F. Williams,Definitions in biomaterials, Elsevier, Amsterdam (1987).

[15] J. Alvarado, R. Maldonado, J. Marxuach, and R. Otero, Biomechanics Of Hip And Knee Prostheses, December, pp. 6–22, 2003.

[16] Ramsden, J.J., et al., The Design and Manufacture of Biomedical Surfaces. CIRP Annals-Manufacturing Technology, 2007. 56(2): p. 687-711.

[17] Hallab NJ, Anderson S, Stafford T, Glant T, Jacobs JJ., Lymphocyte responses in patients with total hip arthroplasty , J Orthop Res 2005; 23(2):384–91.

[18] Geetha, M., et al., Ti based biomaterials, the ultimate choice for orthopaedic implants–A review. Progress in Materials Science, 2009 pp. 397–425.

[19] Viceconti M, Muccini R, Bernakiewicz M, Baleani M, Cristofolini L. , Large-sliding contact elements accurately predict levels of bone–implant micromotion relevant to osseointegration ,J Biomech 2000;33:1611–8.

[20] Teoh, S.H., Fatigue of biomaterials: A review. International Journal of Fatigue, 2000. 22(10): p. 825-837.

[21] M. Karanjai, R. Sundaresan, G. V.N. Rao, T.R. Rama Mohan, B.P. Kashyap, Development of titanium based biocomposite by powder metallurgy processing with in situ forming of Ca–P phases, Mat. Sc. Engg. A, 2007, 447 (1-2), 19–26.

[22] V. A. R. Henriques E. T. Galvani S. L. G. Petroni M. S. M. Paula T. G. Lemos, Production of Ti–13Nb–13Zr alloy for surgical implants by powder metallurgy, J Mater Sci (2010) 45:5844–5850.

[23] http://www.easyfamilydental.com/treatments/cosmetic-dentistry/dentalimplants.html

[24] Mitsuo Niinomi, Topic in recent research and development of metallic biomaterials, Toyohashi University of technology, PowerPoint presentation.

[25] K.C. Hari Kumar, P. Wollants and L. Delaey, “Thermodynamic assessment of the Ti-Zr system and calculation of the Nb-Ti-Zr phase diagram,” Journal of Alloys and Compounds, vol. 206, pp. 121–127, 1994.

[26] L.W. Ma , H.S. Cheng, C.Y. Chung, B. Yuan, Effect of heat treatment time on microstructure and mechanical properties of Ti–19Nb–9Zr (at%) shape memory alloy, Materials Science & Engineering A 561 (2013) pp. 427–433.

[27] V. Brailovski, S. Prokoshkin, M. Gauthier, K. Inaekyan , S. Dubinskiy , M. Petrzhik , M. Filonov, Bulk and porous metastable beta Ti–Nb–Zr(Ta) alloys for biomedical applications, Materials Science and Engineering C 31 (2011) pp. 643–657.

[28] W. Sungtong, A. Khantachawana, Effect of Zr Addition on Mechanical Properties of Ti-Nb-Zr Alloys for Biomedical Applications, Advanced Materials Research Vols. 463-464 (2012) pp 841-844.

[29] Wang Liqiang, Yang Guanjun, Yang Huabin, Cao Jimin, Lü Weijie, Zhang Di, Characterization of Microstructure and Mechanical Properties of TiNbZr Alloy during Heat Treatment, Rare Metal Materials and Engineering, Volume 38, Issue 7, July 2009.

[30] Wang Liqiang, Yang Guanjun, Yang Huabin, Cao Jimin, Lü Weijie, Zhang Di, Microstructure and Mechanical Properties of TiNbZr Alloy during Cold Drawing, Rare Metal Materials and Engineering, Volume 38, Issue 4, April 2009.

[31] L.M. Elias, S.G. Schneider, S. Schneider, H.M. Silva, F. Malvisi, Microstructural and mechanical characterization of biomedical Ti–Nb–Zr(–Ta) alloys, Materials Science and Engineering A 432 (2006) 108–112.

[32] P. Majumdar, S.B. Singh, M. Chakraborty, The role of heat treatment on microstructure and mechanical properties of Ti–13Zr–13Nb alloy for biomedical load bearing applications, Journal of mechanical behavior of biomedical materials 4 (2011), pp. 1132–1144.

[33] A.E. Aguilar Maya , D.R. Grana , A. Hazarabedian , G.A. Kokubu , M.I. Luppo,, G. Vigna, Zr–Ti–Nb porous alloys for biomedical application, Materials Science and Engineering C 32 (2012) 321–329.

[34] L. M. Zou, C. Yang, Y. Long, Z. Y. Xiao and Y. Y. Li, Fabrication of biomedical Ti–35Nb–7Zr–5Ta alloys by mechanical alloying and spark plasma sintering, Powder Metallurgy, Vol. 55(2012).65-70.

[35] Guoqiang Xie,, Fengxiang Qin , Shengli Zhu , Akihisa Inoue, Ni-free Ti-based bulk metallic glass with potential for biomedical applications produced by spark plasma sintering, Intermetallics 29 (2012) 99e103.

[36] F Zhang , A Weidmann , B J Nebe, E Burke, Preparation of TiMn alloy by mechanical alloying and spark plasma sintering for biomedical applications, Journal of Physics: Conference Series 144 (2009) 012007.

[37] R. Nicula, F. Lu¨then, M. Stir , B. Nebe, E. Burkel , Spark plasma sintering synthesis of porous nanocrystalline titanium alloys for biomedical applications, Biomolecular Engineering 24 (2007) 564–567.

[38] Yeon-wook Kim , Young-jun Lee, Tae-hyun Nam, Shape memory characteristics of Ti–Ni–Mo alloys sintered by sparks plasma sintering, Journal of Alloys and Compounds (2013) 2013, pp. S205-S209

[39] Shengli Zhu, Xinmin Wang, Masahiro Yoshimur,and Akihisa Inoue, Synthesis of Ti-Based Glassy Alloy/Hydroxyapatite Composite by Spark Plasma Sintering, Materials Transactions, Vol. 49, No. 3 (2008) pp. 502-505.

[40] C. Shearwood, Y.Q. Fu, L. Yu, K.A. Khor, Spark plasma sintering of TiNi nano-powder, Scripta Materialia 52 (2005) 455–460.

[41] Yanhua Ma, Kee-Do Woo, Dong Soo Kang, and Sang-Mi Kim, Microstructure and Biocompatibility of Porous Ti-Nb-Zr-CPP Composite Fabricated by Spark Plasma Sintering and Leaching Process, (Korean J. Met. Mater.), Vol. 51, No. 5, pp. 377~383.

[42] X. U. Li-juan, X. Shu-long, C. Yu-yong, and W. Juan, “Microstructure and mechanical properties of Tií43Alí9V alloy fabricated by spark plasma sintering,” Trans. Nonferrous Met. Soc. China, vol. 22, no. 4, pp. 768–772, 2012.

[43] C. Ileana and P. Oana, “Bulk titanium for structural and biomedical applications obtaining by spark plasma sintering (SPS) from titanium hydride powder”, Journal of Thermal Analysis and Calorimetry, pp. 849–857, 2013.

[44] M. Stir, B. Nebe, E. Burkel, R. Nicula, and F. Lu, “Spark plasma sintering synthesis of porous nanocrystalline titanium alloys for biomedical applications”, Biomol Eng. vol. 24, pp. 564–567, 2007.

[45] M. Wen, C. Wen, P. Hodgson, and Y. Li, “Fabrication of Ti – Nb – Ag alloy via powder metallurgy for biomedical applications,” Materials and Design, vol. 56, pp. 629–634, 2014.

[46] F. Y. Zhou, B. L. Wang, K. J. Qiu, W. J. Lin, L. Li, Y. B. Wang, F. L. Nie, and Y. F. Zheng, Microstructure, corrosion behavior and cytotoxicity of Zr–Nb alloys for biomedical application, Mater. Sci. Eng. C, vol. 32, no. 4 (2012) 851–857.

[47] S. J. Li, R. Yang, S. Li, Y. L. Hao, Y. Y. Cui, M. Niinomi, and Z. X. Guo, “Wear characteristics of Ti–Nb–Ta–Zr and Ti–6Al–4V alloys for biomedical applications,” Wear, vol. 257, no. 9–10, pp. 869–876, Nov. 2004.

[48] D.A. Porter, K.E. Easterling, and M.Y. Sherif, “Phase Transformations in Metals and Alloys”, CRC Press, Boca Raton, FL. (2009), p. 11.

[49] C. Suryanarayana, “Non-equilibrium Processing of Materials”, Pergamon Press, Oxford, 1999.

[50] C. Suryanarayana and A. Inoue, “Bulk Metallic Glasses”, CRC Press, Boca Raton, FL. (2011).

[51] H. Jones, A perspective on the development of rapid solidification and nonequilibrium processing and its future, Mater. Sci. Eng., A304-306 (2001) 11

[52] C.C. Koch, in “Processing of Metals and Alloys”, ed. R.W. Cahn, VCH, Weinheim, Germany, 1991, p. 193.

[53] Mitsuo Niinomi , Recent research and development in titanium alloys for biomedical applications and healthcare goods , Science and Technology of Advanced Materials 4 (2003) 445–454

[54] G. Purcek, O. Saray, F. Rubitschek, T. Niendorf, H. J. Maier, and I. Karaman, Effect of internal oxidation on wear behavior of ultrafine-grained Nb – Zr, Acta Materialia, vol. 59, no. 20 (2011) 7683–7694.

[55] O. Jin, Z. J. Zhang, B. X. Liu, Z. J. Zhang, and B. X. Liua(1995) Alloying behavior induced by ion mixing in a system with positive heat of formation, J. Appl. Phys., 78 :149-154.

[56] T.L. Wang, S.H. Liang, J.H. Li, K.P. Tai, B.X. Liu(2008) Abnormal alloying behavior observed in an immiscible Zr–Nb system, J. Phys. D: Appl. Phys., 41 095310-095316.

[57] T. Miyazaki, D. Terada, Y. Miyajima, C. Suryanarayana, R. Murao, Y. Yokoyama,K. Sugiyama, M. Umemoto, Y. Todaka, N. Tsuji, Synthesis of non-equilibrium phases in immiscible metals mechanically mixed by high pressure torsion, J. Mater. Sci. 46 (2011) 4296–4301.

[58] H. H. Liebermann (1993) Rapidly Solidified Alloys, Marcel Dekker, New York,.

[59] C. Suryanarayana and N. Al-Aqeeli (2013) mechanically alloyed nanocomposites, Prog. Mater. Sci., vol. 58, no. 4: 383-502.

[60] Glassy Metals III, edited by H. Beck and H.-J. Güntherodt, (Springer-Verlag, Berlin, 1994).

[61] W. Klement, R.H. Willens, and P. Duwez, Non-crystalline Structure in Solidified Gold–Silicon Alloys, Nature 187, 869 (1960).

[62] D.M. Mattox, Handbook of Physical Vapor Deposition (PVD) Processing (Noyes Publications, Westwood, NJ, 1998).

[63] C. Suryanarayana, “Recent advances in the synthesis of alloy phases by mechanical alloying/milling,” Met. Mater. vol. 2, no. 4, pp. 195–209, Jul. 1996.

[64] C. Suryanarayana, Mechanical Alloying and Milling (Marcel Dekker, New York, 2004).

[65] B.X. Liu, W.S. Lai, and Z.J. Zhang, Solid-state crystal-to-amorphous transition in metal multilayers and its thermodynamic and atomistic modelling, Adv. Phys. 50, 367 (2001).

[66] M.A. Shaikha, M. Iqbal, J.I. Akhter, M. Ahmad, Q. Zaman, M. Akhtar, Alloying of immiscible Ge with Al by ball milling, Mater. Lett. 57 (2003) 3681–3685.

[67] S. Wei, H. Oyanagi, C. Wen, Y. Yang, Metastable structures of immiscible FexCu system induced by mechanical alloying, J. Phys.: Condens. Matter 9 (1997) 11077–11083.

[68] K. Sakurai, C.H. Lee, N. Kuroda, T. Fukunaga, U. Mizutani, Nitrogen effect in mechanical alloying of immiscible Cu–V: extended X-ray absorption fine structure study, J. Appl. Phys. 75 (1994) 7752–7755

[69] G.A. Dorofeev, E.P. Elsukov, A.L. Ul’yanov, Mechanical alloying of immiscible elements in the Fe–Mg system, Inorg. Mater. 40 (2004) 690–699.

[70] M. Zhu, X.Z. Che, Z.X. Li, Mechanical alloying of immiscible Pb–Al binary system by high energy ball milling, J. Mater. Sci. 33 (1998) 5873–5881.

[71] M. Zhu, B.L. Li, Y. Gao, L. Li, K.C. Luo, H.X. Sui, Z.X. Li, Microstructure characteristics of nanophase composite synthesized by mechanical alloying of immiscible Pb–Al and Fe–Cu systems, Scr. Mater. 36 (1997) 447–453.

[72] J. Xu, U. Herr, T. Klassen, R.S. Averback, Formation of supersaturated solid solutions in the immiscible Ni–Ag system by mechanical alloying, J. Appl. Phys. 79 (1996) 3935–3945.

[73] T. Aboud, B.Z. Weiss, R. Chaim, Mechanical alloying of the immiscible system W–Cu, Nanostruct. Mater. 6 (1995) 405–408.

[74] T. Fukunaga, M. Mori, K. Inoue, U. Mizutani, Amorphization in an immiscible Cu–V system by mechanical alloying and its structure observed by neutron diffraction, Mater. Sci. Eng., A 134 (1991) 863–866.

[75] T. Fukunaga, K. Nakamura, K. Suzuki, U. Mizutani, Amorphization of immiscible Cu–Ta system by mechanical alloying and its structure observation, J. Non-Cryst. Solids 117 (118) (1990) 700–703.

[76] C.H. Lee, T. Fukunaga, Y. Yamada, U. Mizutani, H. Okamoto, Amorphization process induced by mechanical alloying in the immiscible Cu–Ta system, J. Phase Equilib. 14 (1993) 167–171.

[77] J. Xu, J.H. He, E. Ma, Effect of milling temperature on mechanical alloying in the immiscible Cu–Ta system, Metall. Mater. Trans. A 28 (1997) 700–703.

[78] M.H. Enayati, P. Schumacher, B. Cantor, Amorphization of Ni60Nb20Zr20 by mechanical alloying, Mater. Sci. Eng., A 375–377 (2004) 812–814.

[79] Y. Wang, X. Chen, H. Geng, Z. Yang, Amorphization and crystallization of Zr66.7xCu33.3Nbx (x= 0, 2, 4) alloys during mechanical alloying, J. Alloys Compd. 474 (2009) 152–157.

[80] L.W. Ma, C.Y. Chung, Y.X. Tong, Y.F. Zheng, Properties of porous TiNbZr shape memory alloy fabricated by mechanical alloying and hot isostatic pressing, J. Mater. Eng. Perform. 20 (2011) 783–786

[81] Z. Xiao, C. Tang, T.L. Ngai, C. Yang, Y. Li, Formation of Fe–Nb–X (X1=4Zr, Ti)amorphous alloys from pure metal elements by mechanical alloying, Physica B 407 (2012) 258–262.

[82] M.S. El-Eskandarany, M. Matsushita, A. Inoue, Phase transformations of ballmilled Nb50Zr10Al10Ni10Cu20 powders and the effect of annealing, J. Alloys Compd. 329 (2001) 239–252.

[83] G. Aurelio, A.F. Guillermet, G.J. Cuello, J. Campo, Structural properties and stability of metastable phases in the Zr–Nb system: Part I. Systematics of quenching-and-aging experiments, Metall. Mater. Trans. A 32 (2001) 1903–1910.

[84] S. Sharma, R. Vaidyanathan, C. Suryanarayana, Criterion for predicting the glass-forming ability of alloys, Appl. Phys. Lett. 90 (2007) 111915.

[85] E.S. Park, D.H. Kim, T. Ohkubo, K. Hono, Enhancement of glass forming ability and plasticity by addition of Nb in Cu–Ti–Zr–Ni–Si bulk metallic glasses, J. Non-Cryst. Solids 351 (2005) 1232–1238.

[86] U. Patil, S.J. Hong, C. Suryanarayana, An unusual phase transformation during mechanical alloying of an Fe-based bulk metallic glass composition, J. Alloys Compd. 389 (2005) 121–126.

[87] S.A. Loureiro, D. Fruchart, S. Rivoirard, D.S. dos Santos, L.M. Tavares, Mechanical alloying of Zr–Nb5 at.% powders: microstructural evolution and hydrogenation properties, Mater. Sci. Forum 570 (2008) 59–64.

[88] C. Suryanarayana and J. Liu(2012) Processing and characterization of mechanically alloyed immiscible metals, Int. J. Mater. Res., vol. 103, no. 9: 1125–1129.

[89] T. Murakami, A. Kitahara, Y. Koga, M. Kawahara, H. Inui, and M. Yamaguchi. (1997) Microstructure of Nb–Al powders consolidated by spark plasma sintering process, Mater. Sci. Eng. A, vol. 239–240: 672–679.

[90] T. Murakami, S. Sasaki, K. Ichikawa, and A. Kitahara (2001) Oxidation resistance of powder compacts of the Nb-Si-Cr system and $Nb_3Si_5Al_2$ matrix compacts prepared by spark plasma sintering, 9, : 629–635.

[91] T. Murakami, C. N. Xu, A. Kitahara, M. Kawahara, and Y. Takahashi(1999) Microstructure, mechanical properties and oxidation behavior of powder compacts of the Nb-Si-B system prepared by spark plasma sintering, vol. 7: 1043–1048.

[92] W. Liu, Y. Fu, and J. Sha (2013) Progress in Natural Science : Materials International Microstructure and mechanical properties of Nb – Si alloys fabricated by spark plasma sintering, vol. 23, no. 1: 55–63.

[93] C. L. Ma, A. Kasama, Y. Tan, H. Tanaka, R. Tanaka,Y. Mishima and S. Handa (2000)Synthesis of Nb/Nb_5Si_3 in-situ Composites by Mechanical Milling and Reactive Spark Plasma Sintering , Materials Transactions, JIM, vol. 41, no.6:719 - 726.

[94] K. Sairam, J. K. Sonber, T. S. R. C. Murthy, C. Subramanian, R. K. Fotedar, and R. C. Hubli(2014) Reaction spark plasma sintering of niobium diboride, Int. J. Refract. Met. Hard Mater., vol. 43: 259–262.

[95] Z. M. Xie, R. Liu, Q. F. Fang, Y. Zhou, X. P. Wang, and C. S. Liu(2014) Spark plasma sintering and mechanical properties of zirconium micro-alloyed tungsten, J. Nucl. Mater., vol. 444, no. 1–3: 175–180.

[96] Ahn H, Lee D, Moon C-W, Lee K-M, Lee K. (2008) A study about the bio-compatibility of Ti–8Ta–3Nb alloys with surface modification" Surf Coat Technol;202:5779–83

[97] Wang XJ, Li YC, Xiong JY, Hodgson PD, Wen CE. (2009) Porous TiNbZr alloy scaffolds for biomedical applications", Acta Biomater; 5:3616-24

[98] Shibo Guo, Aimin Chu, Haijiang Wu, Chunbo Cai, Xuanhui Qu, (2014) Effect of sintering processing on microstructure, mechanical properties and corrosion resistance of Ti–24Nb–4Zr–7.9Sn alloy for biomedical applications", J. Alloys and Comp. 597: 211–216.

[99] F. Rubitschek, T. Niendorf, I. Karaman, and H. J. Maier, (2012) Corrosion fatigue behavior of a biocompatible ultrafine-grained niobium alloy in simulated body fluid, J. Mech. Behav. Biomed. Mater., vol. 5, no. 1: 181–192.

[100] El-eskandarany, M. S. Mechanical Alloying For Fabrication of Advanced Engineering Materials. William Andrew Publishing Norwich, New York, U.S.A., 2001

[101] Suryanarayana, C., Ivanov, E. & Boldyrev, V, The science and technology of mechanical alloying. Materials Science and Engineering: A, 304-306, pp.151-158, 2001.

[102] ZA Munir, U. Anselmi-Tamburini, M. Ohyanagi, The The effect of electric field and pressure on the synthesis and consolidation of materials: A review of the spark plasma sintering method, J Mater Sci, 41, 2006, 763–777.

[103] M. Pellizzari, A. Fedrizzi, M. Zadra, Influence of processing parameters and particle size on the properties of hot work and high speed tool steels by Spark Plasma Sintering, Materials & Design, 32, 2011, p. 1796-1805.

[104] M. Belmonte, J. González-Julián, P. Miranzo and M. I. Osendi, Spark plasma sintering: A powerful tool to develop new silicon nitride-based materials, Journal of the European Ceramic Society, 30, 2010, 2937-2947.

[105] F Bernard, S Le Gallet, N Spinassou, S Paris, E Gaffet, J N Woolman, et al , Dense Nanostructured Materials Obtained by Spark Plasma Sintering and Field Activated Pressure Assisted Synthesis Starting from Mechanically Activated Powder Mixtures, Science of Sintering, 2004,155-164

[106] C. Camurri, M. Ortiz, and C. Carrasco (2003) Hot consolidation of Cu–Li powder alloys: a first approach to characterization, Mater. Charact. vol. 51, no. 2–3: 171–176.

[107] C. Y. Xu, S. S. Jia, Z. Y. Cao (2005) Synthesis of Al-Mn-Ce alloy by the spark plasma sintering, Mater. Charact., 54: 394–398.

[108] X. L. Shi, H. Yang, S. Wang(2009) Spark plasma sintering of W-15Cu alloy from ultrafine composite powder prepared by spray drying and calcining-continuous reduction technology, Mater. Charact., 60 :133–137.

[109] J. Garay, “Current-activated, pressure-assisted densification of materials,”Annual Review of Materials Research, vol. 40, no. 1, pp. 445–468, 2010.

[110] Z. Zhaohui, W. Fuchi, W. Lin, L. Shukui, and S. Osamu, “Sintering mechanism of large-scale ultrafine-grained copper prepared by SPS method,”Materials Letters, vol. 62, no. 24, pp. 3987 – 3990, 2008.

[111] Birju Shah, Vasu Kumar Kakumanu, Arvind K. Bansal, “amorphous--Analytical Techniques for Quantification of Amorphous.” Journal of Pharmaceutical Sciences, Vol. 95, No. 8, August 2006.

[112] Mettler-Toledo GmbH 1998, Density Kit, operation instructions manual, Switzerland.

[113] Oliver WC, Pharr GM. An improved technique for determining hardness and Elastic-modulus using load and displacement sensing indentation Experiments. J Mater Res 1992;7:1564–83

[114] Ikehata H, Nagasako N, Furuta T, Fukumoto A, Miwa K, Saito T. First principles calculations for development of low elastic modulus Ti alloys. Phys Rev B 2004; 70:174113.

[115] Leyens C, Peters M, editors. Titanium and titanium alloys: fundamentals and applications. Weinheim: Wiley–VCH; 2003.

[116] Lutjering G, Williams JC. Titanium. 2nd ed. Berlin: Springer; 2007.

[117] Donachie Jr MJ. Titanium: a technical guide. 2nd ed. Materials Park, OH: ASM International; 2000.

[118] S. Sharma and C. Suryanarayana, Mechanical Crystallization of Fe-based Amorphous Alloys, J. Appl. Phys. 102, 083544 (2007).

[119] J. Soltys, Z. Lisowski, J. Knapczyk, X-ray diffraction study of the crystallinity index and the structure of the microcrystalline cellulose, Acta Pharm. Technol. 30 (1984) 174–180.

[120] L.D. Majdanac, D. Poleti, M.J. Teodorovic, Determination of the crystallinity of cellulose samples by X-ray diffraction, Acta Polym. 42 (1991) 351–357.

[121] E. Ma, Alloys created between immiscible elements, Prog. Mater. Sci. 50, 413-509 (2005).

[122] H.W. Sheng, G. Wilde, and E. Ma, The competing crystalline and amorphous solid solutions in the Ag–Cu system,Acta Mater. 50, 475 (2002).

[123] X. Sauvage, L. Renaud, B. Deconiihout, D. Blavette, D.H. Ping, and K. Hono, Solid State Amorphization In Cold Drawn Cu/Nb Wires,Acta Mater. **49**, 389 (2001).

[124] G. Veltl, B. Scholz, and H.D. Kunze, Amorphization of Cu-Ta alloys by mechanical alloying Mater. Sci. Eng. A134, 1410 (1991).

[125] T. Egami, Y. Waseda, Atomic size effect on the formability of metallic glasses, J. Non-Cryst. Solids 64 (1984) 113–134

[126] J. A. Lemberg, M. R. Middlemas, T. Weingärtner, B. Gludovatz, J. K. Cochran, and R. O. Ritchie, "On the fracture toughness of fine-grained Mo-3Si-1B (wt.%) alloys at ambient to elevated (1300 °C) temperatures," *Intermetallics*, vol. 20, no. 1, pp. 141–154, Jan. 2012.

[127] E. Zhou, C. Suryanarayana, F.H. Froes, Effect of premilling elemental powders on solid solubility extension of magnesium in titanium by mechanical alloying, Mater. Lett. 23 (1995) 27–31.

[128] J.Y.Qin X.J. Wu, L.F.Cheng, Exothermal and endodermal Phenomena in Nano crystalline Aluminum ,nanostructured materials Vol 2, pp 99-108, 1993

[129] O. Guillon, J. Gonzalez-Julian, B. Dargatz, T. Kessel, G. Schierning, J. Räthel, and M. Herrmann, Field-Assisted Sintering Technology/Spark Plasma Sintering: Mechanisms, Materials, and Technology Developments. Adv. Eng. Mater.,2014; 16, no. 7: 830–849.

[130] F. Zhang, M. Reich, O. Kessler, and E. Burkel, The potential of rapid cooling spark plasma sintering for metallic materials. Mater. Today, 2013; 16, no. 5: 192–197.

[131] J. C. Garrett, I. Sigalas, M. Herrmann, E. J. Olivier, and J. H. O'Connell, cBN reinforced Y-α-SiAlON composites, J. Eur. Ceram. Soc., 2013; 33, no. 11: 2191–2198.

[132] C. Wang, W. Ji, and Z. Fu, "Mechanical alloying and spark plasma sintering of CoCrFeNiMnAl high-entropy alloy," Adv. Powder Technol., vol. 25, no. 4, pp. 1334–1338, Jul. 2014.

[133] G. Adamek and J. Jakubowicz, Microstructure of the mechanically alloyed and electrochemically etched Ti – 6Al – 4V and Ti – 15Zr – 4Nb nanocrystalline alloys, Mater. Chem. Phys., vol. 124, no. 2–3 (2010), pp. 1198–1204.

[134] T.J. Webster, J.U. Ejiofor. Increased osteoblast adhesion on nanophase metals: Ti, Ti6Al4V, and CoCrMo. Biomaterials. 2004; 25:4731–4739.

[135] N. Saheb. Spark plasma and microwave sintering of Al6061 and Al2124 alloys. International Journal of Minerals, Metallurgy and Materials.2013; 2: 152–159

[136] A. Domı, A. Lara, A. L. Ortiz, and A. Mun. Densification of additive-free polycrystalline b -SiC by spark-plasma sintering. Ceramics International. 2012; 38: 45–53

[137] A. Hynowska, A. Blanquer, E. Pellicer, J. Fornell, S. Suriñach, M. Baró, S. González, E. Ibáñez, L. Barrios, C. Nogués, and J. Sort, “Novel Ti–Zr–Hf–Fe Nanostructured Alloy for Biomedical Applications,” *Materials (Basel).*, vol. 6, no. 11, pp. 4930–4945, Oct. 2013.

[138] Manika, I.; Maniks, J. Size effects in micro- and nanoscale indentation. Acta Mater. 2006, 54, 2049–2056.

[139] Gerberich, W.W.; Tymiak, N.I.; Grunlan, J.C.; Horstemeyer, M.F.; Baskes, M.I. Interpretations of indentation size effects. J. Appl. Mech. 2002, 69, 433–442.

[140]Li, H.; Ghosh, A.; Han, Y.N.; Bradt, R.C. The frictional component ofthe indent of the indentation size effect in low load microhardness testing. J. Mater. Res. 1993, 8, 1028–1032.

[141]Nix, W.D.; Gao, H. Indentation size effects in crystalline materials: A law for strain gradient plasticity. J. Mech. Phys. Solids 1998, 46, 411–425.

[142]Huang, Y.; Qu, S.; Hwang, K.C.; Li, M.; Gao, H.A conventional theory of mechanism-based strain gradient plasticity. Int. J. Plast. 2004, 20, 753–783.

[143] Van C. Mow , and Rik Huiskes,Basic Orthopaedic Biomechanics and Mechano-Biology, Lippincott Williams & Wilkins, 2005.

[144] A. Nouri, X. Chen, Y. Li, Y. Yamada, P. D. Hodgson and C. E.Wen: ‘Synthesis of Ti–Sn–Nb alloy by powder metallurgy’,Mater. Sci. Eng. A, 2008, A485, (1–2), 562–570.

[145] V. A. R. Henriques • E. T. Galvani • S. L. G. Petroni • M. S. M. Paula • T. G. Lemos, Production of Ti–13Nb–13Zr alloy for surgical implants by powder metallurgy, J Mater Sci (2010) 45:5844–5850.

[146] Niinomi, M.; Akahori, T. Improvement of the fatigue life of titanium alloys for biomedical devices through microstructural control. Expert Rev. Med. Devices 2010, 7, 481–488.

[147] B. C. Ward and T. J. Webster, “Increased functions of osteoblasts on nanophase metals,” Mater. Sci. Eng. C, vol. 27, no. 3, pp. 575–578, Apr. 2007.

[148]L. Zhang and T. J. Webster, “Nanotechnology and nanomaterials: Promises for improved tissue regeneration,” Nano Today, vol. 4, no. 1, pp. 66–80, Feb. 2009.

[149] E. B. Taddei, V. A. R. Henriques, C. R. M. Silva and C. A. A. Cairo: ‘Production of new titanium alloy for orthopedic implants’, Mater. Sci. Eng. C, 2004, C24, (5), 683–687.

[150]. F. Zhang, A. Weidmann, B. J. Nebe and E. Burkel: ‘Preparation of TiMn alloy by mechanical alloying and spark plasma sintering for biomedical applications’, Journal of Physics: Conference Series, 2009,144, (1), 012007:1–5.

[151] Omori M., Sintering, consolidation, reaction and crystal growth by the spark plasma system (SPS), Mater Sci Eng 2000;A287:183.

[152] R.M. German, Powder Metallurgy Science, Metal Powder Industries Federation, Princeton, 1994.

[153] R.M. German, Sintering Theory and Practice, John Wiley, New York, 1996.

[154] A.P. Zhilyaev, T.G. Langdon, Using high-pressure torsion for metal processing:

Fundamentals and applications, Prog. Mater. Sci. 53 (2008) 893–979.

[155] L. M. Zou, C. Yang, Y. Long, Z. Y. Xiao, and Y. Y. Li, “Fabrication of biomedical Ti – 35Nb – 7Zr – 5Ta alloys by mechanical alloying and spark plasma sintering, Powder Metallurgy,” vol. 55, no. 1, pp. 65–71, 2012.

Appendix

List of Publications

This research has yielded the following publications:

Patent:

1. **M. A. Hussien**, N. Al-Aqeeli, C. Suryanarayana, “Novel Amorphous and Nanostructured Nb–Zr Alloy”, US patent: US 14/513,368, **filed** “October 2014”.
2. **M. A. Hussien**, N. Al-Aqeeli ,Nanostructured Titanium Alloy and Its Synthesis Method for Biomedical Applications, **submitted**, October 2014 , Ref. 444548US.

Peer reviewed journal publications:

Published:

1. N. Al-Aqeeli, **M.A. Hussein**, C. Suryanarayana, Phase evolution during high energy ball milling of immiscible Nb–Zr alloys, **Advanced Powder Technology 26 (2015) 385–391.**
2. N. Al-Aqeeli, C. Suryanarayana, and **M. A. Hussein**, “Formation of an amorphous phase and its crystallization in the immiscible Nb–Zr system by mechanical alloying,” **J. Appl. Phys**., vol. 114, no. 15, p. 153512, **2013**.
3. **M. A. Hussein**, M. Abdul Samad, and N. Al-Aqeeli, Wear Characteristics of Metallic Biomaterials: A Review ,materials ,**Accepted**

Submitted:

4. **M.A. Hussein**, C. Suryanarayana, A. Madhan Kumar, N. Al-Aqeeli, Effect of Sintering Parameters on Microstructure, Mechanical properties and Electrochemical Behavior of Nb-Zr Alloy for Biomedical Applications, submitted to journal of Materials & Design.

Under preparation:

5. **M. A. Hussien**, N. Al-Aqeeli, C. Suryanarayana, Synthesis of nanostructured Ti-20Nb-13Zr alloy for biomedical applications by mechanical alloying and spark plasma sintering
6. **M.A. Hussein**, C. Suryanarayana, N. Al-Aqeeli, Effect of Zr on the glass forming ability of mechanically alloyed NbZr immiscible Alloys.
7. **M.A. Hussein**, C. Suryanarayana, A. Madhan Kumar, N. Al-Aqeeli **,** Novel Near –β Ti alloy for biomedical applications.

Other papers during PhD program

8. Ihsan H. Toor, Bekir S. Yilbas, Cihan Karatas, **Mohammed A. Hussein**, and Mohammed N. Zafar. Electrochemical investigation of the effect of different laser surface treatments on Haste alloy G alloy. International Journal of Materials Research: (2013) Vol. 104, No. 10, pp. 1007-1012.
9. Junaid Ahmad, Nasser Al-Aqeeli, **M.A. Hussein**, Ihsan H. Toor, Amorphization and Recrystallization of Fe(82-x)Cr18-Six (x=0, 1, 2, 3)Alloys During Mechanical Alloying, **submitted** to Advanced Powder Technology.
10. Junaid Ahmad, Nasser Al-Aqeeli, **M.A. Hussein**, Ihsan H. Toor ,Microstructural and Mechanical characterization of Fe-Cr-Si alloys prepared by Mechanical alloying and Spark Plasma Sintering.

Vitae

Name Mohamed Abdrabou Hussein
Email mahussein@kfupm.edu.sa moh_abdrabou@yahoo.com
Current Address Dep. of Mechanical Engineering, King Fahd University of
Petroleum & Minerals (KFUPM), Dhahran 31261, Saudi Arabia
Permanent address Dep. of Mechanical Engineering, Kafrelsheikh University,
Kafrelsheikh 33516, Egypt

Education

- Ph.D. - May 2015 Mechanical Engineering (Applied Materials &Manufacturing) Department of Mechanical Engineering, King Fahd University of Petroleum & Minerals (KFUPM), Saudi Arabia (GPA 3.75). (KFUPM ABET Accreditation).
- M.Sc. - October 2009: Mechanical Engineering, Tanta University, Egypt.
- B.Sc. -June 2003: Mechanical Engineering, Tanta University, Egypt. Excellent with Honor degree 2nd rank.

Professional Experience and Positions

- January 2012-now: Lecturer-B &PhD Student, Dep. of Mechanical Engineering, KFUPM, Saudi Arabia.
- December 2009- now (on leave): Assistant lecturer in Mechanical Engineering Department, Kafrelsheikh University, Egypt.
- January 2007- November 2009. Demonstrator in Mechanical Engineering Department, Kafrelsheikh University, Egypt.
- February 2005-January 2007: Demonstrator in Production Engineering and Mechanical Design Department, Tanta University, Egypt.
- December 2003 –February/ 2005: Mechanical Engineer in Egyptian Iron & Steel Company, Helwan, Egypt.

Area of interest

- Material Science, Biomaterials, Synthesis, Processing, and Characterization of nanomaterials and nanocomposites, Mechanical Alloying (MA), and Spark plasma sintering (SPS)
- Materials.Characterization of Macro, Micro and Nano Materials,
- Thermodynamic modeling by Miedema, Application of Computational Tools in Manufacturing Technology
- Corrosion, Electrochemical investigations
- Welding Engineering: Friction Stir Welding (FSW).